Model-Based Force Control of a Fluidic-Muscle Driven Parallel Platform

Von der Fakultät für Ingenieurwissenschaften, Abteilung Maschinenbau und Verfahrenstechnik der
Universität Duisburg-Essen
zur Erlangung des akademischen Grades

eines

Doktors der Ingenieurwissenschaften

Dr.-Ing.

genehmigte Dissertation

von

Mahendra Dhanu Singh
aus
Essen

Gutachter:	Prof. Dr.-Ing. Andrés Kecskeméthy Prof. Dr.-Ing. Vincenzo Parenti Castelli
Tag der mündlichen Prüfung:	11. Juni 2010

Vorwort

Die vorliegende Arbeit entstand während meiner Tätigkeit als wissenschaftlicher Mitarbeiter am Lehrstuhl für Mechanik und Robotik des Instituts für Mechatronik und Systemdynamik der Universität Duisburg-Essen.

Mein besonderer Dank gilt Herrn Prof. Dr.-Ing. Andrés Kecskeméthy (Universität Duisburg-Essen), der diese Arbeit angeregt und wissenschaftlich betreut hat. Seine Unterstützung und wertvollen Hinweise haben maßgeblich zum Gelingen dieser Arbeit beigetragen. Ebenso danke ich Herrn Prof. Dr.-Ing. Vincenzo Parenti Castelli (Università di Bologna) für das entgegengebrachte Interesse an meiner Arbeit und die Bereitschaft, das Korreferat für diese Dissertation zu übernehmen.

An dieser Stelle möchte ich mich aufrichtig bei Herrn Dipl.-Ing. Kusnadi Liem bedanken für die kooperative und freundschaftliche Zusammenarbeit und die zahlreichen inspirierenden Diskussionen, die dieser Arbeit wertvolle Impulse gaben. Weiterhin möchte ich mich bedanken bei unseren damaligen Studenten Dipl.-Ing. Marcel Langer und Dipl.-Ing. Christian Michael für die Unterstützung bei den Messungen am Prüfstand.

Außerdem sei insbesondere die Unterstützung der Deutschen Forschungsgemeinschaft (DFG) (Ke 526/4-1/4-2) in diesem Projekt dankend hervorgehoben. Herrn Dr.-Ing. Rüdiger Neumann und der Firma Festo bin ich sehr dankbar für die wertvollen Informationen und die Bereitstellung von wichtigen Prüfstandskomponenten.

Darüber hinaus bin ich Herrn Prof. Dr.-Ing. Diethard Bergers für seine Unterstützung zu Studienzeiten und dessen Einfluss auf meinen bisherigen Werdegang sehr verbunden.

Für die Korrektur des Manuskripts gebührt den Herren Dr.-Ing. Özgür Korkmaz, Dr.-Ing. Ismail Korkmaz und Dipl.-Ing. Marc-André Keip mein freundschaftlicher Dank. Des Weiteren möchte ich mich recht herzlich bei allen Kolleginnen und Kollegen des Lehrstuhls für Mechanik und Robotik für die freundschaftliche Zusammenarbeit und die schönen Jahre am Lehrstuhl bedanken.

Mein ganz persönlicher Dank gilt meinen Eltern und Frau Ruth Breddemann, für deren richtungsweisende und tatkräftige Unterstützung in meinem Leben. Abschließend möchte ich meiner Frau Reshma und meiner gesamten Familie dafür danken, dass sie mir in diesem Lebensabschnitt unterstützend zu Seite gestanden haben.

Dortmund, im Mai 2011 Mahendra Dhanu Singh

Contents

1 Introduction

Biomechanics is a field of science which investigates the relationship between the motion of animals and human beings and the corresponding forces. It plays a decisive role for the improvement of human disease diagnosis and therapies, the development of new techniques for injury prevention measures, and the reduction of medical costs. Hereby, virtual computer simulations as well as physical devices are becoming a more and more important tool for predicting effects of medical treatment and the diagnosis of their success.

The goal of this thesis is to design, build and validate a six-degree-of-freedom parallel platform for the physical reproduction of defined forces and torques. Moreover, the platform must fulfill the geometric requirements needed for its future application as a physical simulator of human cervical-spine motion and loads. In this context, the intervertebral force-displacement properties of two adjacent cervical vertebrae shall be regarded (see Figure 1.1). The device is intended for the physical analysis of neck components and spinal implants. The tested specimen shall be mounted between the end-effector of the platform and a static rigid counterpart. The platform is driven by

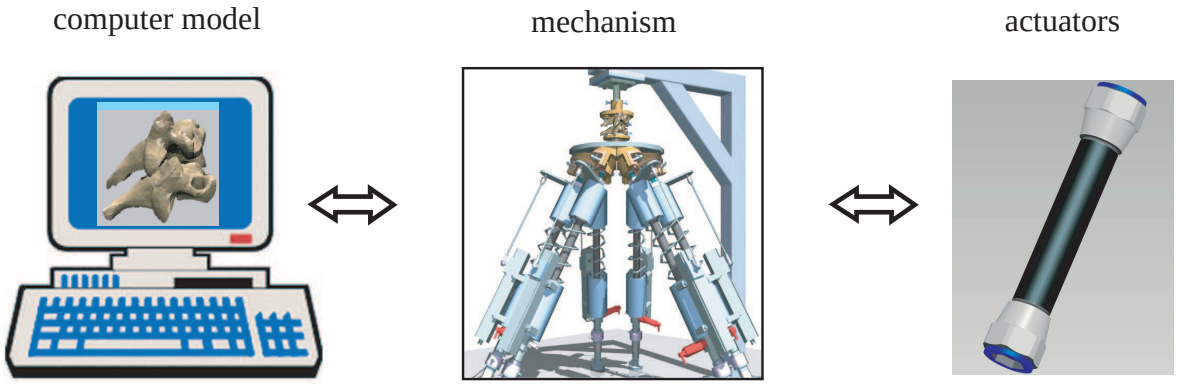

Figure 1.1: Concept of the proposed cervical spine test-bed

six force-controlled actuator legs. The platform control prescribes the target forces of the actuators such that the required platform forces and torques are reproduced at the end effector. The long-term objective is to embed a virtual computer model (Figure 1.1) of a cervical vertebrae pair into the platform control for on-line computation of the end-effector target forces.

Parallel platforms are suitable for the reproduction of intervertebral motion since, on the one hand, they can achieve motion with six degrees of freedom (6 DOF). On the other hand, they feature very high stiffnesses due to the parallel structure leading to a high position accuracy and proper

force transmission at the end effector. The obtained physical simulator is intended for physicians, surgeons or orthopedists, such that they can assess effects of spinal therapeutic or surgical treatment (e.g. inserting implants) prior to the application on the patient. Additionally, the mechanism shall allow for *in vitro* measurements of vertebrae probes under controlled motion and load in order to determine the biological parameters. Hereby, the considered vertebrae pair is mounted along with its intervertebral structures to the end effector for measuring the force-displacement relationships. Especially for this purpose the high stiffness of parallel manipulators and their position accuracy are advantageous.

It has to be regarded that the device is to be applied in environments such as medical centers or laboratories which have to be kept relatively clean. Therefore, fluidic muscles are choosen as actuators as depicted on the right-hand side of Figure 1.1. They consist of a rubber tube and two flanges and produce tension forces when the tube is inflated with compressed air. The application is clean, because no compressed oil is used, as e.g. in hydraulics. Since the muscles are inflated with compressed air, and as supplying lines for compressed air are available in almost any public building, the operation of the actuators is convenient. Furthermore, fluidic muscles are slip-stick free, have a long life-cycle and can produce large forces in relation to their actuator size. Due to the compliant property of the rubber material and the affinity of fluidic muscles to biological muscles, they are suitable for driving the platform.

The cervical spine is given special attention, due to major risk at car accidents, as it is affected with extremely large contact and inertia forces in a collision situation. Major neck injuries can lead to extensive damage of the surrounding tissues and persistent invalidity or death. These injuries can be diagnosed reliably, as e.g. for displaced or fractured vertebrae. The majority of neck injuries, however, are minor injuries with a low threat to life, which are often referred to as whiplash injuries [22]. Although they are classified as minor injuries, they can have severe consequences on the patient's personal and working life, leading to enduring symptoms. Whiplash injuries are still difficult to diagnose because very often a clear sign of structural changes cannot be found.

It is necessary to analyze how the external loads imposed on the neck are transferred to respective internal loads and deformations of individual tissues of the cervical spine [22]. Therefore, a procedure is needed which helps to diagnose the force under the anatomic situation of the individual patient [56]. The reconstruction of intervertebral motion, although basically understood, still poses many open problems. The reason for this is the complex interaction of two adjacent vertebrae. The vertebrae undergo six dimensional motion relative to one other that displays a high degree of coupling between gross translational and rotational degrees of freedom due to restrains imposed by ligaments and muscles and the compliant nature of the intervertebral discs [99]. As a consequence, predictions based on simplified models, such as simple hinge models for intervertebral motion or linear stiffness approximations of the behavior of the intervertebral disc, often fail to match experimental measurements, in particular in vehicle crash situations.

For the simulation of intervertebral motion, one can use either computer models or physical surrogate devices. Computer models have the advantage that they can be very flexible and comprehensive, allowing one to predict the behavior of the human neck motion and the effect of additional components accurately. However, they have the disadvantage that they cannot provide surgeons with haptic sensing such as needed to assess the effects of medical interventions, and that they cannot be used for testing implant units, which are still under development such as artificial intervertebral discs. A novel concept in spinal biomechanics is to apply a computer-controlled physical simulator of spinal motion that can be used for biofidelic hardware-in-the-loop testing of spinal implants and neck components. For the emulation of intervertebral motion, the corresponding surrogate mechanism has to be more complex, as six degrees of freedom and a spatial transmission of forces are required. To this end, a parallel platform is suitable.

1.1 Aims and structure of thesis

Within the scope of this thesis, the goal is to design and validate a fluidic-muscle driven parallel platform which can reproduce defined forces/torques in six DOF. The long-term objective is that the mechanism can be applied for the physical simulation of six DOF cervical spine motion.

Since the applied actuators have a nonlinear behavior, a model-based force control of the applied fluidic muscles shall be developed and embedded into the platform control. The parallel manipulator must be able to produce forces and torques in six DOF at the end effector. It has to be verified that the motion ranges of cervical pairs (specifically C5-C6) can be achieved with the target manipulator. Further, it must be ensured that the forces and torques which are produced between human cervical vertebrae can be generated within the required workspace of the parallel manipulator.

At first, in section 1.2 a literature survey is given which covers the three main topics of pneumatic-muscle applications, physical devices for simulation of spine motion and computer models of spine motion.

In section 1.3, a historical review of 6-DOF parallel platforms is given, ranging form the first-ever concepts to nowadays applications, closing with the description of parallel robots applied in the medical field.

Since in future the motion of two adjacent vertebrae of the human cervical spine shall be simulated physically with the platform, in chapter 2, the physical properties of the human cervical spine are presented. In section 2.2, the corresponding biomechanical parameters are evaluated in order to define the required workspace of the parallel manipulator. Furthermore, in section 2.3, two available computer models of the cervical vertebrae C5-C6 are described. The one model was programmed with the multibody C++ library MBILE[52] and the other one with MADYMO, a software package for occupant-safety analysis. Both computer models are compared with experimental data from Moroney et. al [68].

Chapter 3 is concerned with the design of the parallel manipulator. First, the design aims are defined and classified. Hereafter, basic types of 6-DOF parallel platforms are presented. In section 3.3 the basic geometric and quasistatic properties of the platform actuators (fluidic muscles) are summarized. After this, the design of the platform, i.e., the determination of the platform dimension and geometry, is documented. In section 3.5, the workspace of the obtained geometrical concept is analyzed in terms of motion and force. This chapter is closed with a description of the platform prototype and its components.

Chapter 4 is devoted to the development of the model-based force control of a single actuator. In section 4.1, the equations governing the gas dynamics of a fluidic muscle are derived. Hereafter, an exponential approach is introduced for the approximation of the gas-dynamic behavior of the fluidic muscle. In section 4.3, the procedure of the actuator identification is described, for which different experiments are performed with each of the six actuators. First, the quasistatic behavior of the muscle is evaluated by measuring the relationship between force, pressure and stroke, before the volume-stroke relationship and finally the pressure rates for an opening and closing valve are analyzed. The measured data is approximated with appropriate functions and the respective parameters. Hereafter, the mathematical model of the actuator is presented, which can be adjusted to the behavior of each applied actuator by inserting the individually identified parameters into the model. The model-based actuator force control, which implies the inverse of the actuator model as a feed forward in combination with a PID controller, is described in section 4.4.

Moreover, in section 4.5, the single-axis test bed, on which the identification procedure of each actuator was carried out, is presented with a description of the control and measurement devices. The experimental results of the single-axis control runs are evaluated in section 4.5.

In chapter 5, the developed control algorithm of the previous chapter is applied to the developed platform prototype. The kinetostatics and dynamics of the parallel manipulator are specified in section 5.1. The concept of the platform force control is presented in section 5.2. Hereafter, the results of the platform control are documented and validated.

In the last chapter, the main issues of this thesis are summarized and suggestions for further research are outlined.

1.2 Literature survey

The relevant literature can be basically classified according to Table 1.1 in three main groups. At first, existing control approaches for pneumatic artificial muscles (PAM) are described, and parallel manipulators driven by pneumatic muscles are presented. Then, a survey of existing physical mechanisms is made, describing devices which are (1) used as surrogates of the human spine and (2) which are applied for experiments with vertebrae probes. Finally, an overview of computer models describing the cervical spine motion is given.

pneumatic artificial muscles (PAM)	PAM controlling methods
	PAM-driven parallel manipulators
physical devices for investigation of spine motion	surrogate mechanisms
	experimental setups for specimen testing
computer models of spine motion	multibody systems
	finite-element methods

Table 1.1: Overview of topics related to the physical simulation of the cervical spine

Applications of pneumatic artificial muscles

The *fluidic muscle* is a commercially available pneumatic artificial muscle (PAM) produced by FESTO company. The indication *fluidic* refers to the fact that it can also be operated with water [38]. The first known PAM was developed by J. L. McKibben according to Schulte [83]. It consisted of internal rubber tube surrounded by a sleeve of braided fibers. At both ends the sleeve and the tube were fixed to fittings. By inflating with compressed air the tubing and fiber shell is expanded radially, which induces an axial contraction of the actuator [19]. McKibben intended to use this actuator as an artificial limb.

In most of the following PAMs, the basic funtionality of the McKibben muscle was maintained. In the late 1980's the McKibben muscle was commercialized by Bridgestone Company as the *rubbertuator* in Japan as stated by Inoue [46, 18]. More recently, McKibben-like muscles were reintroduced by Shadow Robot Company and by Festo Company and is still brought to the market. In particular, Festo muscles have fibers which are integrated into the rubber material instead of an interior tube and an external braided sleeve. Before the commercial PAMs were reintroduced, researchers in the 1990's mainly used custom-built McKibben muscles [10, 14].

McKibben muscles were primarily applied to anthropomorphic robots or rehabilitation devices as for instance in the RUPERT project [49, 89], who developed a therapy device for the complete arm of stroke patients in force-feedback therapies. Further, Bharadwaj et al. proposed a concept for an ankle therapy device driven by pneumatic muscles [48].

A major problem with braided PAMs (McKibben muscles) is that the relationship between stroke, pressure and force is highly nonlinear. The nonlinearities limit the controllability, lead to oscillatory motion and make it difficult to realize accurate motion in combination with high speed. Further, it is reported that the behavior of PAMs can be time variant [1, 101].

Daerden and Lefeber [19] refer to the dry friction of the rubber and the fibers, which produces heat influencing the material characteristics. The temperature resulting from friction affects muscle operation: warm muscles behave different from cold ones [11]. It is reported [39] that a positional drift of the rubbertuator occurs when the actuator pressure is oscillating about a fixed value. Chou and Hannaford [14] also observed a hysteresis in the force-stroke relationship of their applied McKibben muscle. Thus, pneumatic artificial muscles require a control algorithm which regards the specific behavior of the rubber material.

Hildebrandt et. al [40] suggested a model-based control approach for the position control of a uniaxial teststand driven by one fluidic muscle. Since the physical model is highly nonlinear, a flatness-based control was employed for the tracking of the payload. Another application with a flatness-based approach was proposed by Aschemann and Hofer [5], who developed a control of a parallel robot driven by two antagonistic pairs of fluidic muscles. The control topology consists of a cascaded control with interior decentralized loops for each fluidic muscle and a central outer control loop for the position control of the two rod angles and the mean pressure of the two muscle pairs.

Neumann et al. proposed a cascaded model-based control with a superior position control and an internal pressure control. The experimental setup consists of a fluidic muscle on a uniaxial test-stand and is loaded with a mass, which is modeled as a spring-mass oscillator with low damping. The model-based control contains characteristic diagrams describing the force-pressure-stroke relationship of the actuator.

Ahn and Thanh [2] observed that fluidic muscles lack of damping ability, thus they applied an active damper with magneto-rheological fluids. The tuning of the damper was synchronized with the muscle control using neural networks. The experimental setup consists of an antagonistic pair of fluidic muscles which drive an external inertial load through a revolute joint. In another application, Ahn and Thanh utilized neural networks [3] for the modification of a PID controller in order to be capable of controlling a two axes pneumatic muscle manipulator consisting of two pairs of fluidic muscles.

Furthermore, Lilly and Chan [12] proposed the modification of a PID controller by applying an adaptive fuzzy PD control and a non-fuzzy integral branch for the tracking of a single pneumatic muscle loaded with a mass on a uniaxial test stand.

An example of a fluidic muscle driven parallel platform is the *airmotion ride*. It was constructed by the FH Bochum in corporation with Festo Company [79, 61]. The *airmotion ride* is a physical motion-simulator for driving application. In this setup, the platform which carries the driver's seat is held by six fluidic muscles, and the motion of the manipulator is synchronized with a computer simulation rendered on a screen in front of the platform by using a steering wheel and accelerator/brake pedals as interfaces between the physical simulator and the virtual simulation. The muscles are actuated with pressure control valves.

Later, Yao et al. [103] developed a three-legged parallel manipulator driven by fluidic muscles. The platform is supported at its center point with an additional rod which is fixed rigidly to the base and is connected with a spherical joint to the mobile platform. The manipulator allows for three rotations, and the position control of the fluidic muscles is performed with adaptive control. The fluidic muscles are inflated with fast-switch valves and the valves are controlled with pulse-width modulation (PWM).

Denkena et al. [98] designed a fluidic-muscle driven parallel platform with 6 degrees of freedom, each leg consisting of 6 fluidic muscles. In this setting, three muscle actuators are responsible for the contraction of the corresponding actuator and the other three provide the extension of the leg. It is intended to use this hexapod platform as a six dimensional damping element on the TCP (tool center point) of industrial robots, which are imposed with high contact forces at their end effectors, as e.g., in handling of forging processed parts. That means that the hexapod must be able to reproduce different stiffnesses, which is realized with a stiffness control and a superposed position control. Furthermore, the hexapod can be applied as a haptic device (joystick) for the tracking of a serial robot. The control is realized by a PID controller in combination with characteristic diagrams of the pressure-force-stroke relationship. In this respect, the dynamic behavior of the pressure increases and decreases is not modeled.

In [81], a concept is described in which fluidic-muscle driven hexapods are arranged sequentially, forming a snake-like manipulator. Each fluidic muscle in this concept is enclosed with a corresponding prestressed coil spring for the realization of tensile as well as compressive forces. No further publication was found about this concept, in terms of the applied control or the realization of the mechanism.

Fluidic muscles were also applied in walking robots. Quinn et al. designed a quadruped robot emulating the walking of a dog, each leg consisting of three antagonistic pairs of fluidic muscles. An interesting issue of the design is that the fluidic muscles which are not activated (inflated) were allowed to flex between the insertion points of the joints. The fluidic muscles were controlled by pulse-width modulation using switching valves. Moreover, the standard flanges of the fluidic muscles were removed and replaced with custom end-plugs for adjusted fixation.

Another walking robot using fluidic muscles is the *air bug*, which is a six-legged insect-like robot with eight fluidic muscles for each leg. The fluidic muscles are used with antagonistic pairs for the prescription of three joint angles at each leg. One joint angle, which is affected with the major torque is driven by two doubled pairs of fluidic muscles. Also, in this type of walking robot, the pneumatic muscles are activated by pulse-width modulation using fast switching-valves. In this respect, it was complained about loud noises, which is due to the impulsive transmission of the compressed air. This can be resolved by proportional directional control valves. Another concept of pneumatic muscles are the pleated muscles. They were developed by Daerden [17] as a response to the drawbacks of the braided McKibben-like PAMs, as e.g., the dry friction inside the material which leads to hysteresis. The characteristics of pleated muscles are that of a membrane

which consists of several pleats in the axial direction. If the muscles are inflated, the pleats will be unfolded and the muscles contracted. It is reported that it can be inflated without material stretching and friction involved in the material as it is the case in McKibben muscles [18]. In this setting, material deformation can be kept to a minimum by choosing a high tensile stiffness material, as e.g., paraaramid where friction and hysteresis are nearly eliminated by the principle of folding/unfolding, and because no outer braid or netting is used. However, it is shown that in this case the actuator force is a nonlinear function of stroke, which is very high for low strokes and increases rapidly when the actuator is shortened towards its maximum contraction.

The pleated muscle has been applied on an experimental setup of a knee joint with an antagonistic pair pleated muscles [93] and was also applied on a walking biped called *Lucy* [94]. Despite this new type of pneumatic muscles, however, it is a fact that McKibben-like braided muscles are still widely used when it comes to the use of pneumatic muscles in robotics and haptic devices. The pneumatic muscles which are used to drive the platform described in this thesis are standard fluidic muscles from Festo Company.

Physical devices for investigation of spine motion

Here, it is distinguished between mechanisms which are applied as physical surrogates of spine segments, and devices which are used for experiments with spine probes. In terms of physical surrogates, in 1972 Melvin et al. [63] designed a mechanical device for reproduction of the human neck. They applied universal joints of steel and aluminum plus intervertebral discs made of rubber. The model allowed for flexion, extension and lateral bending. The rotation and elongation with respect to the vertical axis was not possible. A further physical neck-model was realized by Culver et al. in 1972 [16]. They used viscoelastic elements which were connected by spherical and revolute joints in order to reproduce the workspace of the human neck. In the early 1980's, Kabo and Goldsmith utilized silicon for the emulation of intervertebral discs, ligaments and muscles. They mounted a water-filled skull on vertebrae made of fiberglass-reinforced resin. The model allowed for transient saggital-plane pendulum-loading.

Later, Deng and Goldsmith [32] developed a complex physical replica of the upper human spine including the head-neck and upper-torso region. They regarded the effects of muscles, intervertebral discs and ligaments for the determination of mechanical parameters which lead to injuries in this region. The model consists of a water-filled cadaver skull as well as vertebrae, sternum and ribs made of plastic. The intervertebral discs and ligaments were of silicon rubber and the muscles were made of fabrics. The complete physical model was mounted on a supporting sled running on rails. The system was loaded (1) with inertia forces by impulsively braking the sled and (2) through direct head impacts using a steel ball. The results were validated with a three-dimensional numerical model [33] for the determination of the head-neck motion and the behavior of the corresponding tissues under dynamic loading.

More recently, Nelson and Cripton [70] designed a physical surrogate mechanism for the human neck which was aimed at simulating head-first impacts leading to axial compressive neck injuries. The surrogate mechanism allows for both sagittal rotation and compression between adjacent vertebrae in the sagittal plane. The structure contains stacked aluminum vertebrae with a layer of rubber sheets between each vertebrae pair. The centers of rotation are represented with a slot and bolt system at each vertebra. The device was applied on two different test rigs, (1) a vertical test rig for reproduction of axial impacts imposed on a surrogate head connected to the surrogate neck and (2) a test bed for transmission of defined rotations to the vertebrae column for flexion/extension testings. The experiments were performed with different preloads of the vertebrae column realized with a cable system fixed to the bolts. The kinematics in both experiment types are determined by tracking markers and planar photogrammetry.

With regard to mechanisms which were solely applied for experiments with vertebrae probes, Moroney et al. [68] applied a test rig in order to determine the behavior of cadaver cervical-spine segments. The vertebrae pairs were mounted between a lower base and an upper mobile platform, where the base plate could rotate about its vertical axis and could be fixated in four orientations. The mobile platform has a frame with four concentrically arranged grips. Each grip has vertically arranged pulleys which can be loaded with forces, allowing for flexion/extension, lateral bending, shear and rotation about vertical axis. The pose was identified with dial gauges referenced to steel balls, which were mounted on the frame.

Shea et al. [84] have used a mechanism for the determination of force-displacement curves of the medium and lower region of the cervical spine. The cadaver specimen consisted of three adjacent vertebrae, of which the lowest was fixated on a lower mobile platform, and the top vertebra was fixated to a load cell. The apparatus consisted of three hydraulic cylinders arranged in parallel allowing two translations and one rotation in the plane. The device was applied for testings in the sagittal plane of the vertebrae.

Di Angelo and Jansen [47] employed an experimental set-up for the in-vitro extension of a human neck. The entire region from vertebrae C2 to T1 with its full range of motion was examined. To this end, the neck was inverted and the C2 vertebra was fixated on a rigid base frame. Next to the frame a guided vertical linear actuator was positioned with a certain offset, which was connected to a cylindrical lever over a revolute joint. The lever itself was guided by a slot allowing prismatic motion and was connected to the vertebra T1. Thus, it was possible to apply a torque on the specimen leading to a defined extension. The physical model was validated with a virtual computer model of the human neck which intended to analyze the influences of instant axes of rotation (IAR) of cervical vertebrae.

An experimental setup which applied a 6-DOF parallel platform was developed by Stokes et al. [88]. The mechanism was designed according to the Gough-Stewart platform using six linear actuators consisting of stepper-motor driven lead screws. The device was used for determining the 6×6 stiffness matrix of a pig lumbar vertebrae pair. In the corresponding set-up, the lower vertebra

was fastened to a rigid base pedestal and the upper vertebra was fixated to a mounting plate, which is linked to the mobile platform via a 6-DOF load cell. Six linear encoders were attached in parallel to the actuators. In order to determine the stiffness matrix, the three respective translations and rotations were performed sequentially, while the six actuator strokes and force/torque components were recorded.

Computer models of cervical spine motion

Virtual computer models of the cervical spine can be developed by applying multibody systems or full scale finite-element methods. In order to develop these computer models, one needs to set up mathematical models, which serve as basic approaches. The first mathematical approach which described the dynamic response of the spine to vertical acceleration was set up by Latham [58] in the late 1950's. Subsequent work increased the number of degrees of freedom and allowed for two-dimensional analysis. These models, which include the individual structures of the spinal motion segments, have been developed in order to describe aircraft ejections and whiplash injuries [74].

In the early 1970's Panjabi [72] developed a three-dimensional mathematical model of the spine, in which the vertebrae were described as rigid bodies which are interconnected with spring-damper elements. For each vertebrae pair, 21 stiffness and damping constants have to be defined in order to achieve a realistic simulation. Later Huston and Advani [44] described a complex three-dimensional mathematical head-neck model for the determination of the center of mass displacements, velocities, and accelerations of the head and neck resulting from externally applied impact forces.

The model incorporates the fundamental anatomical components and regards corresponding anatomical restrictions by integrating a joint stopping mechanism. The model was validated with responses from direct frontal and occipital (from behind) impact experiments on human cadavers and sled tests conducted on human volunteers. In 1984, Goldsmith and Deng [31] investigated the dynamic response of a numerical, three-dimensional head-neck-model resulting from lateral impacts and accomplished validation with corresponding data of a physical head-neck-model and tests with volunteers.

A very comprehensive mathematical head-neck model was developed by de Jager [22] for the investigation of the dynamic behavior resulting from impact loads. To this end, he began with implying a basic model with only a few anatomical elements and called this a *global head-neck model*. It was implemented using the multibody part of the integrated multibody/finite-element software MADYMO. The model consisted of a rigid head and the rigid vertebrae, which are connected with three-dimensional, piece-wise linear, viscoelastic elements. These joints reproduced the behavior of the intervertebral discs, the ligaments and the facet joints. The model was validated with frontal-impact tests of volunteers driving on sleds. Subsequently de Jager introduced

a *detailed segment model*, in which the area of the upper and lower cervical spine were emulated individually. The model includes separate representations of the intervertebral discs, ligaments and facet joints.

The intervertebral disc is described as six parallel connections of a linear spring and a linear viscous damper for each of the six degrees of freedom. The ligaments are incorporated with six straight line tensile force elements describing the nonlinear viscoelastic behaviors of the ligaments. Furthermore, the interactions between the facet joints are modeled as a frictionless contact of two hyperellipsoids. As a last step, de Jager integrated the components of a *detailed segment model* into the *detailed head-neck model*, in which he also implied the muscle characteristics according to Hill [41].

Kecskeméthy, Lange and Grabner [54] developed a computer method involving analytical geometric solutions for the contact problem between the facet joints, which were modeled as the contact of two cylinders using the multibody C++ library M□□BILE. With this computer model, the kinetostatics and dynamics of the intervertebral motion could be computed by a factor of 200 times faster than with conventional biomechanics software.

Besides describing the vertebrae as rigid bodies with interconnecting elements one can also include finite-element methods. FEM modelling allows one to consider full effects of the mechanics of intervertebral motion, including contact mechanics, surface gliding, and deformation [91]. For such models, a number of industry standard programs have been developed, such as MADYMO, ATB and LSDYNA3D. However, these models have the drawback that for actual computations a great number of biologic parameters are required that are difficult to obtain. Moreover, FEM models are computationally very slow and prohibit their use for online and real-time simulations as required for numerical control.

1.3 Historical review of parallel platforms

The motivation for the development of parallel robots in the last decades originated from the drawbacks of serial robots. Serial robots are known as being compliant at higher loads, featuring high inertia and low precision [21]. The reason for this is the structure consisting of serially linked-together cantilevers and the number of involved moving masses. The general definition of a parallel robot according to Merlet [65] is that it is made up of an end-effector with n degrees of freedom, and of a fixed base, linked together by at least two independent kinematic chains. Actuation takes place through n simple actuators.

The advantages of parallel robots compared to their serial counterparts are that of higher stiffness [75], higher load capacity and increased precision. These properties arise from the fact that in a parallel mechanism the end effector is linked to several chains in parallel. Hence, the loads on the

end effector can be distributed on all affiliated links. This means that each chain carries only a portion rather than the complete load transmitted from the end effector.

Referring to the nature, it is known that the bodies of load-carrying animals are supported on multiple in-parallel legs. Further, human beings tend to utilize both arms simultaneously for lifting higher loads, and for precise work as writing only the three fingers rather than the whole arm are moved [21]. Obviously besides all these advantageous properties of parallel mechanisms, there exist difficulties with parallel manipulators. First of all, the workspace of a parallel robot compared with its own dimensions is relatively small. This is exactly an issue, in which serial robots are superior, since the ratio of a serial robot's workspace size to its own geometric size is high.

Moreover, it must be regarded that at certain configurations of the actuated joints (e.g. telescopic struts, slides), parallel manipulators would not anymore support the forces transmitted from the end effector. Besides this, it can also happen that in certain configurations the end effector may get struck and cannot be released unless forcibly dismantling elements of the mechanism. Both situations where the stiffness is lost at the end effector or it gets locked in a certain pose are called configuration singularities. It is significant that the scheduled workspace of the parallel manipulator does not include these singularity points and that these points are far away from the workspace boundaries. Further, due to the parallel arrangement of the actuators, the attachment points have to be selected such that collision between the struts is avoided. Because of the complexity of the structure with many passive joints, it is significant to manufacture and assemble with strict tolerances [9]. And it should be noted that also the stiffness of a parallel manipulator could be low if the applied actuators are too compliant.

Since the topic of this thesis is the development a spatial parallel manipulator with six degrees of freedom, the historical review is given exclusively on spatial parallel mechanisms with three to six degrees of freedom.

In the late forties Eric Gough, an automotive engineer of Dunlop Rubber and Co., invented a concept of a parallel robot with six degrees of freedom (Figure 1.2) which was intended for experiments with tyres. For the industry as well as academia it is seen as a revolutionary concept with the most sustainable effects on nowadays existing parallel robots. The pioneering characteristic property of Gough's platform was the parallel arrangement of length-variable struts which is still widely applied to the structure of today's parallel robots.

The prototype of Gough's platform concept was built in the early 1950's [35] and started its operation in 1955. The mechanism was mainly designed for emulating landing situations of aero-tyres, allowing for positioning and orientation of the fixated tyre. The wheel was driven with a conveyor belt placed below and it was possible to measure the tyre wear and tear under various conditions. The moving element is a hexagonal plate which is connected to the six struts with spherical joints, and the struts were connected to the base with universal joints. At the very beginning the extensible struts were manually adjustable screw jacks, which were later upgraded with motor drives.

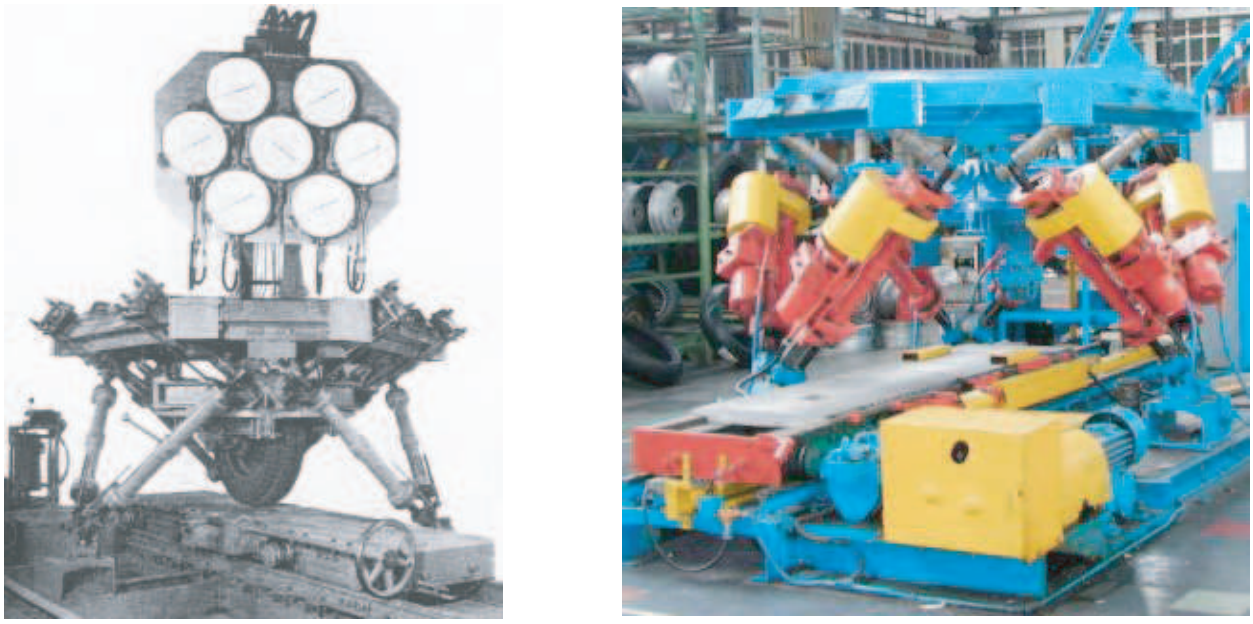

Figure 1.2: Gough platform developed for tyre testings [36]

The mechanism was operated until 2000 and was then shifted to the British National Museum of Science and Industry where it can still be visited. In 1965 Stewart proposed a 6-DOF parallel platform for use as a flight simulator [87]. His concept shown in Figure 1.3 consisted of a triangular mobile platform, which was connected to three actuating systems by spherical joints. Each actuation system consisted of two extensible struts which were both connected to a rod which can rotate around its axis. The upper strut (Figure 1.3) was fixed with the other end to the mobile platform with a spherical joint. The lower strut is linked with its other end to the body of the upper strut with a revolute joint.

Stewart also mentioned that it is possible to joint the ends of the strut pairs at one attachment of the platform, which would then match the Gough platform. It is to be noted that it was after Stewart's publication that general interest had increased under researchers on 6-DOF parallel manipulators and Stewart's impact on that development was that he proposed his mechanism for flight simulation. Due to the fact that Stewart's publication had become a reference for researchers dealing with parallel manipulators, even mechanisms which were built similar to the octahedral shape of Gough's platform were called Stewart platforms. Recently, authors have started to call these mechanisms Gough-Stewart platforms in honor of both inventors.

Moreover, in 1962 Klaus Cappel an engineer from Franklin institute was assigned for improving an existing 6-DOF vibration system. He developed a mechanism which featured the same octahedral arrangement of the Gough platform (Figure 1.4). This device was patented in 1967, but as a motion simulator for the application as a helicopter flying simulator [65], the filing of the patent took place in 1964. Bonev mentions that Cappel and Stewart had developed their ideas before knowing of each other or having any knowledge of Gough's already existing platform [7]. Today's existing flight simulators of all types are using the principles of Gough's and Cappel's octahedral platform structure with extensible struts and universal joints at the base and spherical joints at the moving

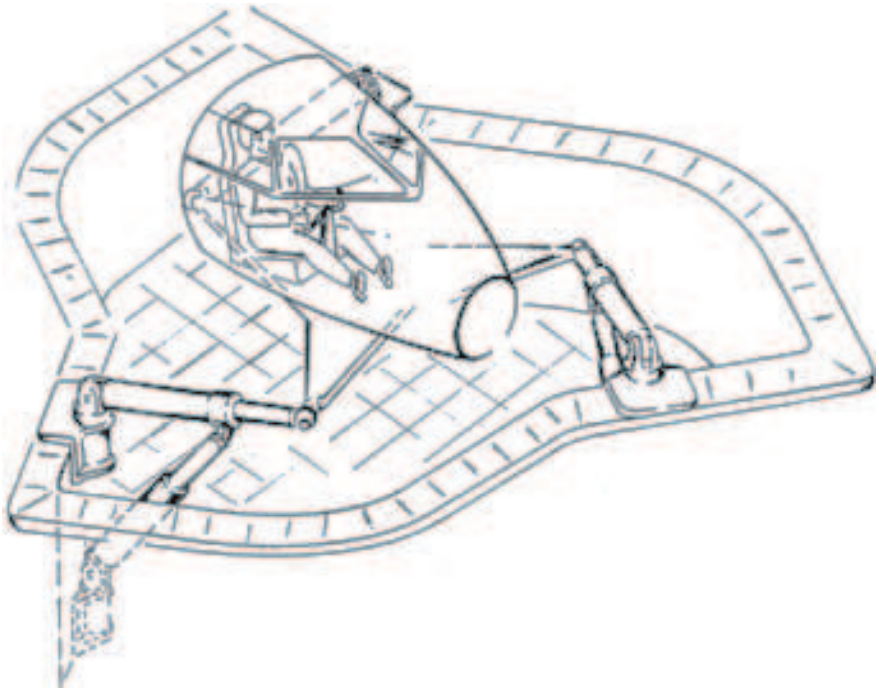

Figure 1.3: Flight simulator concept of Stewart [87]

plate. A flight simulator is shown in Figure 1.5, made by CAE (Canadian Aviation Electronics) and applied here at the flying training center of the dutch airline KLM. There are also companies which are developing parallel structures in motion simulators for ships, trains or trucks or even entertainment facilities [65].

Another important application field for parallel manipulators is the machine tooling industry, specifically for milling machines. The advantage is that the parallel structure provides large stiffness during the workpiece cutting which increases the manufacturing accuracy. It has to be regarded that in general the workpiece is fixated below the tool of a milling machine, due to handling matters. Hence, a milling machine featuring a parallel structure is very often built in hanging position with the base at the top and the end effector with the tool center point at the bottom. Thus, the design of such a milling machine requires a frame which carries the bottom oriented parallel mechanism. A five-axis milling machine in parallel structure made by the Japanese manufacturer Okuma is also built in this bottom oriented position (Figure 1.6). The variation of the tool center point is performed by electrical motors changing the strokes of the rods.

It must be noted that the parallel mechanisms have not yet considerably penetrated into the machine tool industy. Parallel mechanism are not yet applied on large-scale production of milling machines, they are still under progress in various research laboratories or manufactured in very small numbers by a few companies. One reason for this is the small workspace.

A very successful industrial application of a parallel mechanism is the Delta robot, which was initially developed at l'École Polytechnique Fédérale de Lausanne by Clavel in 1988 [15]. Figure 1.7 shows a Delta made by ABB. It is a so-called tripod featuring three degrees of freedom. Each chain consists of an actuated revolute joint at the base which is connected to a lever. The lever is

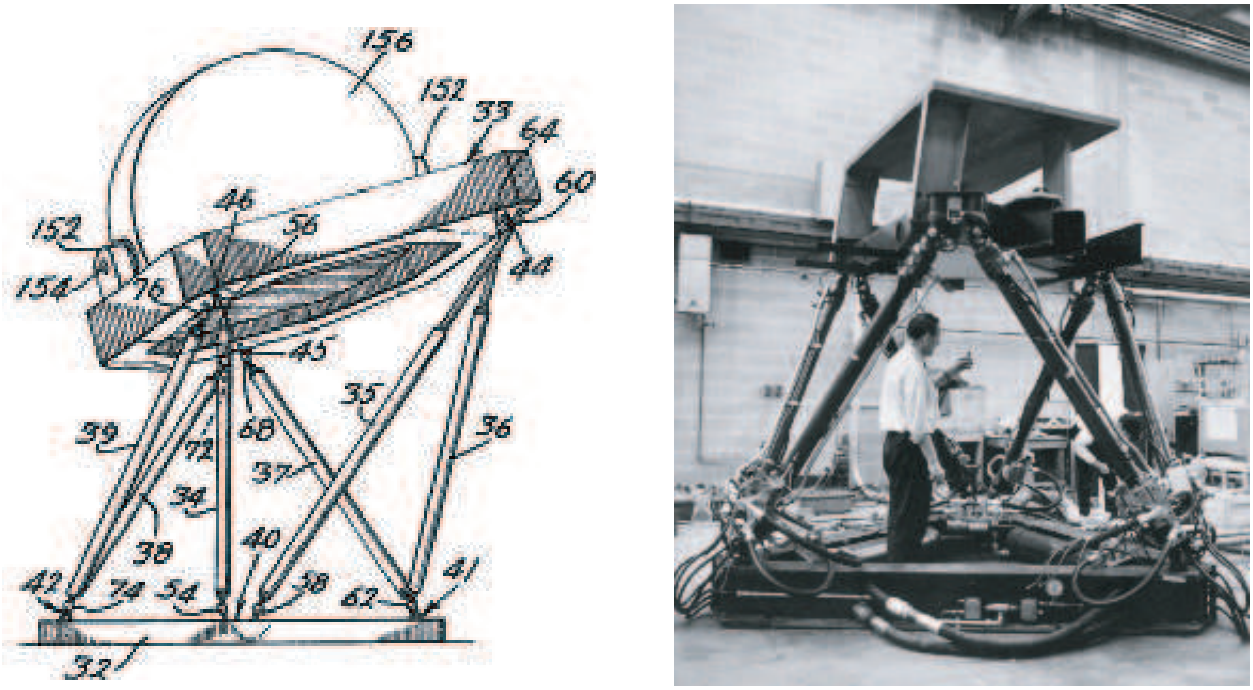

Figure 1.4: Prototype of Klaus Cappel

connected to a parallelogram (four-bar linkage) with a revolute joint [65]. The other end of the parallelogram is connected to the mobile platform using again a revolute joint. The mechanism allows the platform to fulfill three translations. The arms are generally made of carbon fiber and lead to low moving masses combined with the stiff structure of the three-legged robot. The Delta robot has been used successfully for about a decade in pick-and-place, assembly and packaging applications with high speeds. ABB has sold more than 1800 of its *flexpicker* robots (Figure 1.7) since its production was launched [29]. And with the expiry of the key patent, other manufacturers are entering the market with own made Delta robots. Some of them have modified the typical structure, e.g., Festo is using linear actuators controlled with servo motors and Adept Technology is applying four parallelogram-legs for providing additionally a vertical rotation of the platform.

The development of parallel manipulators for the medical field is still in the early stages, as only a few of the prototypes have entered the field. Especially the need of multi-axis haptic devices for surgeons implies several possibilities for parallel manipulators. Haptic devices can be useful for tasks in which visual information is not sufficient and may cause unacceptable manipulation errors. The aim of haptic devices is to provide the user with a feeling of the situation [6].

In Figure 1.8, a concept of a surgeon-assisting parallel robot is shown, which was made in cooperation of the Fraunhofer Institute for Manufacturing Engineering and Automation (IPA) and Physik Instrumente. The concept is intended for surgery requiring high precision at critical parts of the human body. No information was given about the application of this concept on a real surgery. A parallel manipulator which has been applied at numerous operations is depicted in Figure 1.9. The six-legged mechanism is designed for spinal operations, it is directly mounted on bony structure of the patient close to the operation place. It is used for stabilization procedures of the spinal column

Figure 1.5: Flight Simulator at KLM made by Canadian Aviation Electronics

by inserting screws. The robot dictates the surgeon the entry points and trajectory according to a preoperative plan [90].

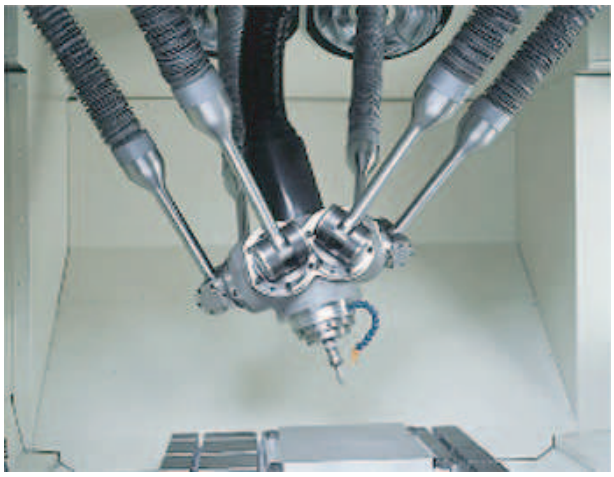

Figure 1.6: 5-axis milling machine (OKUMA Cosmo Center PM-600)

Figure 1.7: Delta robot of ABB for pick-and-place

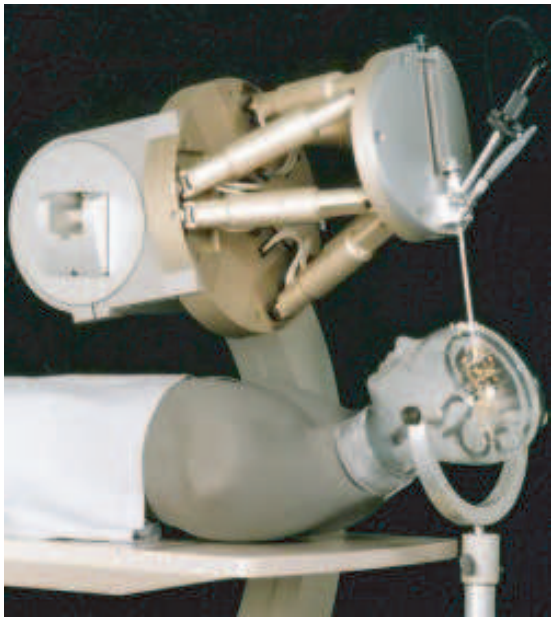

Figure 1.8: Surgical assisting hexapod (Fraunhofer Institute/ Physik Instrumente) [95]

Figure 1.9: Spine surgery assisting hexapod (Mazor Surgical Technologies) [90]

2 Physical Properties of Cervical Spine Motion

In this chapter, the basic biomechanical properties of a cervical spine vertebrae pair under quasistatic load without influences of muscle forces is described. From the mechanical point of view, the spinal column has to fulfill two different tasks. On the one hand, it must feature high stiffness in order to sustain external loads and for keeping the trunk of a human body in stable position. This is made possible with a complex system of ligaments and muscles inside and around the spinal column, which is activated and controlled by the central nervous system such that the human trunk is kept in equilibrium. On the other hand, the complete spine has to be flexible enough for allowing necessary motion, which is achieved by the combination of all of its connected vertebrae. The human spine consists of 24 vertebrae, of which the first seven vertebrae make up the cervical spine. The sections below are named thoracic spine and lumbar spine (Figure 2.1). The cervical spine

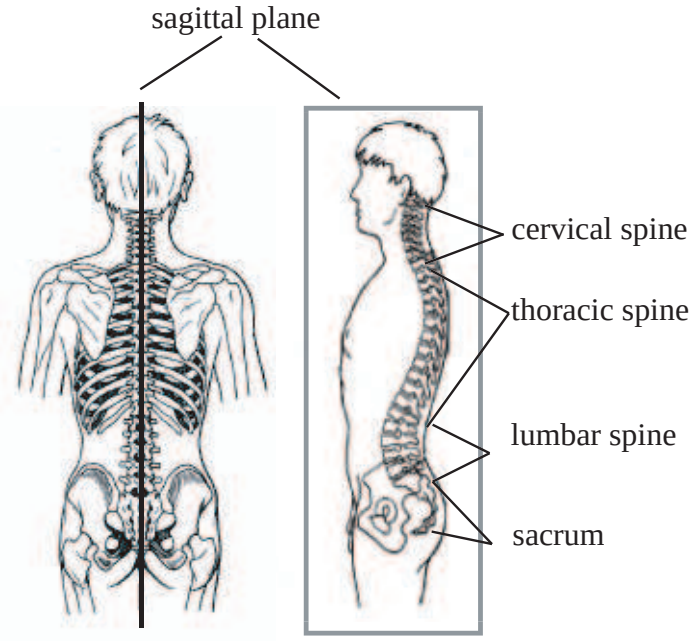

Figure 2.1: Complete spinal column [50]

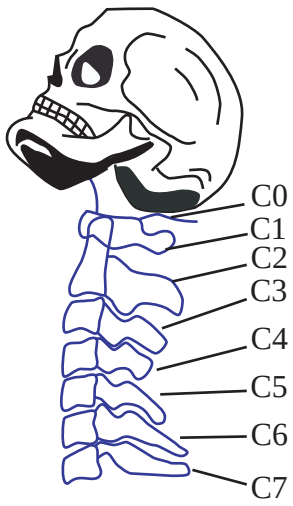

Figure 2.2: Cervical spine

is located between the vertebrae C1 and C7 (Figure 2.2). C0 indicates the occipital region of the skull. The first and second vertebra are different from each other, and they are both different from

the lower five vertebrae. Due to these differences, the cervical spine is divided into the lower and upper cervical spine.

The function of the cervical spine, is to carry the cranial load (head) and to allow the basic motions of the head and neck as shown in Figure 2.3. The basic movements of head and neck are forward

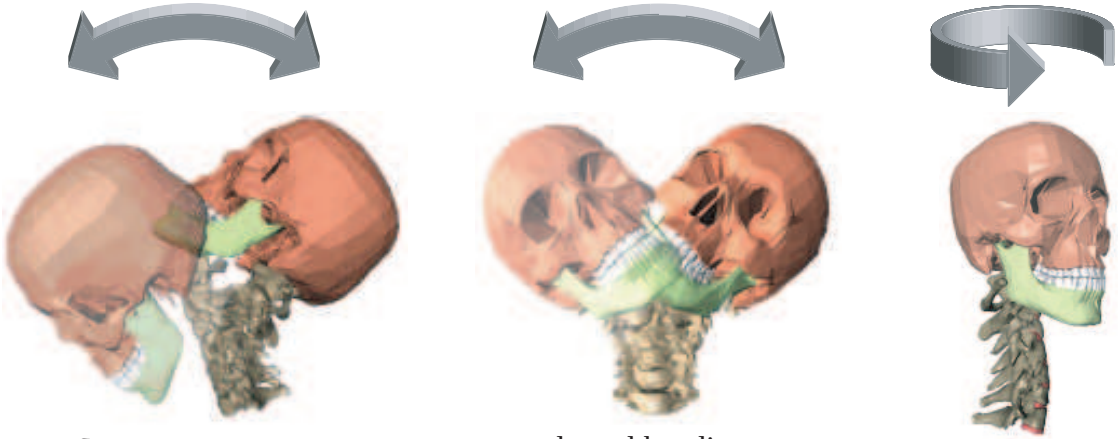

Figure 2.3: Basic movements of the cervical spine [57]

and rearward bending, referred to as flexion and extension, and lateral (sideward) bending and axial rotation.

Although two adjacent vertebrae feature a low amount of relative motion, it is the sum of the vertebrae motions which makes the larger mobility of the considered spinal sections possible. Since in the current work the aim is to reproduce physically the motion of the lower cervical spine, the vertebra C5 depicted in Figure 2.4 is considered for explaining the physiological units of the lower cervical vertebrae. The lateral view on the cervical pair C5-C6 is depicted in Figure 2.5, indicating where the front and rear side of the vertebrae are. The main part of a vertebra consists of the vertebral body, which is a round block of bone. Together with both sides of the arch and the vertebral body the *foramen vertebrale* is built leading to the the vertebral hole. From the sequence of all vertebral holes the vertebral canal is obtained, which gives space for spinal cord and nervous system.

The spinous process and the transverse processes located respectively at the posterior and anterior side of the vertebra serve as attachment points for muscles and ligaments. The intervertebral disc lies between the vertebral bodies of two adjacent vertebrae, and consists of two units. The center of that disc, the *nucleus pulposus* consists of jelly like substance containing loose fibers. The *nucleus pulposus* is surrounded by concentric layers of tough fibers (*annulus fibrosus*) which are connected to the corresponding vertebral bodies, such that it operates as a concentric belt of ligaments holding the vertebrae together when there are tensile stresses. Hence, the function of the interior unit of the disc is to absorb the loads when the spinal column is compressed. The intervertebral disc allows for vertebrae motion in all six directions (three translations and three rotations). The uncovertebral and facet joints (Figure 2.5) guide and constrain this motion. Uncovertebral joints are small joints that

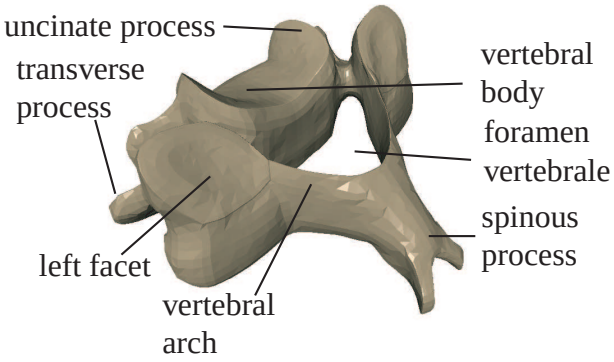

Figure 2.4: Cervical vertebra (C5)

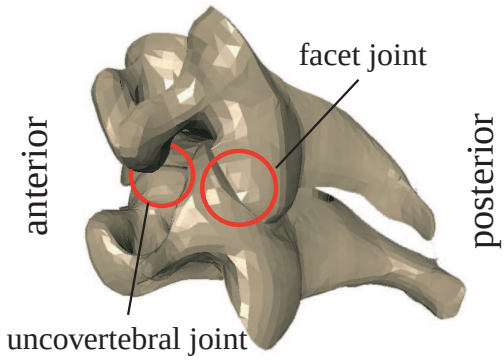

Figure 2.5: Pair of cervical vertebrae (C5-C6)

are located at the uncinate processes, on each lateral side of the vertebral body. The uncovertebral joints are coated with cartilage. Further, each vertebra has two lower facet joints and two upper facet joints, referred to as inferior and superior articular facets of a vertebra. The articular facets are almost flat and covered with articular cartilage. Both, uncovertebral joints and facet joints are synovial joints that allow for sliding motion due the articular cartilage, and which are restricted by a fibrous capsule [30].

Ligaments are bands of tissue that connect bone to bone, they allow spinal motion within physiologic limits and prevent excessive motion to protect the spinal cord. They resist tension, and fold at compression; the major ligaments of the lower cervical spine are depicted in Figure 2.6. The anterior longitudinal ligament is located at the front side of the vertebrae, starts at the cranum (had) and ends at the sacrum (2.1). The posterior ligament extends along the whole spinal column and ends up at the tail bone.

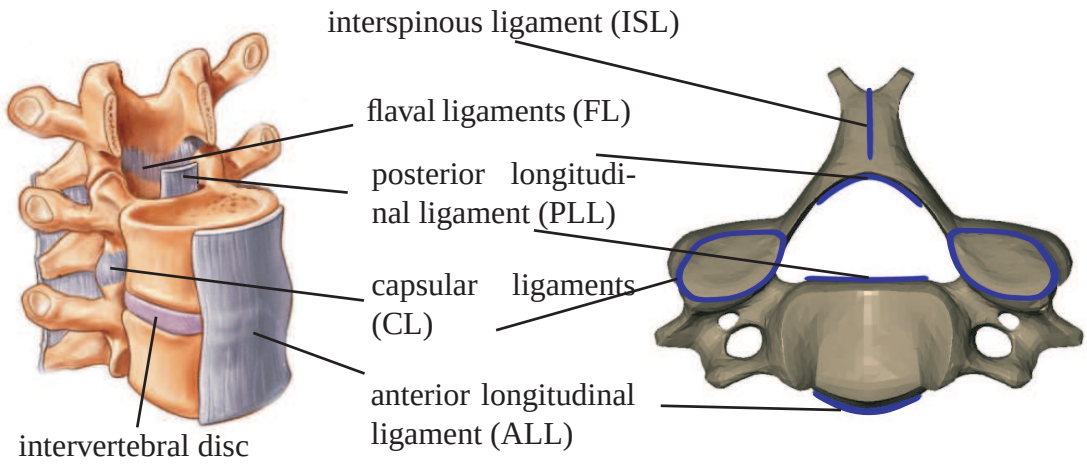

Figure 2.6: Ligaments and their insertion points

The flaval ligaments consist of robust and elastic tissue belts connecting the archs of two adjacent vertebrae, thus building a tissue barrier at the rear side of the vertebral canal. The interspinous ligaments are very short ligaments connecting the spinous processes. The joint cavities of the facet

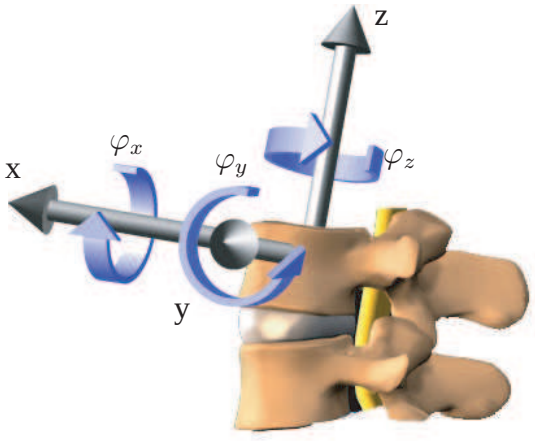

Figure 2.7: Vertebrae motion

abbr.	name	load	displ.
AS	anterior shear	$+F_x$	$+r_x$
PS	posterior shear	$-F_x$	$-r_x$
LS	lateral shear	$\pm F_y$	$\pm r_y$
TNS	tension	F_z	r_z
TNS	compression	$-F_z$	$-r_z$
LB	lateral bending	$\pm M_x$	$\pm\varphi_x$
FLX	flexion	$+M_y$	$+\varphi_x$
EXT	extension	$-M_y$	$-\varphi_x$
AR	axial rotation	$\pm M_z$	$\pm\varphi_z$

Table 2.1: Load and displacement directions

motion (deg)	intervertebral pairs						
	C0-C1	C1-C2	C2-C3	C3-C4	C4-C5	C5-C6	C6-C7
one side lateral bending	5°	5°	10°	11°	11°	8°	7°
combined flexion/ extension	25°	20°	10°	15°	20°	20°	17°
one side axial rotation	5°	40°	3°	7°	7°	7°	6°

Table 2.2: Motion ranges for *in-vivo* measured rotations of cervical pairs [68]

joints at two adjacent vertebrae are interconnected together with the capsular ligaments consisting of an anterior and a posterior portion surrounding the respective facet joint. The described ligaments form a robust interconnection of all vertebrae, that transforms the spinal column into a stable mechanical system, which is resistant towards the different loads on the human trunk.

2.1 Vertebrae motion

The basic setup for the definition of vertebral motion is depicted in Figure 2.7. The relative motion of the upper vertebra towards the fixed lower vertebra is analyzed. The moving frame is assumed to be located in the geometrical center of the vertebral body of the upper vertebra. In Table 2.1 the corresponding load and displacement directions are denoted.

Table 2.2 represents values for the ranges of the cervical pairs based on White and Panjabi [68]. Most of these ranges were derived from radiographic examination of volunteers. The load magnitudes, which caused the displacements in this study are not known [22]. The vertebrae pairs C0-C1 and C1-C2 allow for little lateral bending compared with the joints of the lower cervical

spine. Further, C0-C1 allows for much flexion/extension with little axial rotation, whereas C1-C2 features much axial rotation.

According to White and Panjabi [99], there is almost no translation between C0-C1, and there is no lateral translation but 2-3 mm of vertical and anterior/posterior translation between C1-C2. The vertebrae of the lower cervical spine feature coupling of rotation and translation at flexion and extension.

During the extension of the cervical spine, the motion is coupled with posterior translation while the inner section (*nucleus pulposus*) of the intervertebral disc is pushed forward. Further, the gap at the anterior side between the vertebral bodies is enlarged and the anterior fibers of the intervertebral disc's outer ring are stressed by tension. The extension of the cervical spine is limited by the stretched anterior longitudinal ligament and by the approaching spinous processes of the adjacent vertebrae at the posterior side. At flexion, the upper vertebra bends forward coupled with an anterior translation. The *nucleus pulposus* is shifted to the posterior side and the posterior part of the intervertebral disc's outer fiber layers are stressed by tension. The flexion is constrained by the stressed posterior ligament and additionally by stressed flaval, capsular and interspinous ligaments.

As mentioned above, the relative motion of two neighboring vertebrae comprises translations as well as rotations about all three coordinate axes. This means that there is no fixed center of rotation between two vertebrae as in a hip or a knee joint. This can be illustrated by regarding the planar motion of the spine in the sagittal plane during pure flexion and and extension. In this case, one can describe infinitesimal motions between vertebrae as rotations about the instantaneous center of rotation. However, the instantaneous center of rotation will change during motion and/or due to ageing or external loads. According to Penning [77] the position of the COR is mainly prescribed

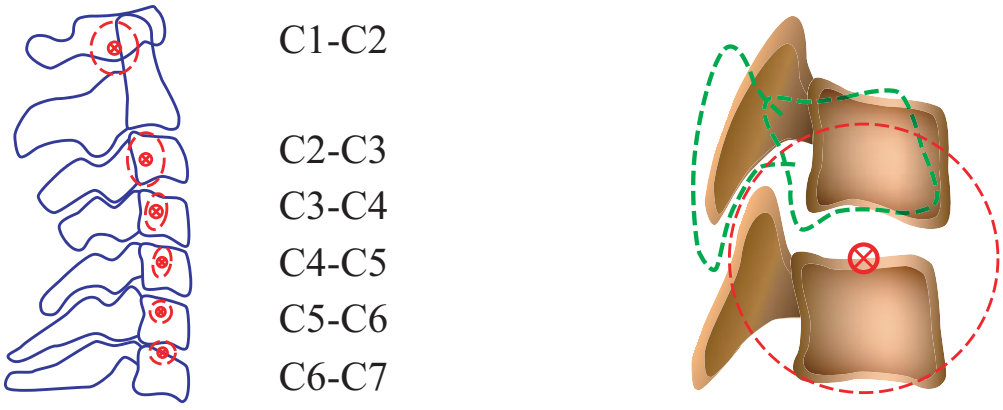

Figure 2.8: (a) Average positions of COR's and their standard deviations (b) COR determined by facet joint anatomy [22]

by the facet joints, as the spaces between adjacent facets are part of a circle with the COR of the upper vertebra as midpoint (Figure 2.8 b).

In Figure 2.8(a) the average positions of COR's in the sagittal plane determined by Dvorak [25] are depicted along with standard deviations. This shows that the position of the COR can change dramatically and that they thus do not represent a feasible way of describing intervertebral motion.

From the biomechanical point of view, a segment of the spinal column is a spatial force element whose nonlinear properties between external loads and the corresponding displacements result from the interaction of ligaments, intervertebral disc and facet joints. The effects of uncovertebral joints are not regarded for the biomechanical analysis in section 2.2, as these joints are of smaller size compared with the facet joints and no experimental data for uncovertebral joints was available.

The forces at compression are additionally absorbed by the *nucleus pulposus*, the interior part of the intervertebral disc. During flexion and extension, the facets of adjacent vertebrae undergo contact as well as free-flight phases. The tensile forces are incorporated by all corresponding ligaments including the exterior fibre ring (*annulus fibrosus*) of the intervertebral disc. The six-dimensional motion between two adjacent vertebrae displays a high degree of coupling between translational and rotational degrees of freedom due to the restraints imposed by the ligaments and muscles and the of the intervertebral disc.

Since the vertebrae of the lower cervical spine have similar properties, the cervical pair C5-C6 is selected as a representative motion segment of the lower cervical spine for the description of a vertebrae computer model (sections 2.3.1 and 2.3.2) and the development of the respective physical simulator (section 3).

2.2 Biomechanical parameters of a typical vertebrae pair

In general, the anatomic model of a cervical pair is developed with simplified approaches of their geometry and force/displacement relationships. The more simple these approaches are, the less experimentally obtained parameters are needed for the emulation of the physical effects. In other respects, an extremely rough simplification could lead to inaccurate models. For finding a compromise, in computer models of biomechanical systems very often simple geometries are combined with complex models of force/displacement relationships.

The selection of the right parameters therefore is crucial for a realistic reproduction in a virtual computer model and for the physical reproduction with a surrogate mechanism. Although several studies on the experimental parameter identification of human vertebrae were carried out, there are still parameters which are missing because they could not be obtained experimentally.

For these data voids, simplifications and estimations were necessary in order to get a full set of describing parameters. Further, due to the large differences in the biomechanical properties of the specimen and the variety of the applied experimental techniques (test stand etc.), it is difficult to choose a representative set of data for the validation of the own simulation results. In this work,

the parameters of the anatomic model of the C5-C6 cervical pair were selected according to the work of de Jager [22].

De Jager developed a detailed segment model of the unit C5-C6 imposed with typical quasistatic loads and validated this model with the experimental results of Moroney [68]. He applied the segment model as a component in a detailed head neck model comprising a rigid head and rigid vertebrae, connected through viscoelastic discs, viscoelastic ligaments and friction-less facet joints. The results showed a good matching with the response of human volunteers to impact experiments [22]. The modeling approaches of de Jager are applied in the following sections for describing the geometrical parameters and the force-displacement relationships of the cervical vertebrae.

The considered segment model consists of the two vertebrae C5 and C6, which are referenced by the frames $\mathcal{K}_5$ and $\mathcal{K}_6$, and the intervertebral disc which has the frame D (Figure 2.9). The disc center D has a fixed distance o to $\mathcal{K}_5$ according to de Jager [22].

In order to obtain full spine mobility, the model for the vertebrae pair must allow for relative motion in six degrees of freedom. The coupling is modeled as a virtual spatial joint with six degrees of

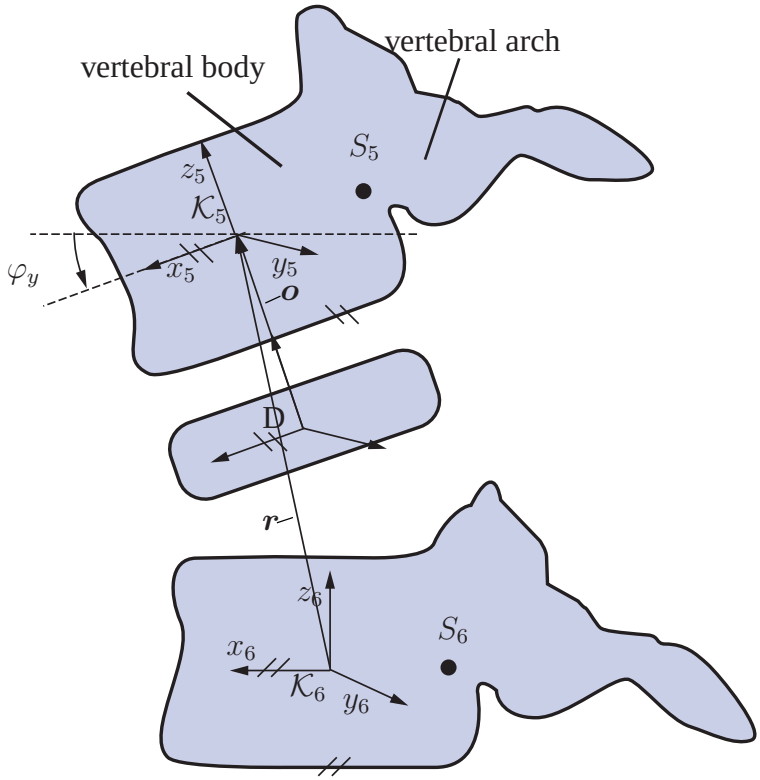

Figure 2.9: Reference frames of vertebrae (C5-C6) and intervertebral disc

freedom between the vertebrae, described as a sequential arrangement of three prismatic joints and three revolute joints.

According to de Jager, the simplifications of the geometries were performed as follows:

- the height of the intervertebral disc is measured perpendicularly to the bottom plate of the upper vertebra,

body	mass	tensor of inertia			origin		COG	orientation
	m	I_{xx}	I_{yy}	I_{zz}	r_x	r_z	s_x	φ_y
	kg	$\mathrm{kg \cdot cm^2}$			mm			deg
C5	0.23	2.3	2.3	4.5	-2.8	17.4	-8.1	-5.2
C6	0.24	2.4	2.4	4.7	-2.0	18.4	-8.3	-5.6

Table 2.3: Geometry and inertia properties [22]

- the vertebral bodies are modeled as rectangles in the sagittal plane,
- the vertebral arch posterior to the vertebral body is modeled as triangle in the sagittal plane,
- the geometrical center of the vertebral body is defined as the middle point of its rectangle's diagonal,
- the reference frames of both vertebrae are located in those geometrical centers,
- the y- and z-coordinates of the mass points (S_5, S_6) of both vertebral bodies are equal to zero.

With these simplifications, a set of parameters was used by de Jager, given in Table 2.3. The frame $\mathcal{K}_5$ is given in relation to the frame $\mathcal{K}_6$ of the lower vertebra by the vector $\boldsymbol{r}$, such that one gets the coordinates r_x and r_z given in Table 2.3. The coordinate s_x is the distance between the respective frame of the vertebra to the center of gravity of the vertebra resulting from the x-axis intersecting the line between vertebral body (rectangle) and vertebral arch (triangle). The frame $\mathcal{K}_6$ is defined relative to the frame of its lower vertebra C7. The inertia properties of the vertebrae include the surrounding soft tissues and were determined according to Walker et al. [96], assuming that the total neck mass is 1.63 kg and the density is $1170\ \mathrm{kg/m^3}$.

2.2.1 Intervertebral disc and ligaments

The viscoelastic properties of the intervertebral disc are approximated for each of the six degrees of freedom with a linear spring-damper element. In this context, Δr_i and $\Delta\varphi_i$ represent the translations and rotations relative to the i-axis of the lower body respectively. Their time derivatives are

coefficient	k_{x+}	k_{x-}	k_y	k_{z+}	k_{z-}	$k_{\varphi x}$	$k_{\varphi y+}$	$k_{\varphi y-}$	$k_{\varphi z}$
direction	AS	PS	LS	TNS	CMP	LB	FLX	EXT	AR
of load	$\mathrm{N/mm}$					$\mathrm{Nm/deg}$			
stiffness	62	50	73	68	492	0.33	0.21	0.32	0.42

Table 2.4: Stiffness properties of the intervertebral disc [68]

defined as v_i and ω_i. The approaches for the resistance loads of the intervertebral disc [57, 59] are given by

$$F_x = \begin{cases} k_{x+}\,\Delta r_x + b_r\,v_x & : \Delta r_x \geq 0 \\ k_{x-}\,\Delta r_x + b_r\,v_x & : \Delta r_x < 0 \end{cases}, \quad M_x = k_{\varphi_x}\,\varphi_x + b_\varphi\,\omega_x\,,$$

$$F_y = k_y\,\Delta r_y + b_r\,v_y\,, \qquad M_y = \begin{cases} k_{\varphi_{y+}}\,\Delta\varphi_y + b_\varphi\,\omega_y & : \varphi_y \geq 0 \\ k_{\varphi_{y-}}\,\Delta\varphi_y + b_\varphi\,\omega_y & : \varphi_y < 0 \end{cases},$$

$$F_z = \begin{cases} k_{z+}\,\Delta r_z + b_r\,v_z & : \Delta r_z \geq 0 \\ k_{z-}\,\Delta r_z + b_r\,v_z & : \Delta r_z < 0 \end{cases}, \quad M_z = k_{\varphi_z}\,\varphi_z + b_\varphi\,\omega_z\,,$$

in which F_i and M_i are the relative components of the forces and moments.

The numerical values for the stiffness coefficients k_i of the intervertbral discs are adapted from Moroney [68] as depicted in Table 2.4. Since no data was available to determine the damping coefficients, they were set as $b_r = 1000\ \mathrm{Ns/m}$ and $b_\varphi = 1.5\ \mathrm{Nms/rad}$ by de Jager. The load directions correspond to the six degrees of freedom of the relative motion of the vertebrae pair, namely anterior shear (AS) and posterior shear (PS) for x-translation, lateral shear (LS) for y-translation, tension (TNS) and compression (CMP) for z-translation, lateral bending (LB) for x-rotation, flexion (FLX) and extension (EXT) for y-rotation, and axial rotation (AR) for z-rotation. In this table, ”+” and ”-” indicate the stiffnes coefficients for pulling forces and pushing forces of the intervertebral disc.

In his experimental set up, Moroney [68] applied an axial preload of $49\ \mathrm{N}$ in order to represent the weight of the head. The description of the intervertebral disc with linear spring damper elements is an intended simplication in order to reduce computation time of the computer model.

Six ligaments of the lower cervical spine are incorporated in the model: the anterior longitudinal ligament (ALL), the posterior longitudinal ligament (PLL), the flaval ligament (FL), the interspinous ligament (ISL) and the left and right capsular ligament (CL) (Figure 2.6). The ligaments

are modeled as straight line elements transmitting only tension forces. The force of a ligament is given as

$$F_\ell = \begin{cases} F_{el}(\varepsilon) + b_\ell \cdot \mathrm{d}\varepsilon/\mathrm{d}t & : \quad \varepsilon \geq 0 \\ 0 & : \quad \varepsilon < 0 \end{cases} \tag{2.1}$$

by regarding the strain

$$\varepsilon = \frac{\ell - \ell_0}{\ell_0}$$

with ℓ for the current length and ℓ_0 for the untensioned length of the ligament. The elastic force component F_{el} is prescribed with a piecewise linear force-displacement curve.

The viscose component of the ligaments force is described with the damping coefficient b_ℓ, and was set to a relative small value of $300\ \mathrm{Ns/m}$ in comparison with the damping coefficient of the intervertebral disc.

The applied characteristics for the elasticity behavior is based on the data of Chazal et al. [13] and Myklebust et al. [69]. Chazal described the nonlinear force-strain properties of the ligaments at three characteristic points as depicted in Figure 2.10. He represented the data in dimensionless

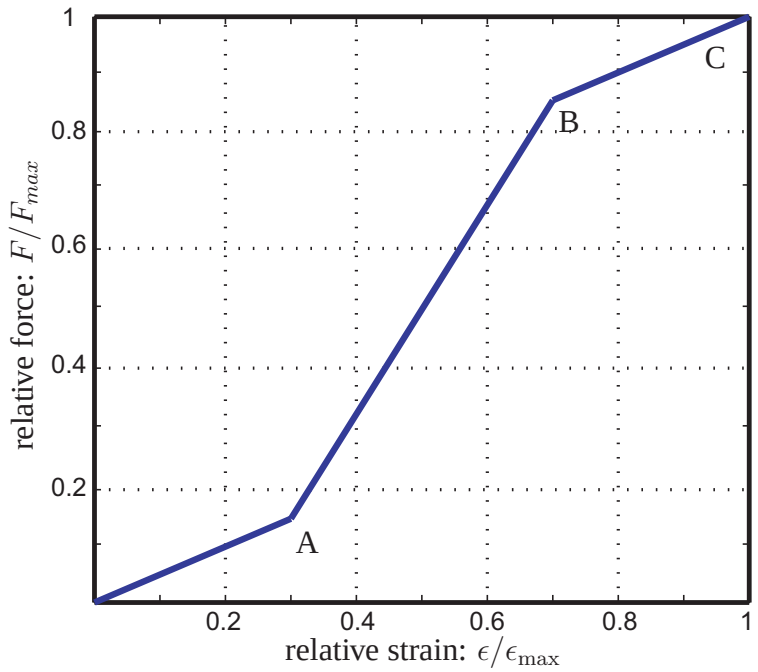

Figure 2.10: Average force-strain curve of ligaments [22]

form with the force relative to the failure force F_{max} and the strain relative to the failure strain ε_{max}. Only three of Chazal's 43 examined ligaments belonged to cervical vertebrae. Because cervical spine ligaments are weaker than the ligaments of other vertebrae according to [69], de Jager

ligament	A		B		C	
	$\varepsilon/\varepsilon_{\max}$	$F/F_{\max}$	$\varepsilon/\varepsilon_{\max}$	$F/F_{\max}$	$\varepsilon_{\max}$	F/N
ALL	0.24	0.11	0.8	0.88	0.58	111
PLL	0.22	0.12	0.78	0.9	0.45	83
FL	0.33	0.21	0.77	0.89	0.21	115
ISL	0.33	0.19	0.78	0.87	0.4	34
CL (Ø)	0.28	0.16	0.78	0.88	0.42	108

Table 2.5: Ligament parameters for C5-C6 [22]

ligament	origin C5			origin C6			undefl. length
	x	y	z	x	y	z	ℓ_0
ALL	7.7	0.0	0.0	8.0	0.0	0.0	18
PLL	-8.1	0.0	0.0	-8.3	0.0	0.0	17
FL	-25.4	0.0	-1.7	-26.3	0.0	-1.9	15
ISL	-39.9	0.0	-3.2	-47.3	0.0	-4.1	16
CL	-15.1	$\pm$ 20.3	-5.1	-12.9	$\pm$ 20.0	7.2	6

Table 2.6: Ligament insertion points for C5-C6 in mm [22]

adjusted the failure forces (see Table 2.5) F_{max} to the experimental data of Myklebust, who provided the information about the failure forces and maximal strains of almost all spinal ligaments. Here A, B and C indicate the three characteristic points (see Figure 2.10) which were determined by Chazal.

Due to the lack of experimental data for capsular ligaments, their values were assumed as the average of the other ligaments.

The untensioned lengths ℓ_0 of the ligaments are given in Table 2.6 together with the corresponding insertion points of the ligaments according to de Jager [22] in body-fixed coordinates of the coordinate frame of the respective vertebra body. In the model, the direction of the line of action of the capsular ligaments is perpendicular to the facet joints and the corresponding insertion points are located at the centers of the facet surfaces.

2.2.2 Facet joints

In addition to the six-degree-of-freedom joint, motion constraints are introduced by (unilateral) contact elements reproducing the surfaces of the facet joints. As described previously, they feature contact as well as free-flight phases. The contact phase can comprise planar, line and point contact;

the almost planar surfaces of the contact pair glide on each other with almost no friction. When the contact force vanishes, the surfaces detach from each other (free-flight phase), eliminating the geometric constraints of the facet joints temporarily. During this motion, the facet joints are pulled together by the surrounding capsular ligaments.

Panjabi et al. [73] developed an ellipsoid model and tested it for 276 vertebrae probes yielding lengths, surfaces and orientation angles of articulated facets. The facet thickness was set to 2 mm. De Jager adjusted position and orientation and applied the data for the development of the segement model of vertebrae C5-C6 including the facet joints using the software MADYMO. MADYMO offers a library of several standard contact elements. From that library, de Jager selected the articulated contact of hyperellipsoids for the emulation of the facet joints (Figure 2.11). A hyperellipsoid of degree n is defined as

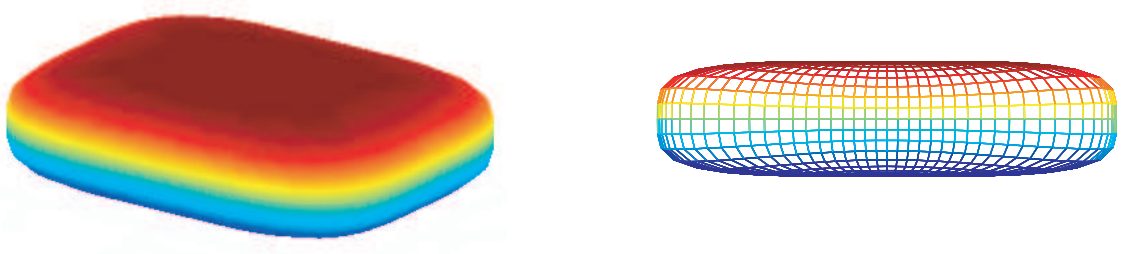

Figure 2.11: Graphical representation of an hyperellipsoid ($n = 4$, $a = 6$ mm, $b = 8$ mm, $c = 2$ mm)

$$\left(\frac{\| x \|}{a}\right)^n + \left(\frac{\| y \|}{b}\right)^n + \left(\frac{\| z \|}{c}\right)^n = 1, \quad n \geq 2, \tag{2.2}$$

where a, b, c are the axial segment lengths of the ellipsoid along the x, y and z-axes of the respective ellipsoid coordinate-frame which is located in the center of the ellipsoid. That center of an ellipsoid, which describes one of the 4 articulated facets of the vertebrae pair C5-C6, is referenced to the frame $\mathcal{K}_5$ or $\mathcal{K}_6$ respectively. The relative orientation of that ellipsoid is defined with Bryant angles with the rotation sequence of x, y and z.

The ellipsoids applied by de Jager were of 4th order. As an example the geometry data of the left facet joint is given in Table 2.7. For the position and orientation of the right facet one has to change the signs of the y-coordinate and the angle φ_y. The contact forces of the facet joints were modeled by de Jager as frictionless interactions between the surfaces of those ellipsoids. The contact force F_c is computed by the nonlinear viscoelastic approach

$$F_c = b_f \, \dot{u} + \begin{cases} 2 \cdot 10^9 \cdot u^2 & : \quad 0 \leq u \leq 3 \cdot 10^{-4} \\ 180 + 1.2 \cdot 10^6 \cdot (u - 3 \cdot 10^{-4}) & : \quad u > 3 \cdot 10^{-4} \, . \end{cases} \tag{2.3}$$

position	coordinates of center point			length of axial segments			relative orientation	
	x	y	z	a	b	c	φ_y	φ_x
	mm						deg	
C5 inferior	-13.7	20.3	-6.5	5.6	5.9	1.0	-45.6	13.8
C6 superior	-14.4	20	8.5	5.5	6.2	1.0	-50.8	13.8

Table 2.7: Geometry data of left facet joint [22]

The penetration u is the normal distance between the tangential planes of the hyperellipsoids in the contact point. The damping coefficient was chosen as $b_f = 300\ \mathrm{Ns/m}$ by de Jager.

The selected force-displacement properties has no physical background, but represents an almost rigid contact allowing some deformations of the thin cartilage layer covering the articular facets. The quadratic part provides a smooth transition of the contact stiffness from zero, when there is no contact, to $1.2 \cdot 10^6\ \mathrm{N/m}$ at 0.3 mm of penetration [22].

2.3 Virtual models of the cervical pair C5-C6

The future objective is to connect a computer simulation of the vertebrae with the control loop of the physical simulator. Hence, a computer model is required which is suitable for real-time application and online data transmission to the platform control.

In the following sections, two computer models of the C5-C6 vertebrae are presented, which were developed [57, 59] by the software MADYMO and the C++ multibody library M□BILE respectively. In section 2.3.3, the simulation results of the computer models are compared with data from experiments with human probes [68].

For the development of the C5-C6 model in the multibody C++ library M□BILE [52], Lange et al. [57] applied the set of biomechanical parameters (section 2.2) which were determined by de Jager. Since de Jager applied MADYMO in his work, Lange et al. [57] created a reference model using MADYMO with the same parameters (de Jager) in order to validate the simulation results of the C5-C6 model programmed with M□BILE. The M□BILE model was later extended by Liem et al. [59] with stable algorithms for making it suitable for real-time control loops.

2.3.1 MADYMO reference model

The software MADYMO is the world-wide standard for occupant safety analysis and is used extensively in industrial engineering, research laboratories and technical universities. In MADYMO one

can apply multibody systems as well as finite-element methods or combine both mechanical methods. To simulate a mechanical system, one has to write a data file according to certain strict syntax rules. Elements and parameters are specified by keywords and numerical data. The complete data file is then compiled and linked to the main MADYMO program, where the specified time interval is simulated. Results are written to several output files, depending on the user's specification.

After computation, using the MADYMO post-processor, the simulation can be visualized as a movie. Interactions of the user during the simulation are not possible [54]. The graphical representation of the vertebrae pair is given in Figure 2.12.

The facet joints were implemented as Ellipsoid-Ellipsoid contact interactions comprising hyper-ellipsoids of degree n = 4. For visualization purposes, the vertebral bodies were modeled as hyper-ellipsoids of degree n = 2, with no contact interactions arising from this model [54]. Similarly, the vertebral arches are visualized as elongated hyper-ellipsoids of degree n = 2, which only have graphical meaning and do not provide any physical interactions with the environment. Although the MADYMO-model was valuable in producing accurate simulation results for the re-

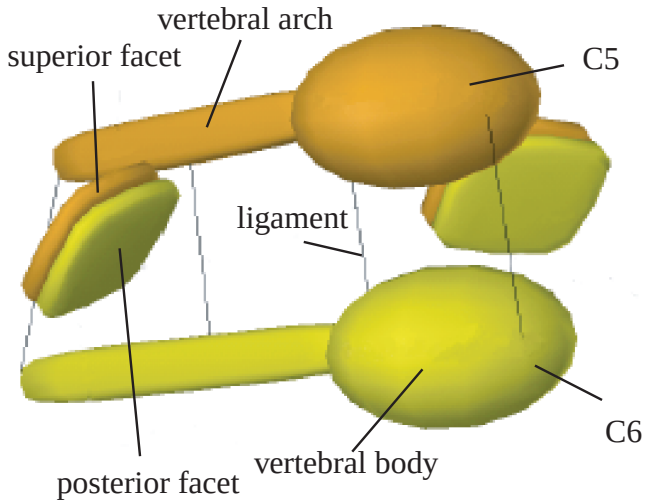

Figure 2.12: MADYMO model of cervical pair C5-C6 [57]

garded vertebrae-pair motion, excessive simulation time turned out to be a drawback in analyzing different parameter sets quickly.

For the change of the parameters, it is always necessary to proceed with a new compilation of the program. It is not possible to run a simulation which can be changed online [54].

2.3.2 Employed MOBILE model

As an alternative model of the vertebrae-pair interactions, a C++ program was developed using the object-oriented multibody package M□BILE [52].

MBILE is an object-oriented programming environment designed for the modeling of multi-body systems. Mechanical entities are represented as objects capable of transmitting motion and force across the system. Furthermore, mechanical systems can be modeled directly as executable programs or as modules for existing libraries.

This yields an open building-block system design that allows the programmer to extend the provided library in contrast to input-oriented programming packages where the user has to work with built-in functions without the possibility of extending or adapting the employed algorithms. MBILE is implemented in the object-oriented programming language C++, which provides portability and offers interfaces to three-dimensional graphic libraries for animation, such as OpenInventor. This makes direct user feedback and interaction possible, including click-and-drag features for online kinematics, statics and dynamics [54].

For emulating the effects of full spine mobility supported by the intervertebral disc, a spatial spring-damper element is applied with a serial connection of three translational and three rotational spring-damper elements with orthogonal axes. The unilateral constraints of the facet joints are implemented as the contact of the end faces of two cylinders due to the fact that the facet joints are almost flat [54]. This type of interaction renders four possible contact situations: (1 a) edge-face, (1 b) face-edge contact, (2) edge-edge contact, and (3) face-face contact, as depicted in Figure 2.13.

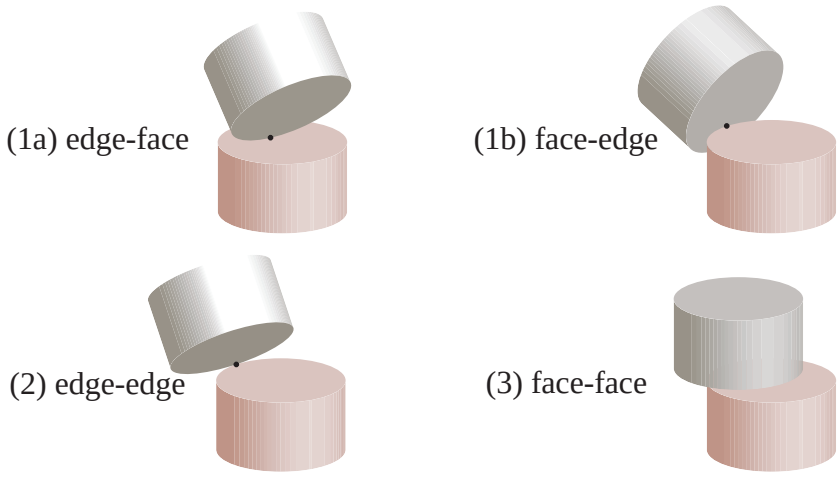

Figure 2.13: Possible contacts of two cylindrical elements

For simulating the skew contact, the *regularized impact approach* is applied by assuming that the neighborhood of the contact point is compliant and that the contact force can be computed with a spring-damper approach. The corresponding penetration u is defined as being perpendicular to the face of the cylinder which is penetrated by the edge of the other cylinder, as depicted in Figure 2.14. One hence obtains

$$u = \boldsymbol{c}^{\mathrm{T}} \cdot \boldsymbol{n_2} + r_1 \sin\alpha \tag{2.4}$$

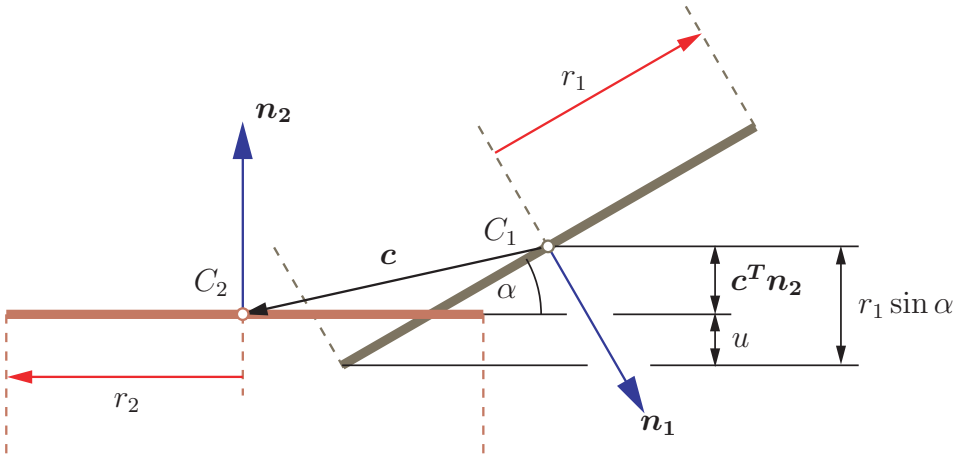

Figure 2.14: Computation of penetration u at edge-face contact

where r_1 is the radius of the cylinder (Figure 2.14) whose edge is penetrating into the corresponding face of the second cylinder whose respective normal vector is defined as $\boldsymbol{n_2}$. The vector between the center points of both cylindrical end faces is given as $\boldsymbol{c}$, and α is the inclination angle between the end faces.

For the computation of the contact force, the penetration approach of equation 2.4 is inserted into the contact-force equation which was applied by de Jager (section 2.2.2), yielding

$$F_c = b_f\ \dot{u} + \begin{cases} 2 \cdot 10^9 \cdot u^2 & : \quad 0 \leq u \leq 3 \cdot 10^{-4} \\ 180 + 1.2 \cdot 10^6 \cdot (u - 3 \cdot 10^{-4}) & : \quad u > 3 \cdot 10^{-4}\ . \end{cases} \tag{2.5}$$

The damping coefficient was chosen as $b_f = 300\ \mathrm{Ns/m}$ as in [22].

In order to provide a smooth transition of the contact point from the edge-face contact into the face-face contact (Figure 2.15) a blending function

$$|\boldsymbol{r}_{mp}| = |\boldsymbol{r}_0| \cdot (1 - e^{-C \sin\alpha}) \tag{2.6}$$

is implemented, where C is a constant. That means that the contact point p is shifted along the radius $|\boldsymbol{r}_1|$ of the cylinder, depending on the inclination angle α between both end faces.

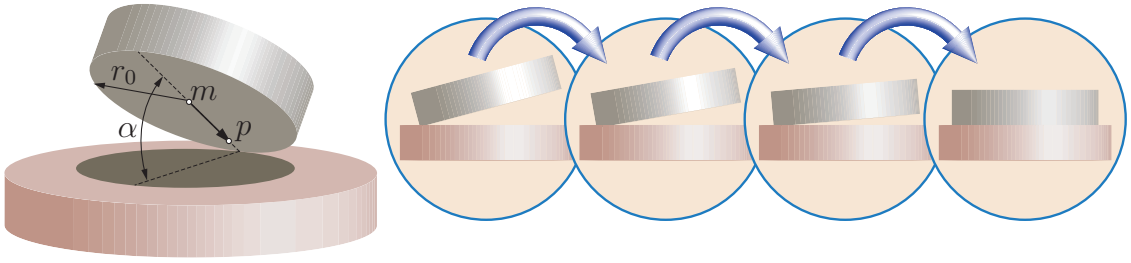

Figure 2.15: Smooth transition from almost parallel case to fully parallel case

A particular property of the used blending function is that it renders a stabilizing moment during that transition situation. Hence, no further computations and state transition tracking procedures are necessary for transition from steep to flat contact [54]. Two graphical models of different complexity for the simulation of the considered vertebrae C5-C6 were rendered as depicted in Figure 2.16. The simplified model on the left hand side of Figure 2.16 comprises only cones, cylinders and spheres, giving a rough idea of where the vertebrae locations are.

The other, more complex model, employs original 3D vertebra visual geometry, and hence renders a more realistic view of vertebrae motion. The M□BILE software package allows online user

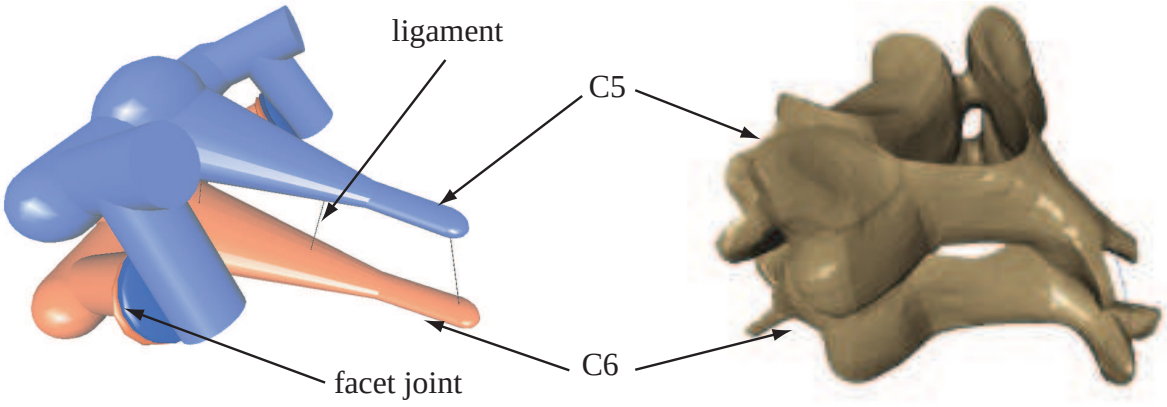

Figure 2.16: Graphical representation of C5-C6 models developed with MOBILE

interactions during the animation. Through software slider controls, the system parameters can be changed interactively. For example, the mechanism response can be controlled visually while stiffness properties of the intervertebral disc are varied [54].

2.3.3 Validation of model results with experimental data

The simulation results of the vertebrae pair models were compared and validated with the experimental results reported by Moroney et al. [68], which contain averaged force-displacement curves from experiments with fresh human segment probes of the cervical spine for 35 vertebrae segments, including nine C2-C3, four C5-C6 , six C6-C7 and four C7-T1 pairs.

Each pair was mounted into a special test stand with which external forces and torques could be induced on the upper vertebra of the respective pair. The lower vertebra was fixed to the rigid part of the test stand. The resulting displacements were then measured for forces up to 73.6 N and torques up to 2.16 Nm. For the C5-C6 segment, the lateral force was 19.6 N and the torque was 1.8 Nm.

For the validation of the C5-C6 models with the experimental results, similar loads were applied, as 20 N for lateral forces and 1.8 Nm for torques. The validation of the respective simulation

results with experimental data from Moroney are shown in Figure 2.17 for lateral bending (LB), flexion (FLX), extension (EXT) and axial rotation (AR). The experimental results of Moroney are

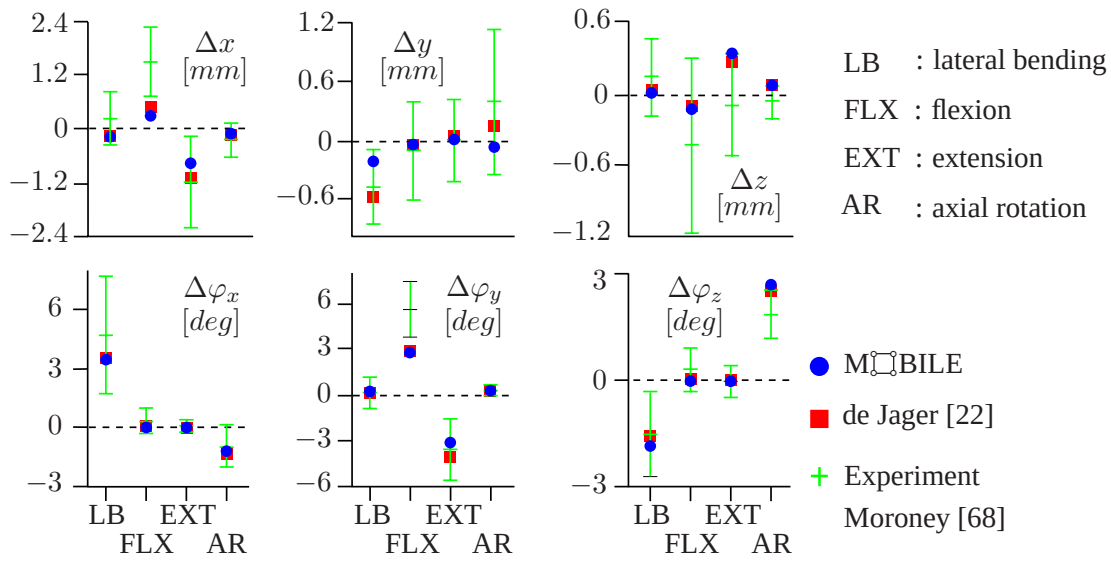

Figure 2.17: Validation of simulation results with experimental data from Moroney [68]

presented by their mean values and the standard deviations. It can be verified that the MOBILE model renders results that are not more inaccurate than the complex MADYMO model and that they are moreover close to the mean values of the experimental results.

Regarding the computation time, when there is a contact situation between the facet joints, it was observed that the computation time of the MADYMO model nearly doubled due to the use of hyperellipsoids, whereas that of the MOBILE model did not increase [57]. For instance, at extension (EXT) of the modeled vertebrae pair the computation time with the reference model in Madymo was 17 s, whereas the MOBILE model needs 3.1 s (using an SGI Indigo 2; 195 MHz; MIPS R10000)[57]. At axial rotation (AR) the MADYMO reference model requires 13.1 s. Here, the MOBILE model computes within 3.3 s.

Moreover, MOBILE has an additional built-in object called *MoStaticEquilibriumFinder*, with which the calculation of the static equilibrium can be achieved in a few iterations using a Newton-Raphson algorithm. Using this object, the static equilibrium was reached 50 times faster than before [57]. That means, in the end, the ratio of the computation time with Madymo to that one of MOBILE is about 250. The reason for this is that, besides using the *MoStaticEquilibriumFinder*, a simpler and more efficient mathematical model is used for the contact mechanics (cylinder-cylinder contact). Thus, the MOBILE model is more suitable for model-based real-time control than the full Madymo Model.

3 Design of Physical Simulation Platform

This chapter is devoted to the design of the complete platform, such as needed for the physical simulation of the cervical spine motion with six degrees of freedom. The chapter starts with a formulation of the design aims, followed by an overview of basic platform design concepts from literature. After collecting the basic properties of the actuators, the dimensional design of the platform is completed and the workspace of the manipulator is analyzed. The chapter is closed with a description of the platform prototype and its components.

3.1 Design aims

For the current design of the Hexaspine platform, the task is to find a mechanism such that the required motion ranges of the human cervical spine, i.e., the forces and the relative motion of a vertebra to its adjacent vertebra (see section 2.1), can be reproduced physically. An overview of the classified aims is presented in Figure 3.1.

The design aims are subdivided into structure-relevant ones on the left hand side and design aims which are important for the funtionality as a physical simulator on the right hand side. The de-

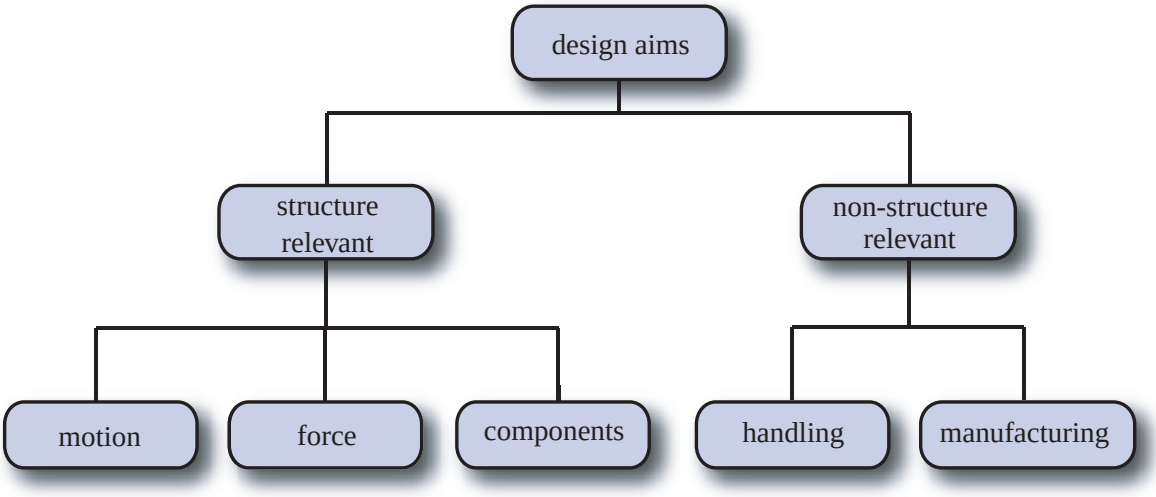

Figure 3.1: Overview of hexaspine-platform design aims

	x_{EE} [mm]	y_{EE} [mm]	z_{EE} [mm]	ϕ_x [deg]	ϕ_y [deg]	ϕ_z [deg]
min	-2	-1	-1	-10	-8	-7
max	2	1	1	10	8	7
	F_x[N]	F_y[N]	F_z[N]	M_x[Nm]	M_y[Nm]	M_z[Nm]
min	-20	-20	-75	-1.8	-1.8	-1.8
max	20	-20	75	1.8	1.8	1.8

Table 3.1: Motion and force/torque ranges for vertebrae pair C5-C6 [68]

sign aims which influence the structure of the platform are subdivided into the aspects motion, force, and integrated components, such as drives, sensors, and passive joints. The non structure-relevant design aims deal with the handling facilities for staff working with the parallel platform and manufacturing matters of the platform components. The particular design aims of the Hexaspine platform are specified in Table 3.2 and 3.3 which contain the subpoints of the aims presented in the overview of Figure 3.1.

In order to simulate the properties of the cervical vertebrae C5-C6, the workspace of the platform must feature the translation, rotation, force, and torque values of Table 3.1, which contains the force and motion ranges of the vertebrae pair C5-C6 determined by Moroney et al. [68].

A significant structure-relevant requirement is that a singularity free parallel mechanism must be designed such that the required motion and forces can be achieved without any restrictions (e.g. loss of stiffness). The platform should feature as well the possibility of mounting surrogate specimen to the end effector, which additionally requires a specific fixation device. Furthermore, it is important to choose an ideal operation point (tool center point: TCP) of the end effector which is the place where the specimen will be fixed. The operation point shall be chosen such that the required motion ranges of the cervical vertebrae can be reached with the TCP using the achievable strokes of the actuators.

In addition to the realized motion, the specimen shall be loaded with controlled forces and torques such that real conditions for cervical vertebrae are reproduced. Therefore, the mechanism has to feature a high stiffness for allowing noise-free transmission of forces to the end effector while the platform force control is running. Hence, on the one hand, an architecture providing high stiffness is to be developed, but on the other hand, it must be regarded that the moving elements of the mechanism do not have too much weight. Especially, the motion platform is to be designed under lightweight criteria such that the required pressure forces (see Table 3.1) imposed on the cervical-spine specimen are achieved.

Furthermore, due to the selection of fluidic muscles as actuators for the platform, the legs can be contracted only by about 20 % of the initial unexpanded actuator length, which consequentially leads to large leg lengths when larger strokes are required.

Generation of motion	• achievement of human cervical-vertebrae motion ranges • placement of operation point such that the required end-effector motion ranges are reached with technologically available leg strokes
Generation of forces	• force control of manipulator for the production of quasistatic forces • lightweight construction for achievement of necessary pressure forces • stiff architecture for accurate transmission of forces • target workspace must be singularity-free in order to avoid loss of stiffness • tight fixation device for vertebrae specimen
Effects of integrated components	• it must be regarded that the force of fluidic muscles is nonlinear in stroke • limitation of contraction to approximately 20 % of initial length • space for coil springs and their housings must be made available for producing pressure forces • space for sensors (position, force, pressure) and passive joints

Table 3.2: Design aims related to the platform structure

It has to be also regarded that the applied fluidic muscles have to be combined with coaxial springs in order to produce pressure forces, which makes additional elements for fixation of the springs necessary. This means that the diameter of the resulting actuator combination is larger than the diameter of the fluidic muscle ($20\,\mathrm{mm}$) which accordingly has to be taken into account for devicing a collision-free structure of the mechanism. Moreover, enough space must be provided for the sensors and the passive joints. Another aspect regarding the specific properties of fluidic muscles is that different to pneumatic or hydraulic cylinders the force/pressure relation of a fluidic muscle is variable in stroke with rapidly decreasing forces at increasing contraction of the muscle.

The design aims which do not depend on the structure of the parallel manipulator are subdivided into the contexts of handling and manufacturing matters (see Table 3.3). For handling matters, it shall be noted that the motion platform is to be designed for application in medical institutes and academic laboratories, where a clean environment must be ensured. This makes actuation systems necessary which do not contaminate the environment in health centers or labs. Moreover, the drive systems shall feature easy maintenance and shall be run by an accessible and clean power source.

This requirement was fulfilled by using pneumatic artificial muscles [38, 55], in particular fluidic muscles from Festo, which feature a clean and convenient air-pressure power source. Due to the fact that connections to compressed air are found in many laboratories, the power source for the selected actuators is easily accessible. And if there is no pressure source, the possibility of using a mobile compressor device is still convenient, as no specific fluid except air is needed.

It must be regarded that the operation point is easily accessible for operators at installation and fixation works. Further, the installation procedure for the fixation of specimen in the operation point must be as convenient as possible.

3.2 Basic types of parallel platforms

All possible design variants for the 6-DOF Hexaspine platform will consist of basic elements as passive and active joints (actuators). The basic types of joints used in each variant may be the same, but it is the way of arranging the passive and active joints in each kinematic chain which defines the specific differences of the platform variants. Thus, before presenting design variants, the basic joint types, which are used in the design of parallel robots, are introduced.

These joints are, with increasing degrees of freedom, revolute, prismatic, universal and spherical joints (see Table 3.4). Revolute joints are labeled R, while prismatic joints become P, universal joints are labeled U. It is to be noted that for spatial mechanisms universal and spherical joints are often used. Industrial universal and spherical joints are shown on the right hand side in Figure 3.4. There are problems, especially, with spherical joints, as usually models of industrial serial productions have a low range of motion.

Handling	• suitability for medical institutes and laboratories environment, enabling clean operation • easy maintenance • accessibility of operation point • convenient installation and deinstallation of specimen fixation device
Manufacturing	• low amount of play at joints • lathe process to be favoured instead of milling (accuracy) • number of parts shall be low • unambiguous assembly of components • easy to handle fasteners • suitable for frequent assembly/disassembly • flexible towards changes and newly added components

Table 3.3: Non-structure relevant design aims

Symbol	Name	DOF	Structure	Industrial Component
R	Revolute	1	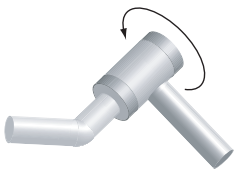	
P	Prismatic	1	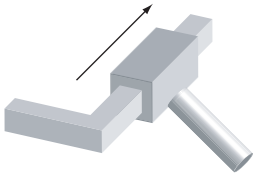	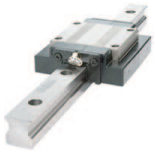
U	Universal	2		
S	Spherical	3	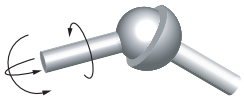	

Table 3.4: Basic joint elements

Thus, very often it is necessary to develop customized spherical joints, which will be designed and manufactured according to the individual requirements of the application. Particularly the assembly of ball and socket of a spherical joint and their way of fixation may create problems in terms of clearance, friction and manufacturing tolerances. Another method for creating a spherical joint could be the combination of a universal joint with a revolute joint; this means that the universal joint would feature rotations about two axes and the revolute joint would provide the rotation about the third axis. The joints featuring one degree of freedom are typically applied as active joints. The most common active prismatic joints are electrical linear drives, spindle drives or hydraulic and pneumatic cylinders. In terms of micro parallel-manipulators, very often piezo actuators are applied [24]. Active revolute joints usually are driven by rotary electric motors.

In general, the number of drives in a parallel manipulator is equal to the degrees of freedom of the end effector. It has to be regarded that each chain of the mechanism has to restrict at least one degree of freedom of the end effector [71]. An overview of kinematic chains applied on 6-DOF parallel mechanisms with six legs is given in Figure 3.2. Here, the arrangement of joints and drives and the connection to the base and motion platform is illustrated for different variants. For 6-DOF parallel robots with six legs the most significant kinematic chains are of $U\underline{P}S$, $\underline{R}US$, and $\underline{P}US$. The underlined joints are the actuated ones. All kinematic chains described in Figure 3.2 have

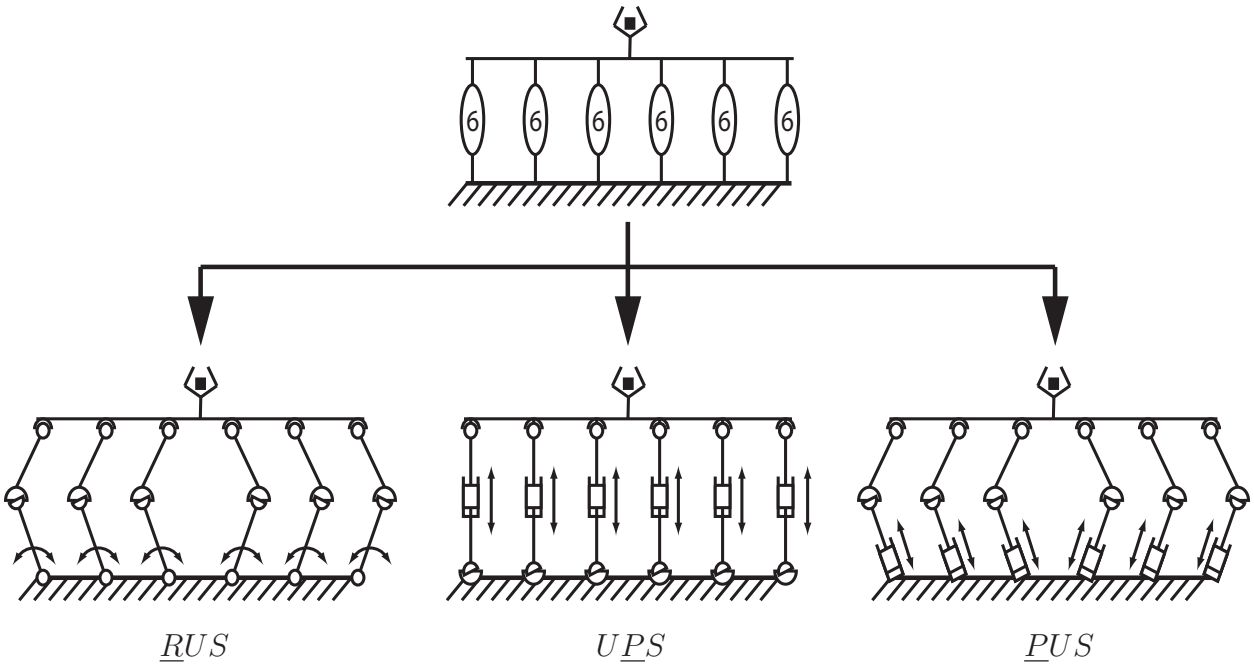

Figure 3.2: Basic chains of 6-DOF parallel robots [28]

three joints each, and the sum of the joint degrees of freedom in each leg is six. All six of these chains are arranged such that they are connected to a motion platform and a rigid base. For other architectures of 6-DOF mechanisms, different to those given in Figure 3.2, it shall be referred to Innocenti and Parenti Castelli [45], and Faugere and Lazard [26].

For the description of the degrees of freedom of a parallel mechanism, n_B defines the number of rigid bodies in the mechanism, and n_G is the number of joints, where each joint has relative degrees of freedom $f_{G_i} \leq 3$ for $i = 1, ..., n$ respectively. The addition of the joint degrees in each leg is $\sum f_{G_i} = 6$. The unconstrained motion of a mechanism with n_B rigid bodies in a K-dimensional subspace of rigid-body motion is given by

$$f = K \cdot (n_B - 1)\ ;\ K = \begin{cases} 3 & : \text{ planar motion} \\ 6 & : \text{ spatial motion} \end{cases} \tag{3.1}$$

with f defined as the degrees of freedom of the end effector. For each joint, $K - f_{G_i}$ constrained degrees of freedom will be locked, such that for the degrees of freedom of a mechanical system it holds according to Grübler-Kutzbach

$$f = K \cdot (n_B - 1) - \sum_{i=1}^{n_G} (K - f_{G_i})\ , \tag{3.2}$$

which can be written as

$$f = K \cdot (n_B - 1 - n_G) + \sum_{i=1}^{n_G} f_{G_i}\ . \tag{3.3}$$

For a six-legged mechanism equipped with the basic chains presented in Figure 3.2 one obtains $n_B = 14$ and $n_G = 18$ such that it holds

$$f = 6 \times (14 - 1 - 18) + 6 \times 6 = 6$$

for the degrees of freedom of the respective parallel mechanism by applying equation 3.3. Thus, it is verified by the Grübler-Kutzbach formulation that all platform variants, which will be described in the following subsections, feature six degrees of freedom at the end effector. This corresponds to full spatial mobility.

3.2.1 RUS Type

The first concept of a parallel robot using $\underline{R}US$ chains was introduced by Hunt [43] in 1983 (Figure 3.3). It consists of six actuated revolute joints, which are placed on the base plate. The axes of the revolute joints are in horizontal direction. Further, they are connected to rigid links by universal joints. The other ends of the links are attached to the moving plate by spherical joints. As rotary actuators are required, electric motors are best suited for this application.

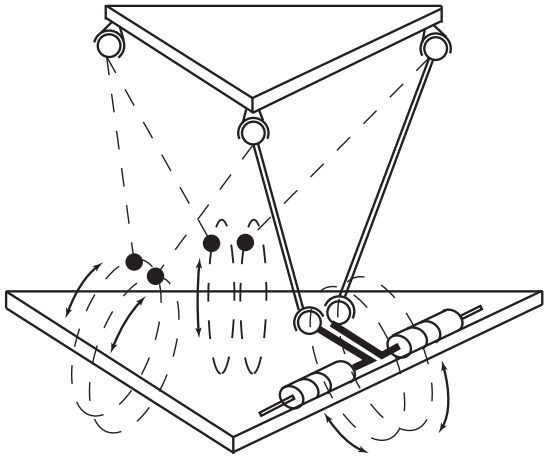

Figure 3.3: RUS type concept by Hunt [43]

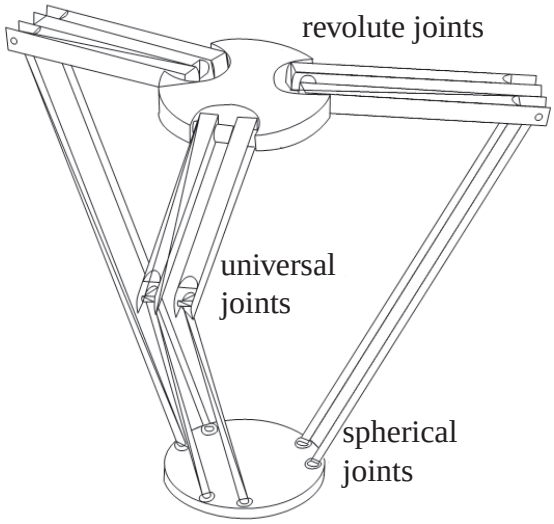

Figure 3.4: Hexa concept as illustrated by Bruyninckx [9]

Another concept of a $\underline{R}US$ type parallel robot was developed by Uchiyama and Pierrot [78, 92], who extended and upgraded the famous 3-DOF Delta robot principle of Clavel [15] to a 6-DOF mechanism named as Hexa (see Figure 3.4). The mechanism differs from Hunt's presented concept, as the links attached between the actuated revolute joints and the passive universal joints are longer. Moreover, the joint centers of the spherical joints are not arranged by three joint pairs as done by Hunt, but with six attachment points to the corresponding spherical joints leading to a hexagonal motion plate. It is to be noted that the axes of the actuated revolute joints do not have to be necessarily in horizontal direction [65].

Since fluidic muscles perform linear motion and are preselected as drives in the Hexaspine platform, they would have to be combined with an additional mechanism in order to actuate the revolute joints of $\underline{R}US$ type parallel robots. This requires an antagonistic configuration of two fluidic muscles combined with a revolute joint as depicted in Figure 3.5 or a single fluidic muscle in connection with a coil spring linked to the revolute joint (see Figure 3.6). In this case, one can also apply a rotational spring at the revolute joint itself. However, it must be regarded that the realization of rotary motion with fluidic muscles in a 6-DOF parallel mechanism leads to a complex architecture which demands too much of space per leg as it is seen in Figures 3.5 and 3.6.

3.2.2 PUS Type

Parallel robots with PUS chains are also known as Hexaslide manipulators (HSM). A general concept of an HSM from Bonev and Ryu [8] is given in Figure 3.7 and the corresponding kinematic structure is shown in Figure 3.8. The mechanism consists of six constant-length struts, which are connected to the mobile platform with spherical joints. Furthermore, six actuated slides with their corresponding rails, which are fixed to the base, are connected to the struts with universal joints.

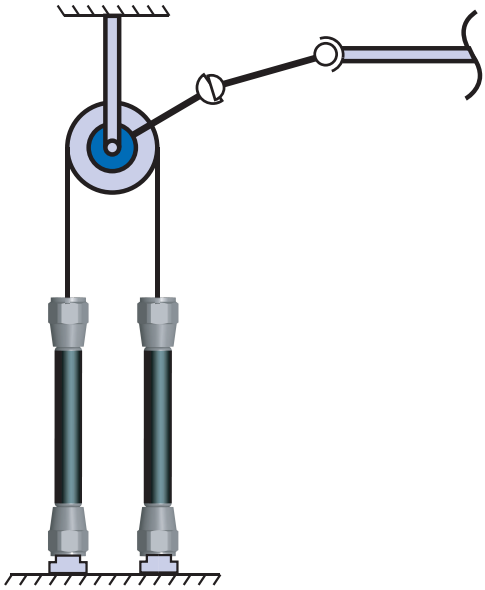

Figure 3.5: Antagonistic arrangement of fluidic muscles for one rotary drive

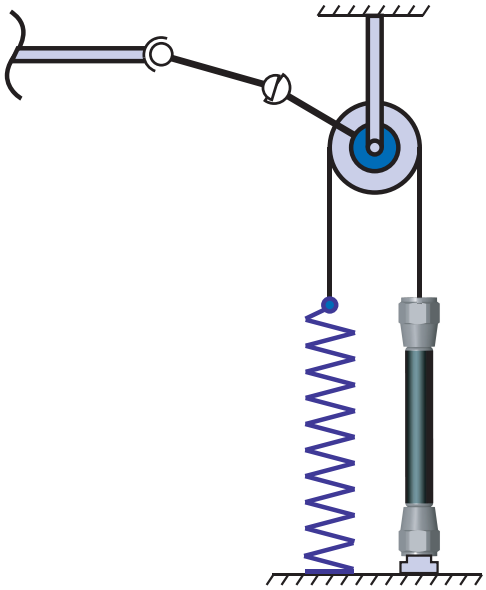

Figure 3.6: Arrangement of single fluidic muscle for one rotary drive

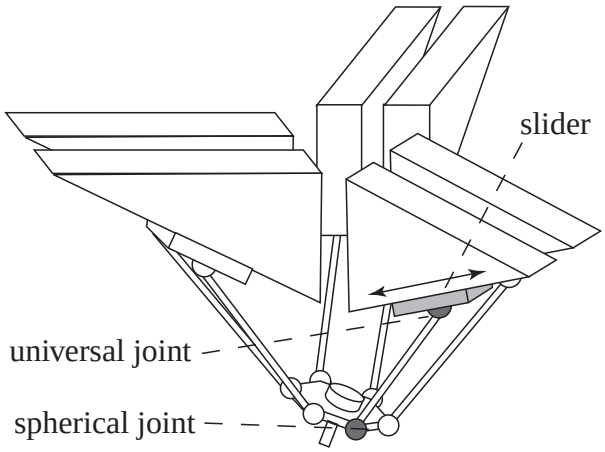

Figure 3.7: Concept of an HSM [8, 82]

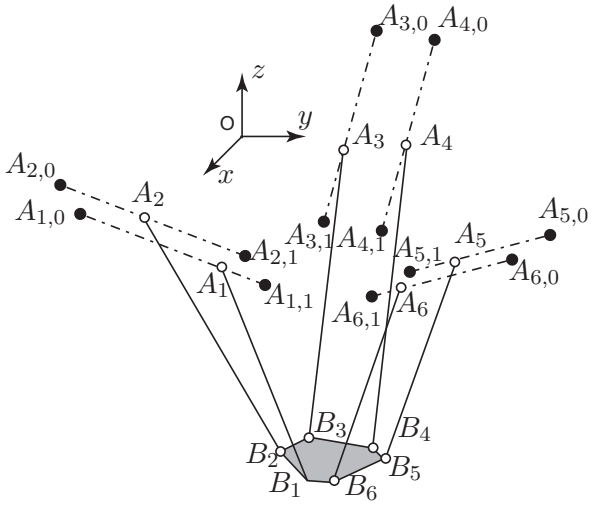

Figure 3.8: Structure of respective HSM

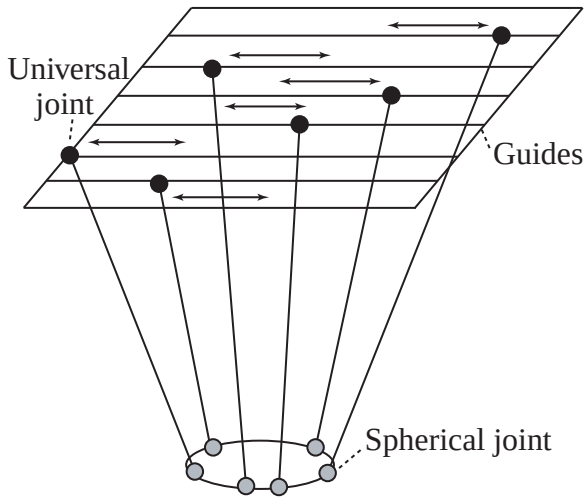

Figure 3.9: PUS structure of Hexaglide

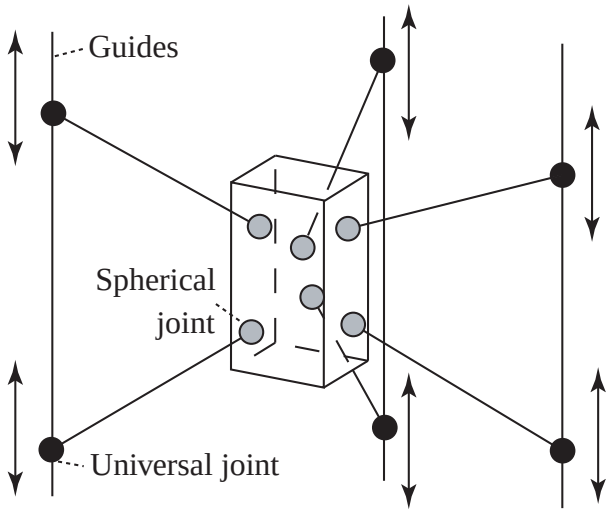

Figure 3.10: Linapod structure

The manipulator defines the position and orientation of the platform by moving the spherical joints A_i from the end points $A_{i,0}$ to $A_{i,1}$ with all six slides.

Parallel robots using $\underline{P}US$ chains feature advantages that result from the fact that the guides are fixed rigidly to the base plate. The actuators do not change their orientations, as the actuator can only move in the guided direction (prismatic joint) and the constant-length struts just need a low-diameter. Hence, it is achieved that the collision risk of the actuators is reduced. Moreover, a low moving mass is obtained and the center of mass is kept close to the base [8].

It is to be noted that in PUS chain robots the direction of the linear guides can be variable [65]. For instance, the hexaglide [42] of the ETH Zürich (Figure 3.9), which was developed for machine tool application, consists of horizontal prismatic drives. The prismatic actuators are realized by slides which are mounted to six horizontal guides arranged in parallel to each other. The workspace can be varied by changing the distance between the end-stops of the slide-guide connections and by changing the corresponding lengths of the rods.

A $\underline{P}US$ parallel mechanisms, which has prismatic drives in vertical direction, has been realized at the University of Stuttgart with the Linapod [80, 100] (see Figure 3.10). This mechanism was also developed for application in machine tooling. In particular, the Linapod consists of three vertical guides, having two actuated slides each, such that 6-DOF is achieved at the tool center point of the Linapod.

The main drawbacks of PUS chain robots compared to other parallel structures are that they have a relatively small workspace, as the motion ranges of the slides are not completely transmitted to the end effector due to the tilted directions of the rods between the platform and the slides. The workspace analysis is also more elaborate [8] due the more complicated relationship between the platform pose and the actuator strokes, as the platform is not directly linked to the actuated joints. Bonev [8] remarks that it is difficult to conceive and implement a geometric approach for the workspace determination of these manipulators.

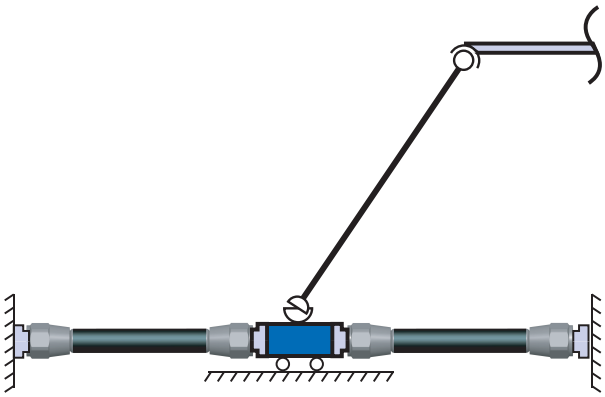

Figure 3.11: Antagonistic arrangment of fluidic muscles for one linear drive in PUS configuration

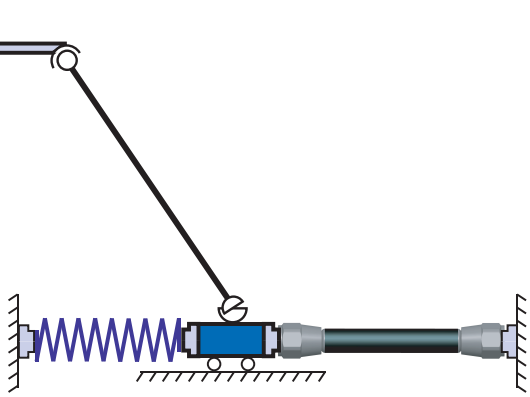

Figure 3.12: Arrangement of single fluidic muscle for one rotary drive

Concerning the application of fluidic muscles on $\underline{P}US$ chain robots, if the arrangement would be similar to that one of the Hexaglide [37] or the Linapod [100], the fluidic muscles would have to be connected to slides, which are guided on linear rails, as depicted in Figures 3.11 and 3.12. The actuation can take place with two antagonistically working fluidic muscles for each leg as depicted in Figure 3.11 or a single fluidic muscle in combination with a coil spring (Figure 3.12).

Further, a rod must be placed between the slides and the motion platform, hinged with a universal joint to the slides and with a spherical joint to the platform. This would also mean that a special frame has to be built which carries the slide-guide connections of the fluidic muscles, in vertical (Linapod, Figure 3.10), horizontal (Hexaglide, Figure 3.9) or tilted direction (general HSM manipulator, Figure 3.7 and Figure 3.8. Such a frame would make more space necessary for the hexaspine platform if it was built as a parallel manipulator with $\underline{P}US$ chains.

3.2.3 UPS Type

The UPS type robot, known as Gough-Stewart platform, is also called Hexapod or General Parallel Manipulator (GPM). It is the most common and best investigated platform structure and was realized in various applications. The first prototype of this structure was built by Gough in 1955 [35] as a test rig for automobile tyres (see Figure 1.2 in section 1.3).

A UPS robot consists of two rigid bodies, the base and the platform which are connected through six legs with universal joints at the base and spherical joints at the moving plate (see Figure 3.13). The legs consist of actuated prismatic joints. The position and orientation of the platform in space are prescribed by changing the length of the six legs. When the positive aspects of parallel manipulators are mentioned in comparison with serial robots, it is very often referred to 6-UPS type robots. Due to the fact that UPS type robots are driven by prismatic actuators, various types of linear actuators powered by different energy sources are available, such as electric, hydraulic, pneumatic

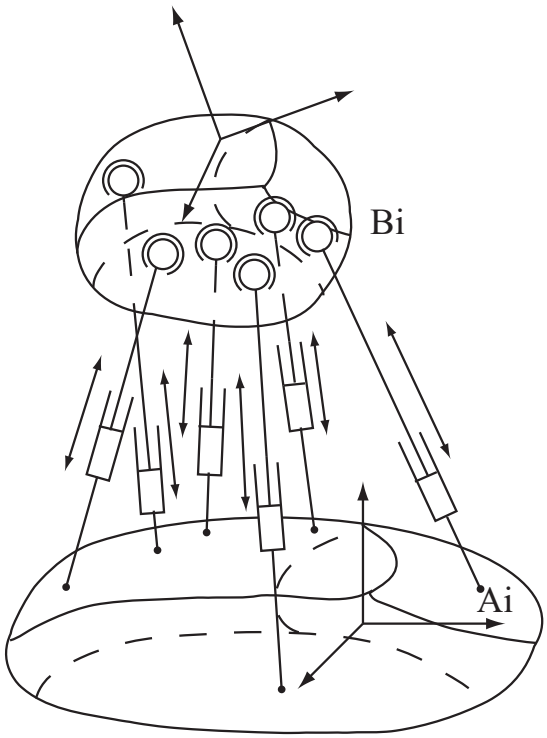

Figure 3.13: Gen. topology of $U\underline{P}S$ robot [65]

Figure 3.14: $U\underline{P}S$ robot (Physik Instrumente)

or piezo-electric actuators. In Figure 3.14 a hexapod from Physik Instrumente is shown, which is driven by electric motors.

The advantages of a GPM over serial manipulators are higher stiffness, higher accuracy, and high load-carrying capacities [21, 4]. Further, the mechanical structure features higher natural frequencies and is less sensitive to variation of external loads [76]. Therefore, this type of manipulator is used in various applications, e.g., in flight simulators, machining centers and precise positioning devices [67].

In comparison with hexaslides ($\underline{P}US$) described in the previous subsection, the workspace of hexapods is larger and its computation is less complicated, as the translation of the actuators is directly transmitted to the motion platform. Therefore, a U<u>P</u>S type parallel robot features a more compact architecture, since additional space for surrounding slide-guide components is not required except the space for the linear actuators and the joints between mobile platform and the base. Though being the most commonly applied 6-DOF structure in parallel kinematics, it also bears typical drawbacks of parallel kinematic machines as the aspect of singularities [34].

In terms of force singularities, the mechanism would not be able to hold its previous amount of stiffness in certain poses such that loads being imposed on the end effector cannot be supported anymore by the actuated joints [86, 20]. Further drawbacks of parallel robots with U<u>P</u>S chains are that forces from the end effector are directly transmitted to the actuators in axial direction of the legs, which could lead to lower stiffness at the end effector when the linear actuators are compliant. Moreover, the risk of collision between the actuators is higher, compared to a $\underline{P}US$ robot, since the prismatic actuators change their orientation when the platform is moving. This can be problematic

if the actuators may have wider dimensions due to additional elements, e.g., sensors etc. Assuming that the constant-length rods of $\underline{P}US$ type parallel mechanisms are always of low diameter with lower mass than linear actuators, which are equipped with further components as sensors etc., it can be said that a further drawback of U<u>P</u>S type parallel robot is that of larger moving masses in comparison with $\underline{P}US$ parallel robots [8].

Further, Masory and Wang [97] pointed out that the accuracy of a Gough-Stewart platform is mainly affected by the manufacturing tolerances of the components, as e.g., the passive joints. The workspace of a GPM can be varied with the arrangement of the attachment point of the joints on the moving plate and the base plate. Merlet introduced three variations of the Gough-Stewart platform which differ by the locations of the attachment points [64]. The SSM (Simplified Symmetric Manipulator) has a hexagonal base plate and motion platform, the $TSSM$ (Triangular Simplified Symmetric Manipulator) has a triangular motion platform and a hexagonal base plate (see Figure 3.15), and the $MSSM$ (Minimal Simplified Symmetric Manipulator) has a triangular base plate and a triangular motion platform as well.

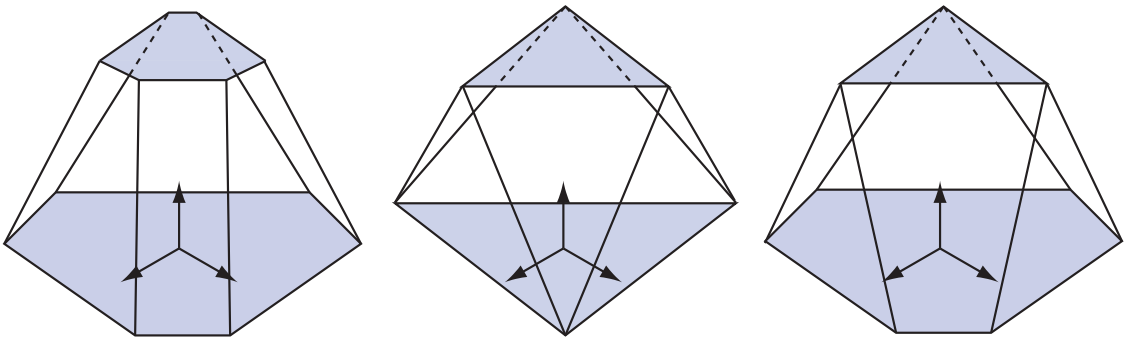

Figure 3.15: Joint center variations of U<u>P</u>S type robots [64]

Merlet considered three types of hexapods with similar size and assumed that the ranges of the leg strokes are same and defined that the attachment points lie on circles with the same radius for each type of the considered mechanisms. He found out that the variant in which both plates are hexagonal (SSM) will have the largest workspace, larger than the TSSM, while the MSSM gained the smallest workspace. It is to be noted that a SSM-type Gough-Stewart platform is also more convenient in terms of manufacturing and assembly because the joint centers in the moving plate and the base plate are attached at six different points, and moreover this lowers the risk of collision.

Although the SSM would have the largest workspace, it must be regarded that a larger workspace is always related to a lower stiffness of the structure. That is why the MSSM, with both triangular base and motion plate, will have the stiffest architecture but smallest workspace. Moreover, the limitations of the universal and spherical joints in a U<u>P</u>S type robot will influence the workspace

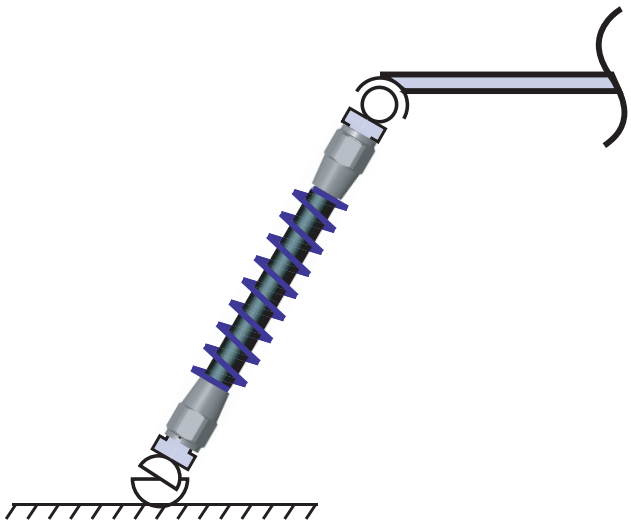

Figure 3.16: Arrangement of fluidic muscle in a U$\underline{P}$S leg

size and shape significantly. Additionally, it is obvious that also the leg lengths of a Gough-Stewart platform and their stroke ranges will have significant effects on the workspace volume.

In a $U\underline{P}S$ configuration, the integrated fluidic muscles would be linked directly to the motion plate by using spherical joints (see Figure 3.16). The connection to the base is done with universal joints. Thus, a special frame carrying rails of respective slides, as it is the case with $\underline{P}US$ chains, is not necessary. This means also that additional linking elements as rods are not placed between actuators and platform except the spherical joints. However, with this type of kinematic chain in a fluidic-muscle driven parallel platform an antagonistic arrangement of two fluidic muscles per leg is not possible. This can be circumvented by combining a fluidic muscle with a coaxial spring, as depicted in Figure 3.16).

3.3 Geometric and quasistatic properties of the selected actuators

Fluidic muscles (Figure 3.17) are actuators consisting of a rubber and filament structure, such that when inflated a contraction force is produced. The contraction force results from the lateral expansion of the fibers inside the filament structure when the muscle is inflated with compressed air. Thus, they resemble the functionality of biological muscles. The maximum expansion of the fibers are limited by the angle $\alpha_{\max} = 54.7$ [38].

A drawback of fluidic muscles is that the actuator force is nonlinear in stroke and therefore requires a control algorithm that considers the particular nonlinear properties. The corresponding characteristics of a fluidic muscle are described in Figure 3.18, in which the forces for constant-pressure lines are plotted in a diagram over the contraction of the muscle given in percent of the initial muscle length. Here, negative forces are pulling forces. The maximum stretched position is -3 %, and

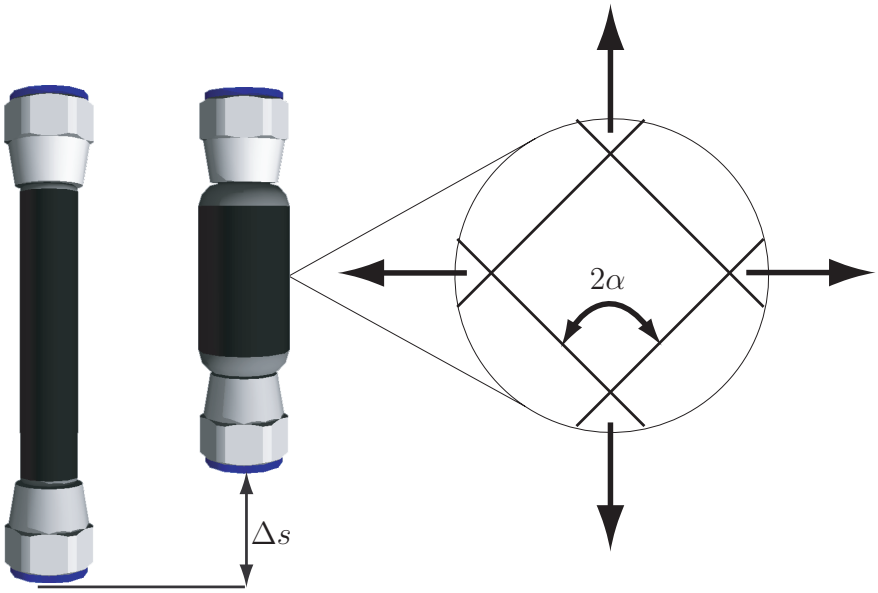

Figure 3.17: Fluidic Muscle and structure of its fibers [38]

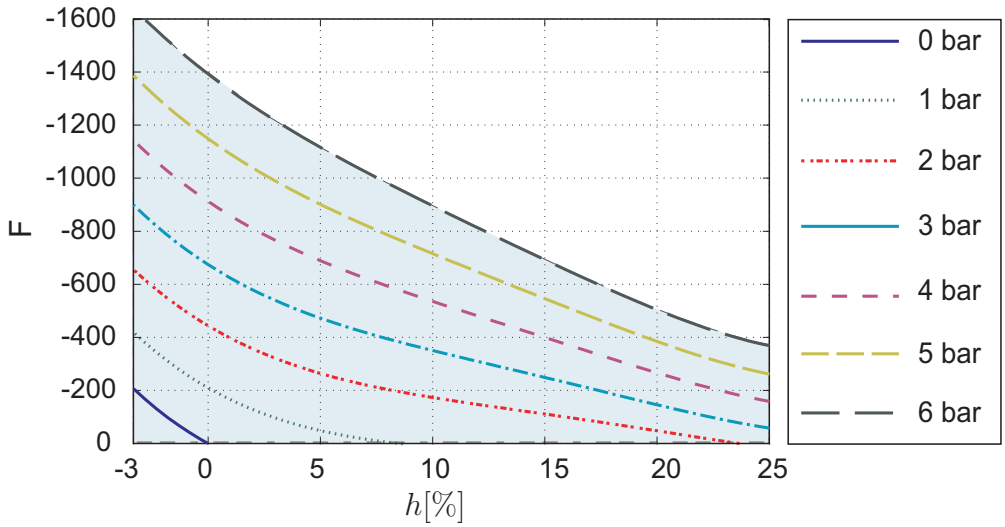

Figure 3.18: Muscle characteristics

the maximum contraction point is only 25 % of the initial length. This is a disadvantage in terms of the maximum stroke of the actuator, because 75 % of the actuator length cannot be used for contraction, which results in workspace restrictions to fluidic muscle applications. Moving along a constant-pressure line in direction of increasing contraction in Figure 3.18 leads to the decrease of the muscle force. If the pressure is changed iteratively, the force can be increased or decreased such that different force-displacement relationships can be realized within the working space of the fluidic muscle. This is an important characteristic for creating a manipulator which produces arbitrary force-displacement relationships.

The chosen fluidic muscles are of type MAS-20 and have a diameter of $20\ \mathrm{mm}$ and a tube length of $250\ \mathrm{mm}$. Each muscle is additionally connected with a prestressed coil spring featuring a stiffness c_{spring} in order to create also pushing forces. Using a design approach described in the next section,

we found the best compromise to choose as stroke of the combined actuator $\Delta\rho = 40$ mm. Since

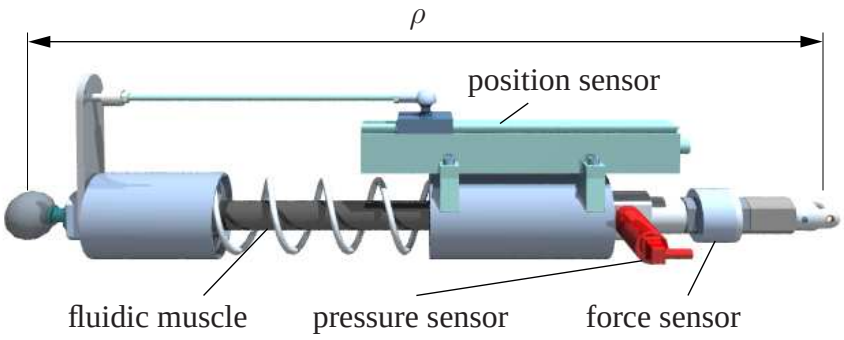

Figure 3.19: Actuator concept

both ends of the muscle rubber tubing are connected with flanges which are provided with internal threads, the full length of the delivered fluidic muscles is 385 mm. Using this maximal stroke and the given MAS 20 parameters, the actuator is at neutral mode when contracted to 50 % such that the chosen spring stiffnes is $c_{\text{spring}} = 7$ N/mm.

For the further geometric discussions, the actual length ρ of the actuator will encompass also joints, sensors, etc. and denote the distance between the two mid points of the spherical and universal joint respectively.

The force-displacement properties of the modified actuator are described in Figure 3.20. The actuator forces depend on the current length of the actuator and the air pressure. The maximal forces of the fluidic muscle MAS 20 at different strokes are given by the manufacturer. The corresponding maximal and minimal forces of one actuator (fluidic muscle + coil spring) at the attachment points of the platform (”-” = pull, ”+” = push) can be approximated by the following equations:

$$Q_{spring} = -7 \frac{\text{N}}{\text{mm}} \rho + 4,768.5 \text{ N} \tag{3.4}$$

$$Q_{max.\,pulling} = -0.304 \frac{\text{N}}{\text{mm}^2} \rho^2 + 361.3 \frac{\text{N}}{\text{mm}} \rho - 107,095.7 \text{ N} \tag{3.5}$$

The maximal pressure force line results from the prestressed coil spring, and the maximal pulling force curve is derived from the muscle force at maximum air pressure. The operation range of the fluidic muscle lies in the area between the maximal and minimal force line. The maximal tensile force is reached at maximal actuator length (645.5 mm) with -1300 N and the maximal compression force of +400 N is achieved at the minimal actuator length of 625.5 mm.

3.4 Dimensional design of the parallel robot

As described in section 3.2.3, the Gough-Stewart platform can be divided into three types depending on the arrangement of the joints. For the Hexaspine platform the SSM type [64] of a $\underline{UP}S$

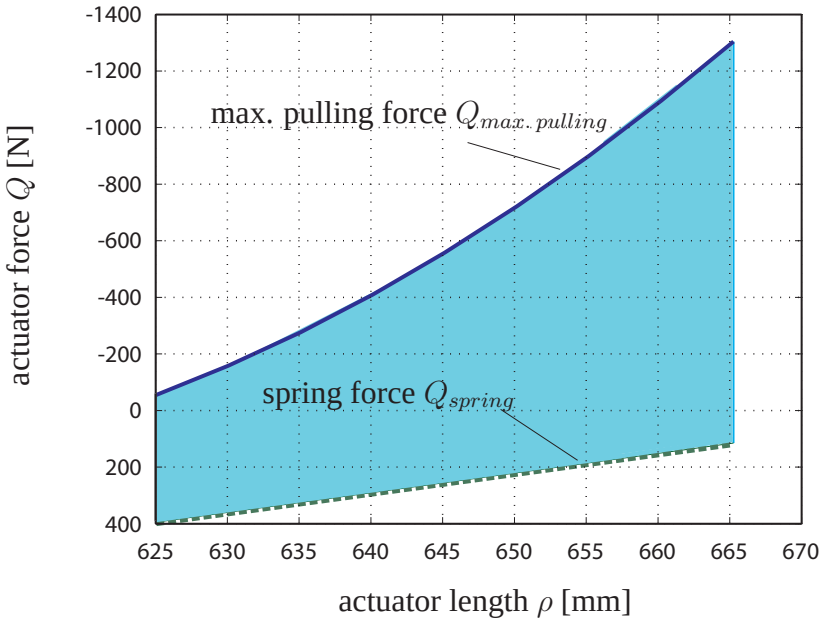

Figure 3.20: Maximal and minimal actuator forces as functions of actuator length

robot was chosen because this type of a $U\underline{P}S$ robot features a large workspace and allows a convenient placement of the attachment points. Moreover, the applied fluidic muscles would not have to be combined with additional mechanical components as needed in a $\underline{P}US$ configuration (section 3.2.2) or in a $\underline{R}US$ configuration (section 3.2.1).

In the selected configuration, the six attachment points of the spherical joint and universal joint centers lie on a circle and form a hexagon both on the mobile platform and the base (Figure 3.21). The coordinates of the attachment points are described by the offset angles α_A and α_B and the radii r_A and r_B.

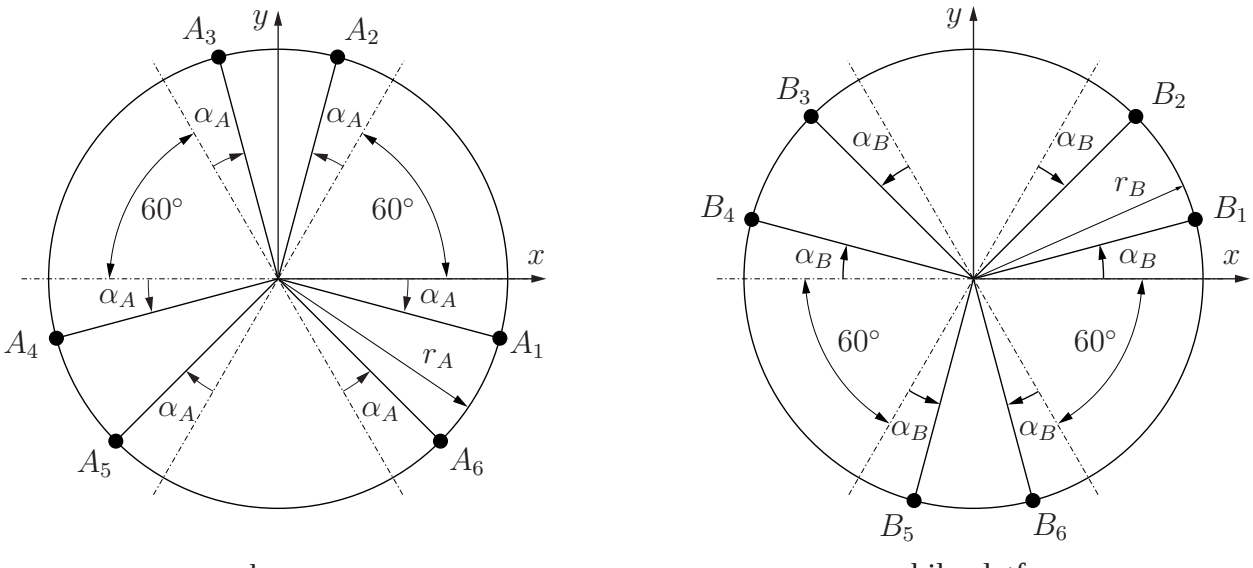

Figure 3.21: Attachment points of the joint center

The distance of the end effector from the plane passing through the spherical joint centers is denoted by h_{EE}, with positive values pointing up (see Figure 3.22). The platform velocities are

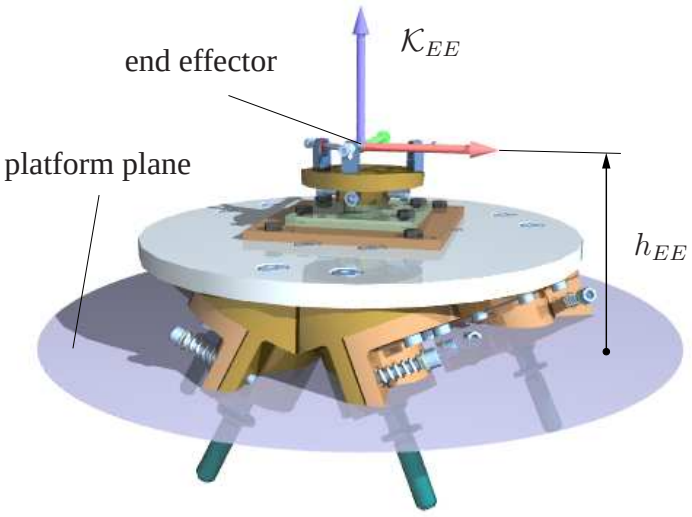

Figure 3.22: Distance of the end effector from the platform plane

defined as the twist

$$\underline{\mathrm{t}} = [\boldsymbol{\omega}^{\mathrm{T}}, \boldsymbol{v}^{\mathrm{T}}]^{\mathrm{T}}$$

including the vector of angular velocity $\boldsymbol{\omega}$ and the vector of linear velocity $\boldsymbol{v}$ of the platform. The inverse Jacobian of one general point of the parallel manipulator is defined $\mathbf{J}^{-1}$. In the following, we shall denote by $\delta\underline{\mathrm{t}}$ a small variation in pose, which can be interpretated as a small rotational variation $\delta\underline{\boldsymbol{\phi}}$ and a small translational variation $\delta\underline{\boldsymbol{r}}$ For the relationship between the pose variation $\delta\underline{\mathrm{t}}$ and the actuator length variations $\delta\underline{\boldsymbol{\rho}} = [\delta\rho_1, ..., \delta\rho_6]^{\mathrm{T}}$ it holds

$$\delta\underline{\boldsymbol{\rho}} = \mathbf{J}^{-1} \cdot \delta\underline{\mathrm{t}}\,. \tag{3.6}$$

The manipulability index of the mobile platform according to Yoshikawa [102] is defined as the determinant of the inverse Jacobian; the closer it is to zero the worse is the manipulability of a parallel platform. For the design of parallel manipulators, it must be regarded that singularity configurations are a serious problem for the manipulability of these mechanisms. Hence, singularities must be avoided by choosing the right geometrical parameters.

As described by Gosselin and Mayer St-Onge [86], architectural singularities occur when the inverse Jacobian $\mathbf{J}^{-1}$ of the platform is singular throughout the whole workspace. That means that one can obtain a parallel platform which can continuously move although the actuators are locked. According to Gosselin and Mayer St-Onge, and according to Ma and Angeles [62], the inverse Jacobian of a Gough-Stewart platform (UPS) is singular in each pose when the base and the platform are similar hexagons.

The specific requirements for the design of the Hexaspine platform arranged with $U\underline{P}S$ chains are as follows [60]:

(1) the manipulator should be as compact as possible

(2) in order to avoid singularity configurations, the determinant of the inverse Jacobian of the end-effector should be far from zero, which also corresponds to a large manipulability index of the mobile platform according to [102],

(3) due to constructive constraints (necessity of space for placement of sensors and housings, collision avoidance), the actuator lengths should not be shorter than $625.5\ \mathrm{mm}$

(4) the radius r_A and r_B should be greater than $75\ \mathrm{mm}$ in order to have enough space for actuators and joints,

(5) the relative swaying angle between the legs and the upper platform should not exceed $25°$ (Figure 3.23).

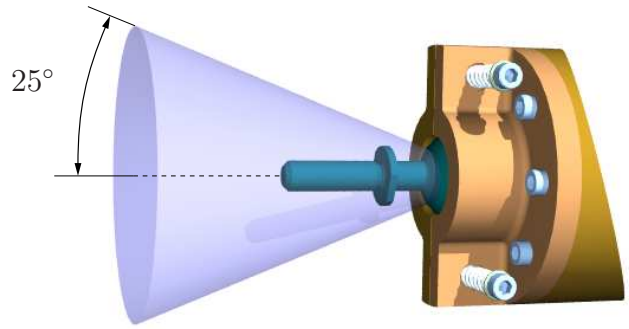

Figure 3.23: Limit of the spherical joint

In order to have a compact manipulator, the minimal actuator length will be set to the smallest possible length of $\rho_{min} = 625.5\ \mathrm{mm}$ such that the maximal length is $\rho_{min} = 665.5\ \mathrm{mm}$ due the maximal stroke of $\Delta\rho = 40\ \mathrm{mm}$. Thus, there are still five design parameters to be determined, as r_A, r_B, α_A, α_B and h_{EE}, denoted in Figures 3.22 and 3.23.

For the computation of the design parameters, the necessary ranges of motion described in Table 3.1 were applied as target values. First, the necessary actuator stroke as a function of the offset angles α_A and α_B was computed [60]. The result is given in Figure 3.24. One can see that the lowest strokes are attained for $\alpha_A = \alpha_B$. In particular, for α_A and α_B equal zero the minimal necessary stroke is obtained.

However, as shown in the diagrams of Figure 3.25, for the platform radii $r_B = 75\ \mathrm{mm}$ and $r_B = 150\ \mathrm{mm}$, the manipulability functions at $\alpha_A = \alpha_B$ always have a minimum equal to zero, meaning that a configuration $\alpha_A = \alpha_B$ is singular. Hence, the offset angles of the upper and lower joint centers, α_A and α_B, must be different. Further, it can be recognized in Figure 3.25 that for an increased radius of the upper platform the manipulability is also increased. Hence, for avoiding a singular configuration, the angles of the joint centers are set to $\alpha_A = -20\ °$ and $\alpha_B = 5\ °$. The

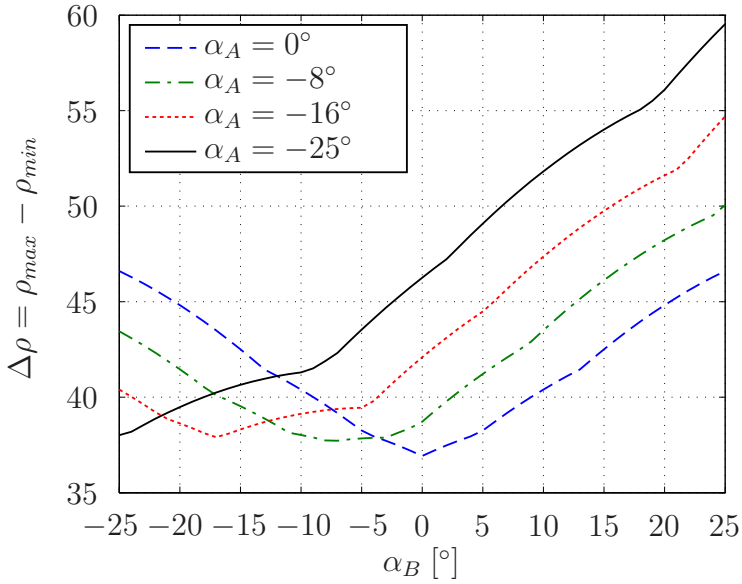

Figure 3.24: Stroke as function of α_A and α_B

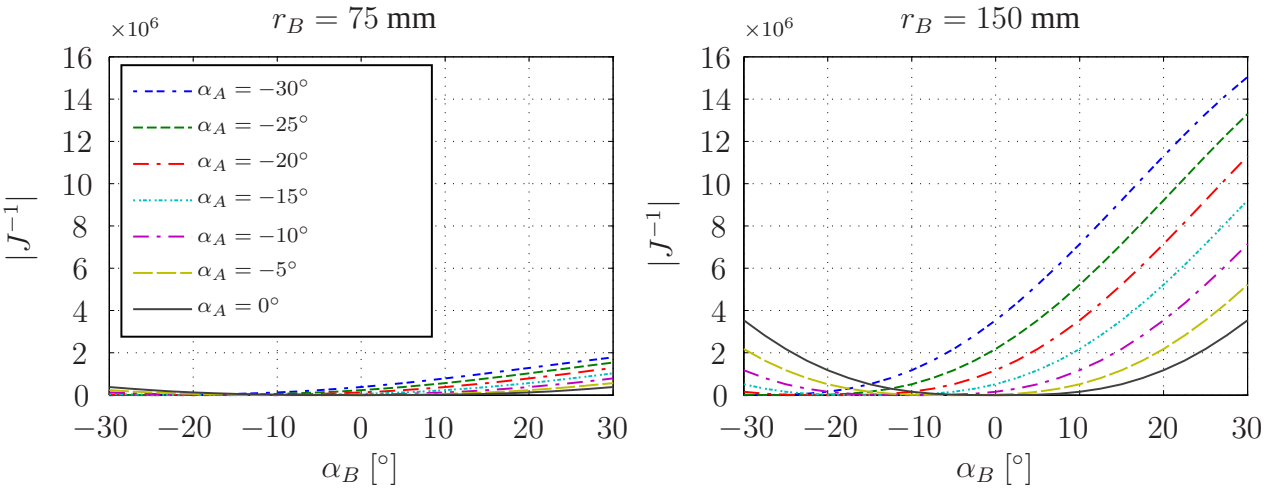

Figure 3.25: Manipulability as function of α_A and α_B

angle $\alpha_B = 5\,°$ of the upper platform could not be increased because of the required space for the socket housings of the spherical joints. Further, the radius of the circle on the base was set to $r_A = 400$ mm in order to have enough space between the actuators for avoiding collision.

Then, for the respective offset angles of $\alpha_A = -20\,°$ and $\alpha_A = 5\,°$ and the radius $r_A = 400$ mm of the base platform, the dependency of the necessary leg stroke on the end-effector offset is regarded in diagram 3.26, where the stroke is plotted over the upper platform radius for different values of the platform offset. As it can be seen, an operation point below the platform always requires higher stroke, while positive offset values reduce the necessary actuator strokes.

An operation point above the platform is also advantageous for the accessibility of the end effector, e.g., at fixation of specimen. Thus, the end effector offset was chosen as $h_{EE} = 125$ mm such that one obtains a necessary actuator stroke of 40 mm at a platform radius of $r_B = 100$ mm. The

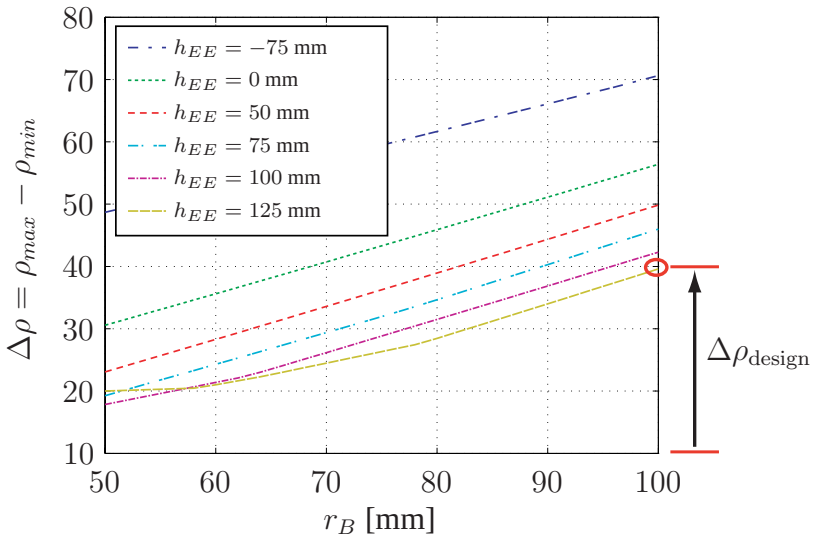

Figure 3.26: Stroke as function of h_{EE} and r_B ($\alpha_A = -20°, \alpha_B = 5°$)

Description	Value
Angle (base) α_A	20 °
Radius (base) r_A	400 mm
Angle (platform) α_B	10 °
Radius (platform) r_B	100 mm
Min. actuator length ρ_{min}	625.5 mm
Max. actuator length ρ_{max}	665.5 mm
Limit of spherical joint	25 °
TCP distance h_{EE}	125 mm

Table 3.5: Geometry Data

manipulability with this radius rendered a value of $5.9e5$ [60]. The finally selected data of the platform geometry is given in Table 3.5.

The final concept of the Hexaspine platform is shown in Figure 3.27. Since the TCP point (tool center point) of the hexapod is above the platform, a solid rack is placed next to the mechanism, which holds the rigid counterpart above the mobile platform. Between rack and mobile platform a jig is placed around the TCP point, where the cervical spine specimen can be fixated in order to get imposed with the forces and torques produced by the mobile platform.

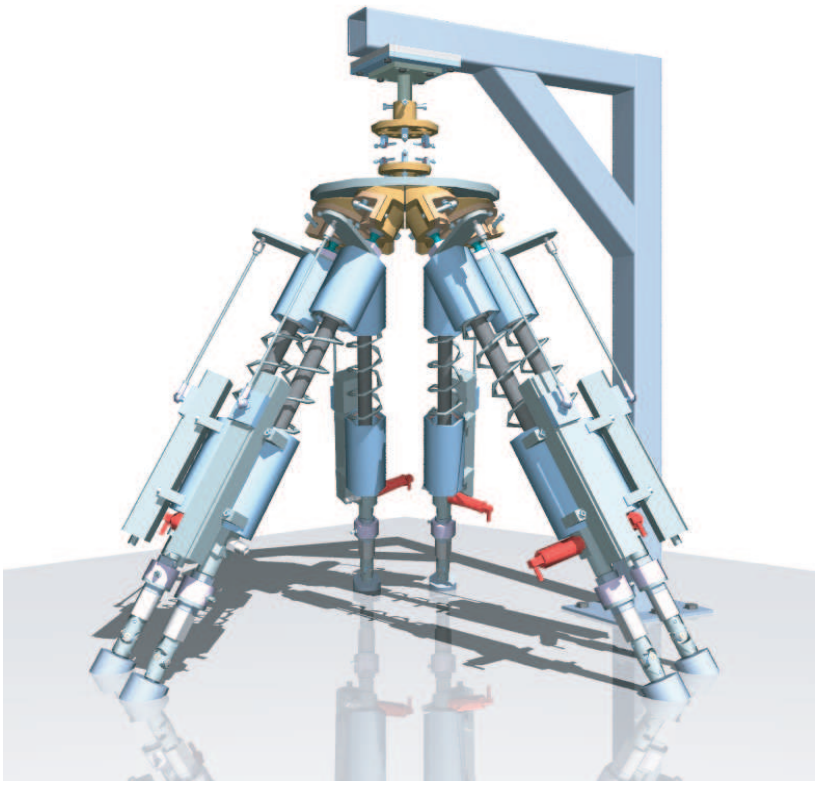

Figure 3.27: Virtual concept of Hexaspine platform

3.5 Workspace analysis

The workspace of a 6-DOF parallel robot can be represented with several methods, e.g., the *translation workspace*, the *orientation workspace* and the *dexterous workspace*. With the *translation workspace*, locations are considered which can be attained with translational motion of the platform in one given orientation of the end effector, therefore, it is also known as *constant orientation workspace* [65]. The *orientation workspace* is achieved when the platform is fixed in one location and can rotate about each axis. Further, the *dexterous workspace* includes all locations of the end effector in a translational workspace in which the maximum rotation about all three axes can be achieved. The *maximal workspace* (also called *reachable workspace*) defines the largest workspace, as it comprises all locations in a translation workspace to be reached with at least one orientation.

In terms of the calculation of the platform's workspace, a common method is the discretization of the pose parameters. With the discretization method, the workspace is covered by a regularly arranged grid in either cartesian or polar form of nodes. Each node is then examined such that for the given pose of the end effector the strokes of the actuators and the angles of the joints are calculated. By regarding the limits of the actuator strokes and the joint angles, it will be verified whether the respective node still belongs to the workspace or not. The accuracy of the boundary depends on the amount of nodes that is used to create the grid. The computation time grows with

the amount of nodes and creates a limit on the accuracy, such that exact boundary information cannot be acquired.

The target workspace of the Hexaspine platform results from the motion ranges of the vertebrae pair C5 and C6. The relative motion between the vertebrae shall be emulated physically with the Hexaspine platform. The values in Table 3.1 show that the required workspace is relatively small. To check if the target workspace is reached, the extreme situations for the actuators are investigated for fixed translation and for fixed orientation of the end-effector [60].

The translation in x, y and z direction can be represented as a box. It was verified for all six legs that the vertices of that box can be reached with the minimal and maximal leg lengths of the actuators with $\rho_{min} = 625.5\ \mathrm{mm}$ and $\rho_{max} = 665.5\ \mathrm{mm}$. Further, it was proven that the necessary angles given in table 3.1 were achieved in each of the vertices of the target translation workspace box. By using the extrema of the leg lengths, it was also validated in the C++ library ALIAS [66] that the desired workspace lies within the reachable workspace. Hence, it was proven [60] that the manipulator is geometrically consistent.

The reachable translation workspace is shown in diagram 3.28 .

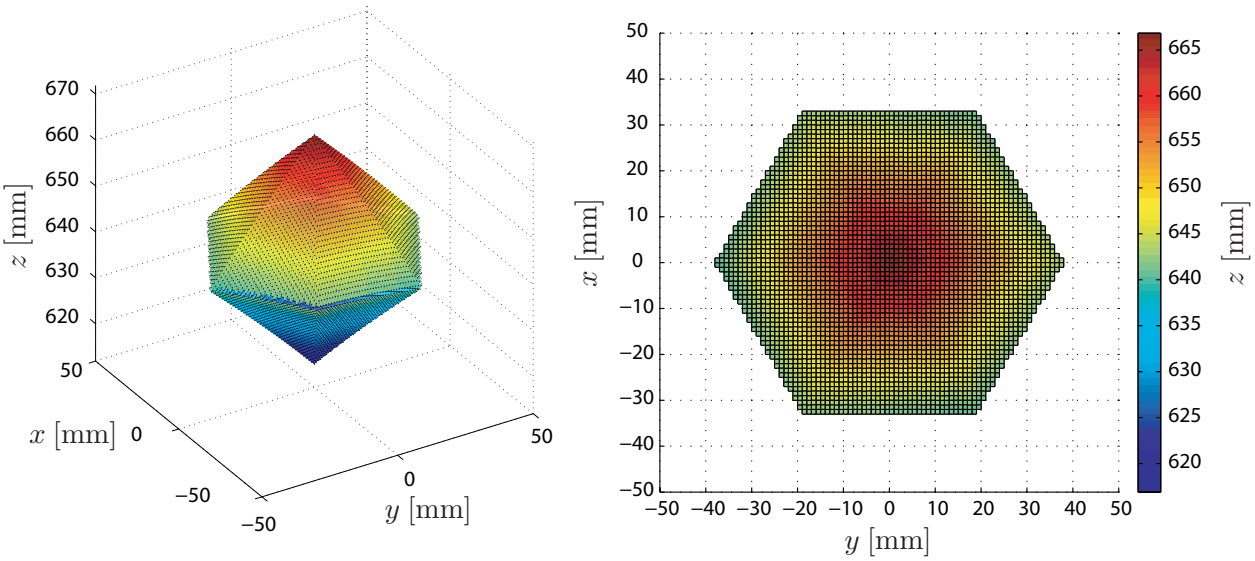

Figure 3.28: Translation workspace of the Hexaspine platform

The 3-dimensional view is given on the left hand side and the top view is given on the right hand side. The reachable translation workspace was determined by discretization method and is computed with the end effector orientation angles α_{EE}, β_{EE} and γ_{EE} equal to zero. The step size for the discretization is $1\ \mathrm{mm}$. The shape of the translation workspace consists of a polyhedron comprising 8 vertices and 12 triangular surfaces. The cross-section is of hexagonal type. For the illustration of the translation workspace the limits of the actuator strokes and the passive joints were regarded. The target translation workspace defined in Table 3.1 lies inside the reachable translation workspace depicted in Figure 3.28.

Description	Min. Value	Max. Value
F_x	-622.8 N	592.6 N
F_y	-709.4 N	709.5 N
F_z	-1117 N	2734.7 N
M_x	-51.5 Nm	52.3 Nm
M_y	-57.9 Nm	57.9 Nm
M_z	-61.6 Nm	61.6 Nm

Table 3.6: Results of the achievable end-effector forces/torques ([N] / [Nm])

In order to verify whether the necessary platform forces of Table 3.1 can be reached at each point of the target workspace, a solution using conventional kinetostatics would have been too complex [60]. Thus, the interval analysis C++ library ALIAS was applied in order to search for boxes that render forces within an interval that contains the required values [60].

To this end, the minimal and maximal end-effector forces/torques which the manipulator can exert at any pose in the desired workspace were computed by using the minimal and maximal forces (section 3.3) of the applied actuators. In case the achievable forces/torques enclose the desired ones (Table 3.1), the manipulator can be regarded as statically consistent. The corresponding results for the given values with an error of at most 100 are shown in Table 3.6. This means, e.g., that at each pose the manipulator will be able to exert a maximal force of $F_y = 709.5$, but there may be some poses for which the maximal force could be larger, up to $F_y = 809.5$. Hence, considering the values of Table 3.6, the designed manipulator is also statically consistent as the target force ranges of Table 3.1 are achieved.

3.6 Description of prototype

The complete actuator with the combination of the fluidic muscle and the coil spring is depicted in Figure 3.29. At the left end, a pressure port is available which leads to the muscle and can be interconnected with the pressure hose coming from the valve. And at the right end, a socket is mounted for holding the slide of the position encoder. The spring with a stiffness of $7\ \mathrm{N/mm}$ can be prestressed by rotating the cylinder on the right hand side which is provided with a fine thread for accurate adjustment of the spring force. The operation point of the actuator is reached with the spring length of 150 mm ($F_s = -251$ N) and at a contraction of 20 mm of the fluidic muscle inflated with 2.5 bar ($F_m = +251$ N) leading to mechanical equilibrium in that position.

Therefore the spring is prestressed on the length of 170 mm before the actuator is connected to the platform, then when the hexapod is assembled the actuators are contracted for 20 mm in order to reach the operation point. From that position the actuators can be operated with a stroke of

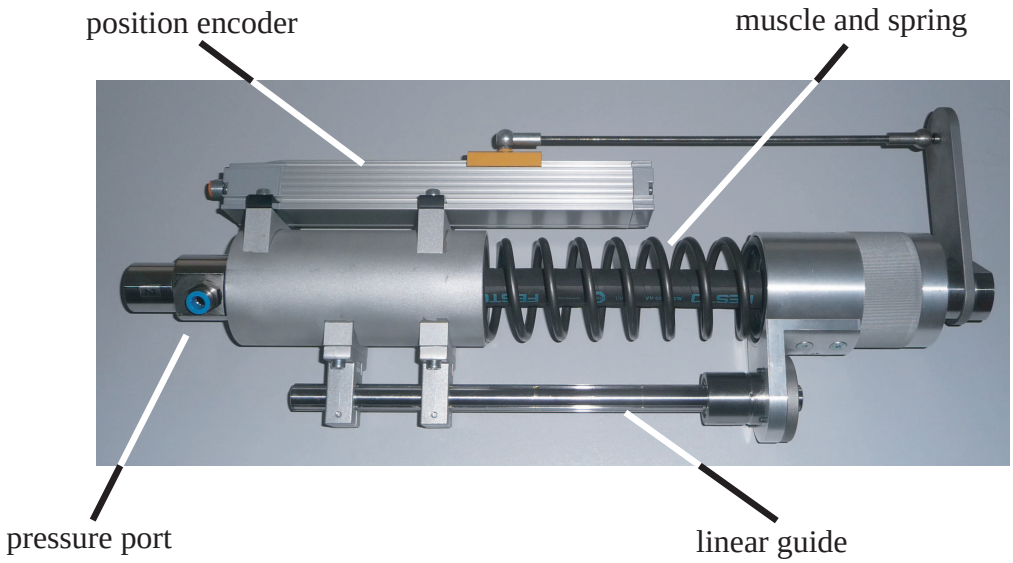

Figure 3.29: Single actuator

$\pm 20\ \mathrm{mm}$. The mechanical adjustment of the spring must take place before the actuator is fixed to the linear guide (Figure 3.29), since it is also connected to the cylinder which varies the prestress of the spring. Both support cylinders are made of aluminum. The linear guide was mounted additionally to the actuator for supporting possible transversal forces on the actuator. They are ball spline guides THK, type number LF16-300L, and consist of a nut which is guided on a cylindrical shaft, the nut having four trains of load-bearing balls. A retainer which is built into the interior of the nut causes the balls to circulate in line. The nut provided with a flange is fixed to a support which is connected to the cylinder. The guide is assumed as frictionless. The shaft is held by two bearing bocks which are mounted to the cylinder on the left hand side. The feedback is provided with sensors measuring force, pressure and position.

While selecting the sensors it had to be regarded that the control unit had only analog voltage inputs with a range of 0 to $10\ \mathrm{VDC}$, therefore only sensors with analog outputs were used. In case of force sensors this was not a restriction, since most of them are analog due to the application of strain gauges. The selected force sensor (Novatech, type number F256UFROKN) is depicted in Figure 3.30. The maximum force is 1.25 kN in compression as well as tension and the accuracy is 0.625 N. The output is $\pm 2\ \mathrm{mV/V}$, for achieving an output of 0 to $10\ \mathrm{VDC}$ the load cell must be connected with a strain gauge amplifier. For this an amplifier of HBM (TG 005) was applied featuring six analog outputs (ME 30) for amplifying the output signals of the six load cells to the range of 0 to $10\ \mathrm{VDC}$.

In contrast, the selected pressure sensor from SENSIT (HPSA-B10DVAB-10-G) depicted in Figure 3.31 has an output of 0 to $10\ \mathrm{VDC}$ for the overpressure of 0 to 10 bar. The accuracy of that pressure sensor is 0.015 bar. For the position feedback a magnetostrictive position encoder from Novotechnik (TLM 0100 001 411 102) was chosen, with a needed supplying voltage of $24\ \mathrm{VDC} \pm 20\ \%$. The signal output is 0 to 10 VDC, the range is $100\ \mathrm{mm}$ and the accuracy is

Figure 3.30: Force sensor (Novatech)

Figure 3.31: Pressure sensor (Sensit)

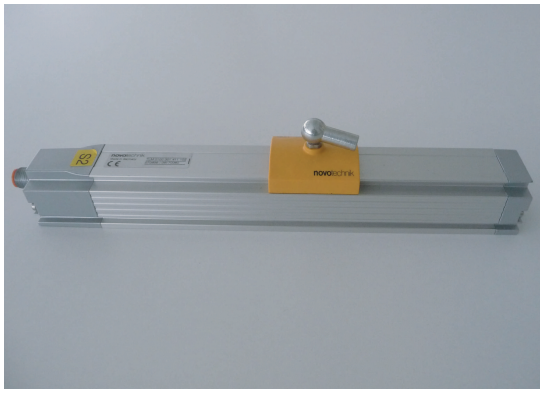

Figure 3.32: Position encoder

Figure 3.33: Valve and muscle (Festo)

0.02 mm. The yellow position marker is guided on the sensor cage and contains a permanent magnet.

The selected fluidic muscle and valve are depicted in Figure 3.33, the fluidic muscle of type MAS-20-250N-AA-MC-O has one pressure input and the tubing consists of textile fibers combined with chloroprene and aramide [27]. The tubing has a length of 250 mm and a inner diameter of 20 mm. The properties of the selected fluidic muscle are already described in section 3.3. The selected valve is a 5/3-way proportional directional control valve of type MYPE-5-1/8LF-010-B which controls the mass flow. The advantage of these valves is that they can reach higher dynamics than other valves, because no retarding valve-internal pressure control loop is used as for example in pressure control valves.

Since each fluidic muscle of the Hexaspine platform is to be controlled individually, each actuator is connected to its own valve. Below 5 V the valve is closed and from 5 V to 10 V the mass flow is increased. The prototype of the Hexaspine parallel manipulator is depicted in Figure 3.34, the base plate of the hexapod was fixed on a massive foundation bench. This basement serves as a damping

element for heavy vibrations, moreover the bench is featured with slots and is raised for about 1 m above the ground floor, making the fixation and the handling of the hexapod much easier.

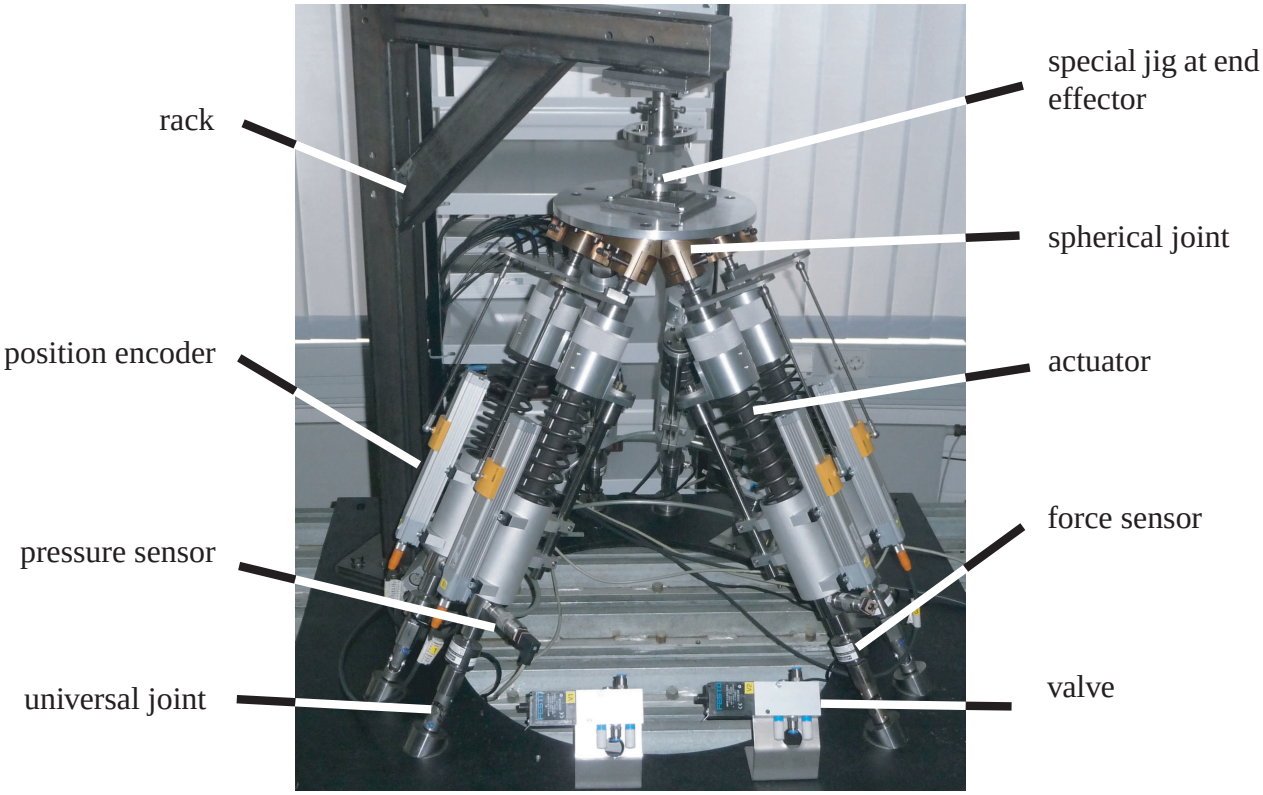

Figure 3.34: Prototype of the Hexaspine parallel manipulator

The rack was fixated next to the hexapod, which is the counterpart of the mobile platform when a force control is performed at the end effector. For test runs with vertebrae surrogates and implants, they can be fixated in a special jig (Figure 3.34). The upper part of that jig is connected to the rack and the lower part is fixed to the mobile platform. The sockets of the spherical joints demanded a more complex processing. They consist of two halfs (Figure 3.35), which were processed individually before they were assembled together. The halfs were manufactured partly by milling and partly by turning.

They were fastened together with screws attached with coil springs in order to adjust the gap between the socket halfs and the corresponding ball. The balls with a diameter of $40\ \mathrm{mm}$ were ordered from an external company and were made of chromium steel. In order to fasten the ball with the top of the actuator it was attached with an additional bolt provided with a male thread. The socket material consists of bronze (CW459K) for achieving low friction between the surfaces of the socket and the ball (chromium steel). Generally, it was intended that the moving masses of the Hexapod consisted of light alloy materials. Also the cylindrical elements of the actuator as described above were made of aluminum.

Since the developed parallel manipulator is a prototype which is improved continuously, it was regarded that the design is still open for smaller changes or replacements of components. For

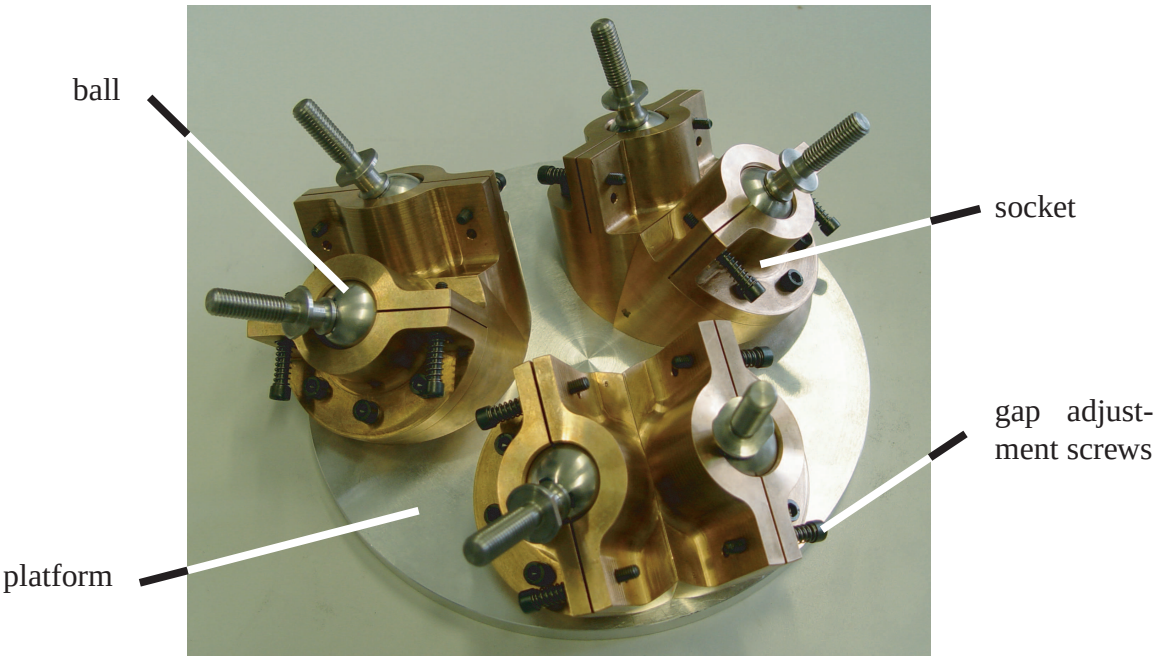

Figure 3.35: Spherical joints fixed to the platform

example, the jig which is placed at the end effector can be remounted easily and replaced with a shaft which can be connected rigidly with rack and mobile platform for a 6-DOF force control. Moreover, the actuators could be modified with the addition of supplementary linear guides, since enough space was still available for attachment points.

4 Modeling and Control of the Actuator

This chapter is devoted to the development of a model-based force control for a single actuator. After a detailed introduction of the governing equations describing the gas-dynamic behavior of the fluidic muscle, an approach is presented which simplifies the pressure rate ODE of the actuator by using exponential functions. Furthermore, in section 4.3, the corresponding identification procedure applied on the actuators is described regarding three different aspects of the fluidic muscle: the gas-dynamic behavior, the pressure-force-stroke and volume-stroke relationship. As a consequence, a mathematical model of the actuator is presented which can be adjusted to the behavior of each applied actuator by inserting the individually identified parameters into the model. The model-based force control which implies the inverse of the actuator model in combination with a PID controller is described in section 4.4. The chapter closes with a description of the uniaxial test stand which was used for the experiments and the presentation of the experimental results.

4.1 Gas-dynamic equations

For developing a model-based control of the fluidic muscle it is crucial that the gas-dynamic behavior of the pneumatic actuator is analyzed. Therefore, the ideal gas law

$$p \cdot V = m \cdot R \cdot T \tag{4.1}$$

and the polytropic equation

$$p \cdot \rho_m^{-\gamma} = const. \tag{4.2}$$

are considered, in which p, V, m, R, T, γ, ρ_m denote the relative pressure inside the muscle, the gas volume in the muscle, the gas mass, the gas constant, the temperature, the polytropic exponent, and the air density.

The polytropic exponent is taken from literature [40] as $\gamma = 1.26$, in which the behavior of the air in the fluidic muscle was identified between adiabatic and isothermal. By solving the equation 4.2 for p one gets the following expression

$$p = const. \cdot \rho_m^{\gamma} \tag{4.3}$$

which then is time-differentiated resulting in

$$\dot{p} = \gamma \cdot const. \cdot \rho_m^{\gamma} - 1 \cdot \dot{\rho}_m \, . \tag{4.4}$$

Inserting (4.2) into (4.4) gives:

$$\dot{p} = \gamma \cdot \frac{p}{\rho_m} \cdot \dot{\rho}_m \, . \tag{4.5}$$

Additionally, the definition of density

$$\rho_m = \frac{m}{V} \tag{4.6}$$

is taken into account such that the following expression is obtained for its time derivative

$$\dot{\rho}_m = \frac{\dot{m} \cdot V - m \cdot \dot{V}}{V^2} \, . \tag{4.7}$$

After inserting 4.7 in 4.5 one gets:

$$\dot{p} = \gamma \cdot \frac{p}{m} \cdot \dot{m} - \gamma \cdot \frac{p}{V} \cdot \dot{V} \, . \tag{4.8}$$

And finally, the law of ideal gas (4.1) is inserted into (4.8), such that $\dot{p}$ is represented as follows:

$$\dot{p} = \gamma \cdot \frac{RT}{V} \cdot \dot{m} - \gamma \cdot \frac{p}{V} \cdot \dot{V} \, . \tag{4.9}$$

Here, the polytropic exponent and the gas constant are assumed to be almost constant, while the gas temperature T will vary according to the adiabatic process. However, it is assumed that this change is small such that the temperature-dependent parameters, as for instance rubber elasticity, are assumed to remain constant. Additionally, it is assumed that the volume of the muscle depends only on the stroke and can be approximated with a polynomial function $V = V(s)$ which is

described in section 4.3.2. Thus, if this polynomial function is differentiated, the variation of the muscle volume $\dot{V}$ is represented as a function which depends on stroke and velocity:

$$V = V(s) \Rightarrow \dot{V} = \frac{\mathrm{d}V(s)}{\mathrm{d}s} \cdot \dot{s} \,. \tag{4.10}$$

The mass flow $\dot{m}$ with which the muscle is inflated has a nonlinear characteristic and is a function of the relative pressure p inside the muscle and the input voltage u of the valve

$$\dot{m} = \phi(p, u) \,. \tag{4.11}$$

where the supply pressure is assumed to be constant and the function $\phi(p, u)$ is still unknown. By inserting the equations 4.11 and 4.10 into equation 4.9 the differential equation for $\dot{p}$ becomes:

$$\dot{p} = \underbrace{\gamma \frac{RT}{V(s)} \phi(p, u)}_{f_1(s,p,u)} - \underbrace{\gamma \frac{p}{V(s)} \frac{\mathrm{d}V(s)}{\mathrm{d}s}}_{f_2(s,p)} \dot{s} \tag{4.12}$$

such that $\dot{p}$ is represented by a superposition of two terms

$$\dot{p}(s, \dot{s}, p, u) = f_1(s, p, u) + f_2(s, p)\dot{s} \tag{4.13}$$

depending on the stroke s, the velocity $\dot{s}$, the valve voltage u and the pressure p. The second term in equation 4.13 can be readily computed once the approximation $V(s)$ is known (from measurements, section 4.3.2) and the pressure is given. The diffcult term in equation 4.13 is the first term.

4.2 Best-fit approximation of gas dynamics by simplified equations

For the approximation of the gas-dynamic behavior, the equation 4.13 is considered. If the position of the actuator is held constant, the velocity becomes zero, such that the second term of the right side of the equation vanishes. Thus, the remaining first term in equation 4.13 is just the pressure rate for fixed actuator length and given voltage and pressure values:

$$f_1(s, p, u) = \hat{\dot{p}}_s(p, u) = \dot{p}(s, p, u)\Big|_{s=\text{const.}} \,. \tag{4.14}$$

In order to determine this two-parametric function, the actuator is fixed into a rigid frame at different lengths and then voltage step functions of the amplitude u (Figure 4.1) are applied to the fuidic

muscle starting at $p = 0$. From the resulting transient pressure step responses and the ensuing time histories (Figure 4.2), the slopes at different times and thus also at different pressures can be determined numerically, yielding a field of slopes for each voltage step response. The slopes can

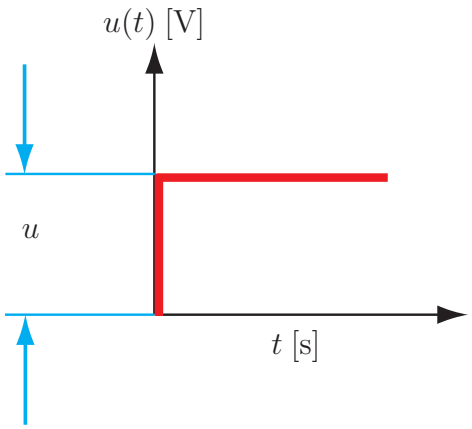

Figure 4.1: Voltage step

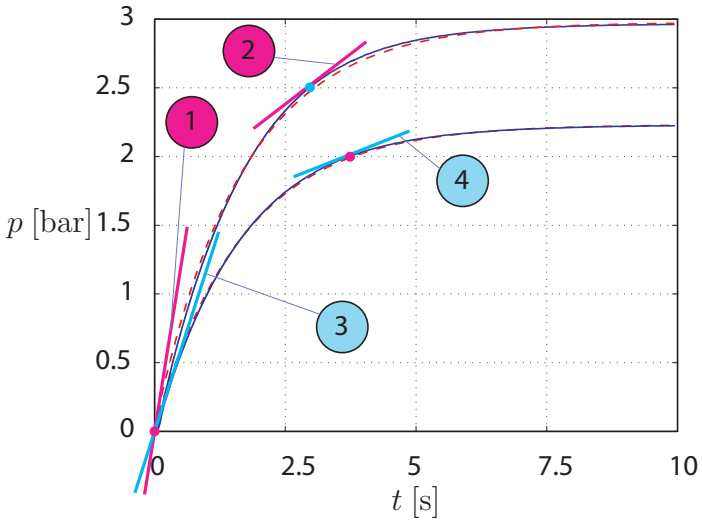

Figure 4.2: Response of actuator pressure to voltage step

be detected at different points, e.g., in point 1 and 2 of the upper pressure response (Figure 4.2). The determined slopes can be plotted over the muscle pressure and the valve voltage, yielding a set surface describing the pressure rate over pressure and valve voltage (Figures 4.3 and Figure 4.4); this surface is the sought function 4.14.

For example, the slopes of point 1 and 2 and other slopes which can be taken from the upper pressure response then yield the line in the right plane in Figure 4.3. For another voltage step function the pressure response in Figure 4.2 is obtained for which the slopes at point 3 and 4 are determined. It should be noted that the procedure must be repeated for pressure decreases resulting from a clo-

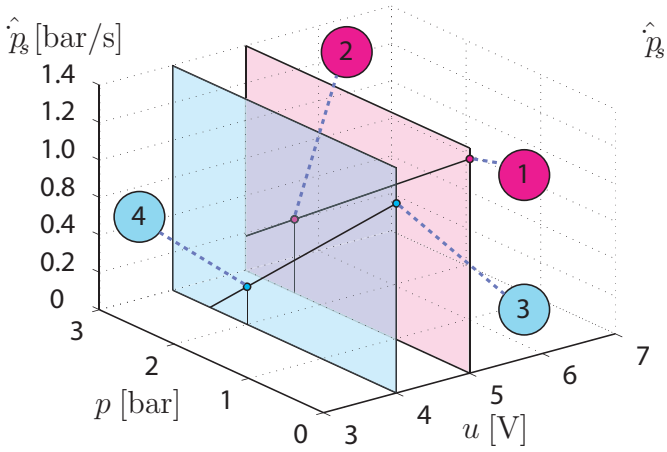

Figure 4.3: Generation of $\hat{\dot{p}}_s$ lines of corresponding voltages

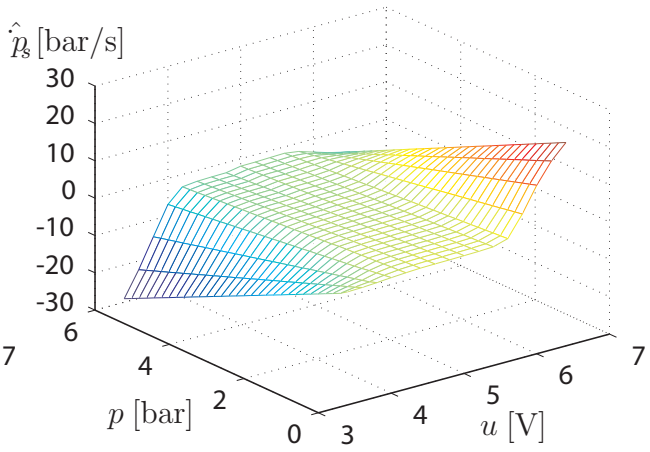

Figure 4.4: Surface of $\hat{\dot{p}}_s(p, u)$ for fixed s

sing valve, as the corresponding coefficients are different than those for pressure increase. Thus,

there will be an own surface function for negative and positive pressure rate values. This method of collecting the pressure rates resulting from the voltage step functions into a parametric surface can be improved by the following semi-analytic approach.

From the step response time histories in Figure 4.1, one can recognize that these resemble quite closely exponential functions. By parameterizing these exponential functions for fixed stroke s as

$$p_{\mathrm{inc}}^{\mathrm{appr}}(t;u)|_{u=\mathrm{const.}} = k_1(u)(1 - e^{-k_2(u)t}) + k_3(u) \tag{4.15}$$

one can determine the coefficients $k_1(u)$, $k_2(u)$ and $k_3(u)$ from least squares fitting of the parametrized exponential function with the measured step responses for constant actuator strokes s and constant valve voltage step functions u. The time derivative of the exponential approach then leads to following expression:

$$\hat{p}_{\mathrm{inc}}^{\mathrm{appr}}(u) = k_1(u)k_2(u)e^{-k_2(u)t} \; . \tag{4.16}$$

After resolving equation 4.15 for the exponential function and back-substituting this expression into equation 4.16, one obtains the approximation of the pressure rate (for fixed u and s) as

$$\hat{p}_{\mathrm{inc}}^{\mathrm{appr}}(u) = k_2(u)(k_1(u) + k_3(u) - p) = \tilde{f}_1(s,u,p) \tag{4.17}$$

which replaces the equation 4.14 at pressure increases. Equation 4.17 shows that the pressure rate is approximately a linear function of the pressure, i.e., that the dynamic behavior resembles a PT_1 element.

For pressure decreases, a corresponding exponential function

$$p_{\mathrm{dec}}^{\mathrm{appr}}(t;u)|_{u=\mathrm{const.}} = \ell_1(u)e^{-t\ell_2(u)} + \ell_3(u) \; . \tag{4.18}$$

is used as approximation, where the parameters $k_1(u)$, $k_2(u)$, $k_3(u)$ are again determined from corresponding measurements and least squares fitting. For the time derivative one then obtains:

$$\hat{p}_{\mathrm{dec}}^{\mathrm{appr}}(u) = -\ell_1(u)\ell_2(u)e^{-\ell_2(u)t} \tag{4.19}$$

which after re-substituting for the exponential function analogously to equation 4.17 leads to

$$\hat{p}_{\mathrm{dec}}^{\mathrm{appr}}(u) = \ell_2(u)(\ell_3(u) - p) = \tilde{f}_1(s,u,p) \tag{4.20}$$

which again is a linear expression in p and replaces equation 4.14 at pressure decreases. The approximated pressure rates $\hat{\dot{p}}_s = \tilde{f}_1(s,u,p)$ for fixed positions replace the first term $f_1(s,p,u)$ of the general pressure-rate ODE of equation 4.12 such that one obtains

$$\dot{p} = \tilde{f}_1(s,u,p) - \underbrace{\gamma \frac{p}{V(s)} \frac{\mathrm{d}V(s)}{\mathrm{d}s}}_{f_2(s,p,\dot{s})} \dot{s} \,. \tag{4.21}$$

for the computation of the pressure rate at variable position.

4.3 Identification of actuator characteristics

In the following, the identification procedures for analyzing the characteristics of the fluidic muscle are described. The identification is carried out by specific experiments of the fluidic muscle on a single axis testbed. The measurement data is obtained from different experiments for each of the six actuators individually.

4.3.1 Pressure-force-stroke relationship

The pressure-force-stroke relationship is obtained from measurements with the complete actuator. For equilibrium condition it holds

$$-Q - F_m + F_s = 0 \tag{4.22}$$

where F_m, F_s, and Q are the muscle force, the spring force, and total actuator force, respectively, with positive forces for pushing and negative forces for pulling.

Hence, the total force is

$$Q = F_s - F_m \tag{4.23}$$

The muscle force is described as the relative pressure times the volume flow as follows

$$F_m = -p \cdot \frac{\mathrm{d}V(s)}{\mathrm{d}s} \,, \tag{4.24}$$

	initial value	increment	final value
Position [mm]	20	-2	-20
Pressure [bar]	$0 + p_{\text{offs.}}$	0.2	4.8

Table 4.1: Operation mode for p,s,F - measurement

Further, for the air volume of the fluidic muscle it holds

$$\frac{\mathrm{d}V(s)}{\mathrm{d}s} < 0 \tag{4.25}$$

since for increasing s (see Figure 4.5) the air volume of the fluidic muscle decreases.

The spring force is

$$F_s = -c(s_p + s)\,. \tag{4.26}$$

with the spring stiffness c, the negative spring prestress stroke s_p for reaching the operation point of the combined actuator and the actuator stroke s in reference to the operation point. Thus, the resulting actuator force then can be described as a function which depends on stroke and pressure:

$$Q = F_s - F_m = -c(s_p + s) + p \cdot \frac{\mathrm{d}V(s)}{\mathrm{d}s} = g(s, p)\,. \tag{4.27}$$

The aim is to approximate this force function by a polynomial function

$$Q = \sum_{i,j=0}^{i+j\leq 9} a_{ij}\, s^i\, p^j\,. \tag{4.28}$$

To this end, experiments were carried out with constant stroke increments and different pressure values. The stroke ranged within $\pm 20\ \mathrm{mm}$ with 21 stroke increments of $2\ \mathrm{mm}$ as depicted in table 4.1 and figure 4.5. Because for each stroke the force had to be measured for different target pressure values, a step function was arranged with an increment of $\mathrm{d}p = 0.2\mathrm{bar}$ as described in table 4.1 and depicted in figure 4.6. The starting point is 0 bar and the end point is 4.8 bar. The pressure could not be prescribed directly because proportional servo valves are applied, which control the mass flow and not the pressure. Thus, a closed-loop control with pressure feedback was necessary. The automation for the measurement and the pressure control depicted in figure 4.7 was programmed in Matlab/Simulink and implemented on a dSPACE control system.

For the positions of $s = +20\ \mathrm{mm}$ to $s = 10\ \mathrm{mm}$ the pressure step function begins at 0 bar. Below $s = 10\ \mathrm{mm}$ the tubing of the fluidic muscle tended to buckle at very low pressures because the

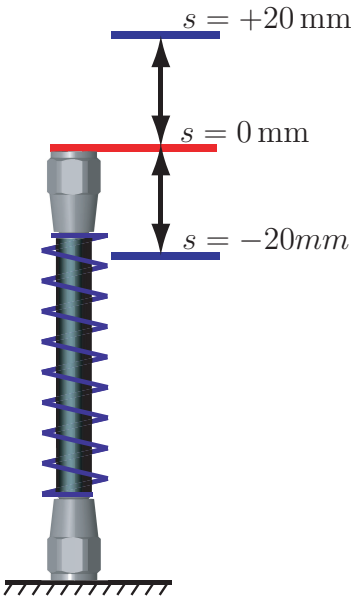

Figure 4.5: Actuator stroke

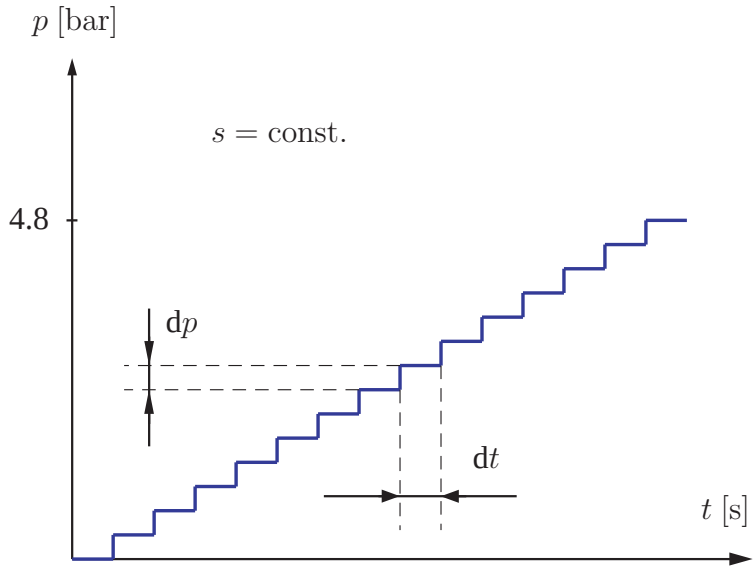

Figure 4.6: Pressure step function at constant strokes

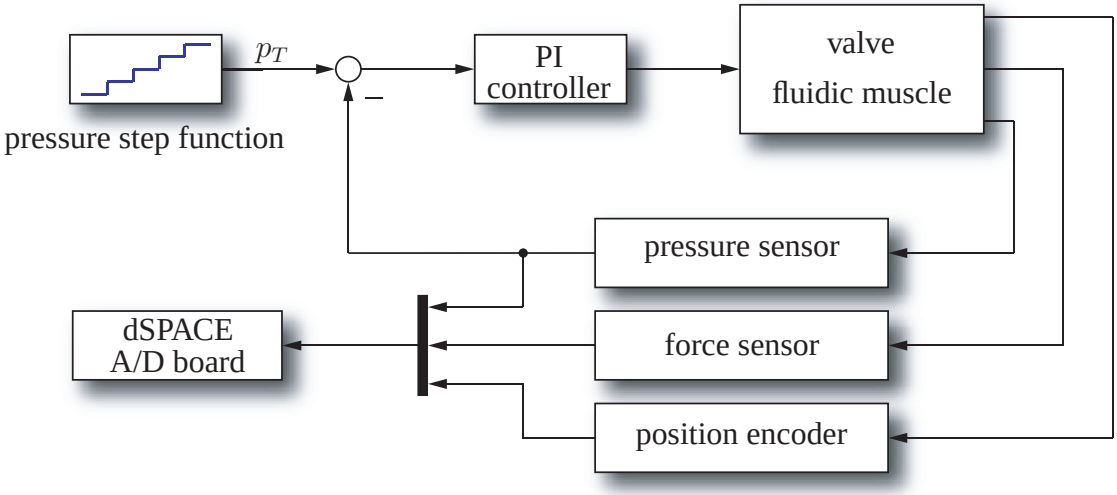

Figure 4.7: Block diagram of p, s, F-measurement

actuator was fixed in that position. A buckling of the muscle can damage the rubber material and should be avoided. Therefore, the muscle was inflated with a certain offset pressure $p_{\text{offs.}}$ (table 4.1) before starting the experiment with the pressure step function. The offset value in each position increment below $s = 10\ \text{mm}$ was the lowest possible pressure which did not lead to a folding of the muscle.

The target value p_T (see figure 4.7) in this case is the pressure step function, the difference between target pressure and measured pressure then is inserted into the PI controller which prescribes the respective valve voltage. The pressure and force signals were filtered and hereafter captured at a sample time of $1\ \text{ms}$. The pressure progress in comparison with the target pressure and the measured force at a constant position of $-8\ \text{mm}$ is depicted in figure 4.8.

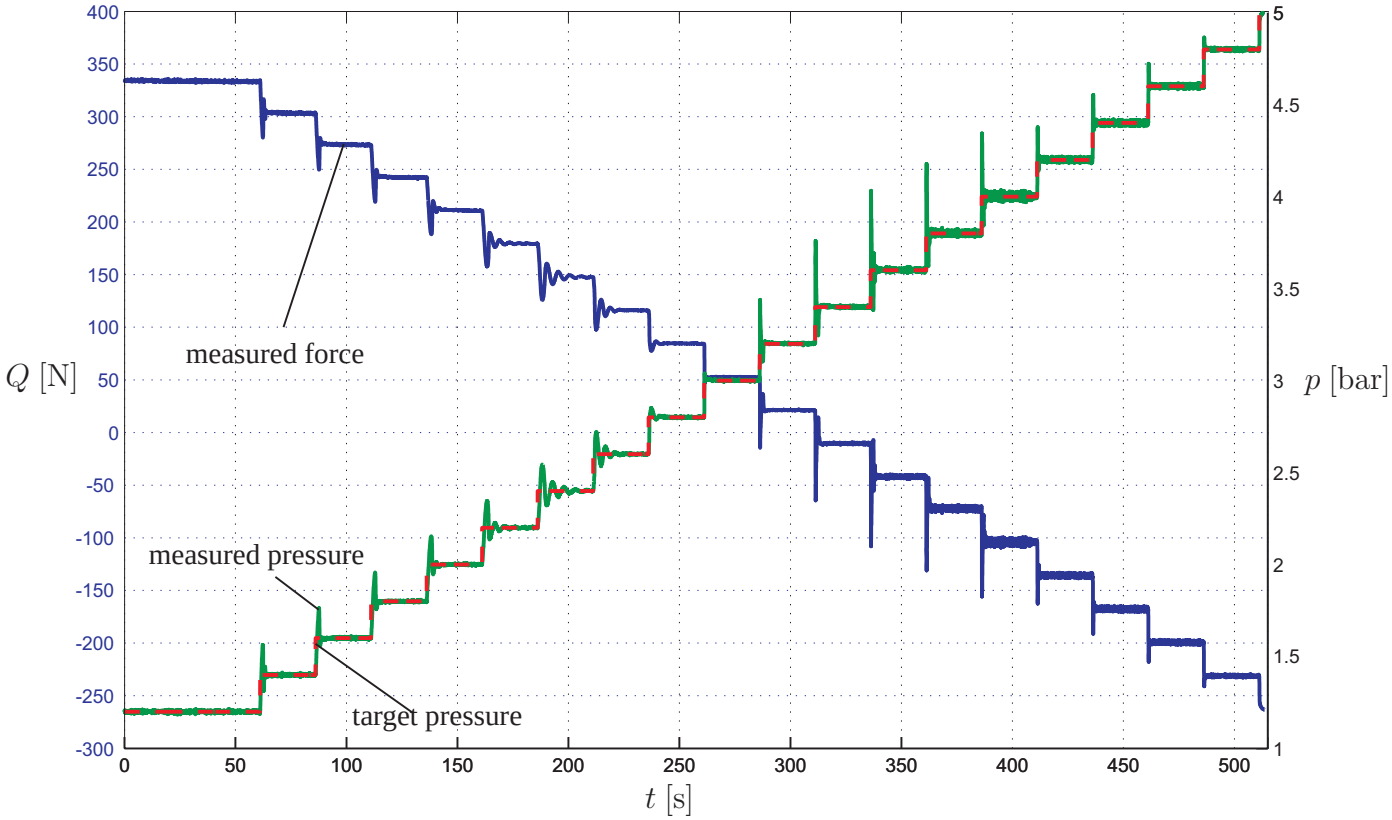

Figure 4.8: Pressure-step function at $s = -8\,\text{mm}$

It can be observed that the measured pressure overshoots at the pressure jumps before settling down to the target values. To this end, a large time increment of 25 s for the pressure step function was chosen such that the system is given enough time to stabilize for measuring the right pressure and force values. The direct relationship between the muscle pressure and the muscle force can be observed when the pressure starts oscillating at the beginning of the steps leading to an oscillating force in the same manner and settles down when the pressure reaches the target value.

The data pairs of force and pressure measured in oscillating situations were excluded. A routine was programmed in Matlab such that only force-pressure data pairs were used in which the difference between target pressure and measured difference was below 1 mbar. For each target pressure

Q [N]	p [bar]	Q [N]	p [bar]	Q [N]	p [bar]	Q [N]	p [bar]
333.7188	1.1995	179.5405	2.1995	21.2737	3.1995	-103.858	3.9995
303.3977	1.3995	147.7192	2.3996	-10.2187	3.3995	-135.715	4.1995
273.3185	1.5995	116.1447	2.5996	-41.655	3.5995	-167.4322	4.3995
242.3155	1.7995	84.5459	2.7995	-41.655	3.5995	-199.2254	4.5995
211.0603	1.9995	52.6693	2.9995	-71.8878	3.7995	-231.164	4.7995

Table 4.2: Pressure and force at $s = -8\,\mathrm{mm}$

the mean value of the measured force was determined. These values for a position of $-8\ \mathrm{mm}$ are given in table 4.2. It has to be mentioned that these values describe the quasi-static behavior of the fluidic muscle because the data was saved when the system has settled down in a stable steady-state. This set of values for pressure and force were measured and postprocessed for each of the 21 stroke steps such that the result can be displayed in the 3D-diagram in Figure 4.9, where the measured force is plotted over the prescribed pressure and stroke. Then, the least squares method

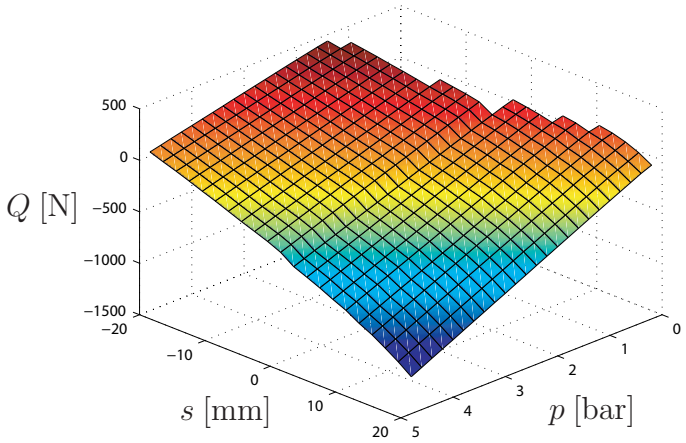

Figure 4.9: Measurement of p, s, F - behavior

was used in order to approximate the surface of the measured force over pressure and stroke with a polynomial function $G(p, s)$ with the coefficients a_{ij} of this function. The result of the approximation is given in Figure 4.10. The difference between the measurement and the approximation is depicted in Figure 4.11, where the maximum error is $10\,\mathrm{N}$ which is about 1 % of the maximum force. The region which could not be measured at large contraction and low pressure due to the buckling of the muscle is an area which is never reached when the muscles are applied on the hexapod. These are conditions which only occur when the platform is loaded with a very heavy weight, making necessary pressure forces of much more than $1000\,\mathrm{N}$ at the end effector which will not be the case in the application field of the Hexaspine platform. The inverse of this polynomial function will later be used in the model-based control of the actuator as described in section 4.4.

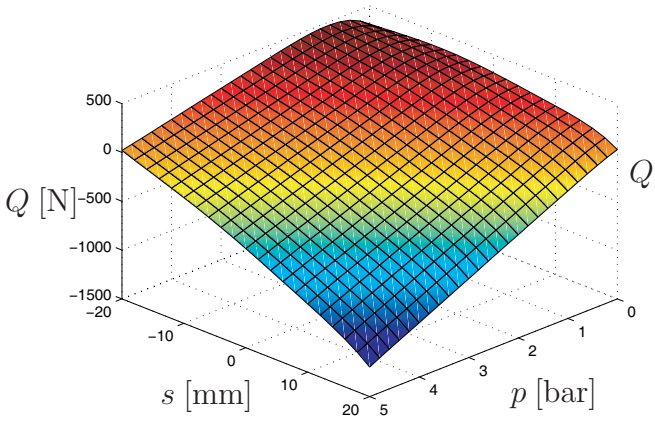

Figure 4.10: Approximation of p,s,F-behavior

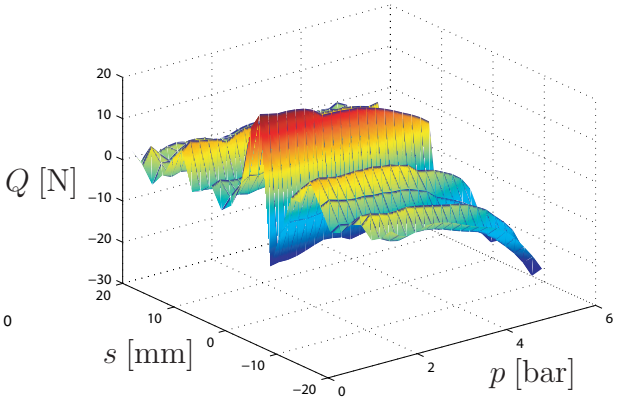

Figure 4.11: Approximation error

4.3.2 Volume-stroke behavior

Referring to the pressure ODE (4.9) from section 4.1, it is necessary to define the volume as well as the volume flow. Since the energy conservation law [85] states that the mechanical work of the fluidic muscle is equal to its gas work, it holds:

$$W_{mech} = W_{gas}.$$

Hence, the following equation can be written:

$$F_m \cdot \mathrm{d}s = p \cdot \mathrm{d}V = p \cdot \mathrm{d}V \ . \tag{4.29}$$

Since the pressure sensor measures the relative pressure p, the equation 4.29 can be simplified and solved for $\mathrm{d}V$:

$$\mathrm{d}V = \frac{F_m}{p} \cdot \mathrm{d}s \ . \tag{4.30}$$

For the determination of the variables in equation 4.30, the measurements of the pressure-force-stroke relationship from section 4.3.1 are used. The muscle force is determined from the difference of the total actuator force Q and the spring force F_s. It was observed that the relationship between pressure and force at a constant stroke is linear. The quotient F_m/p is determined for each measured stroke. To this end the quotients F_m/p resulting from the pressure step function depicted in Figure 4.8 were averaged for each stroke. The determined quotients of F_m/p were drawn over the stroke s as depicted in fig. 4.12. These points were approximated with a 7th order polynomial function. In order to obtain the volume function the approximation of F_m/p is integrated with respect to the stroke s by regarding the initial volume of the fluidic muscle. The obtained volume-stroke relationship $V(s)$ is depicted in fig. 4.13.

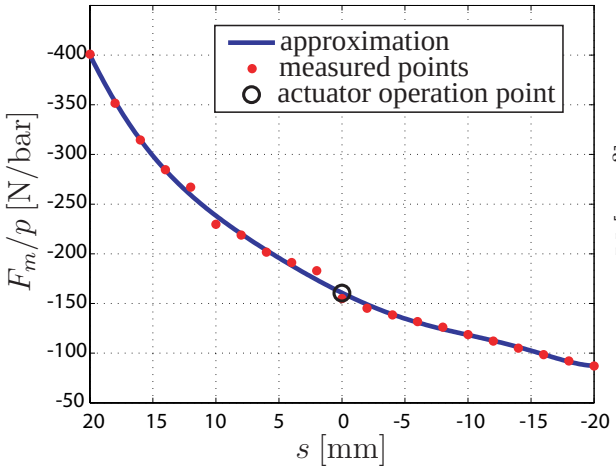

Figure 4.12: dV/ds - polynome

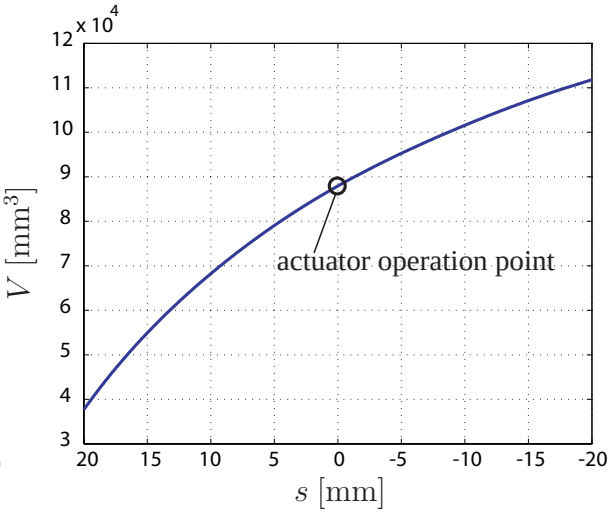

Figure 4.13: $V(s)$ - polynome

4.3.3 Determination of exponential fitting parameters

For the identification of the fluidic muscle characteristics, in addition to the pressure-force-stroke and volume-stroke relationships also the gas dynamic behavior of the valves was identified. The pressure responses were approximated by exponential fitting.

The exponential approach is

$$p_{\text{inc}}^{\text{appr}}(t;u)|_{u=\text{const.}} = k_1(u)(1 - e^{-k_2(u)t}) + k_3(u)\,, \tag{4.31}$$

Its parameters k_1, k_2 and k_3 are determined from measured data using least squares minimization

$$k_1, k_2, k_3 : \sum_{i=0}^{n} \|p_{\text{inc}}^{\text{appr}}(i\Delta t) - p_{\text{inc}}^{\text{meas}}(i\Delta t)\|^2 = \min. \tag{4.32}$$

The approximation routine was programmed in Matlab and performed using the sampling time of $\Delta t = 1$ ms [60]. The same procedure was repeated for the pressure decreases, which was approximated by the exponential approach

$$p_{\text{dec}}^{\text{appr}}(t;u)|_{u=\text{const.}} = \ell_1(u)e^{-t\ell_2(u)} + \ell_3(u)\,. \tag{4.33}$$

The measurements of the pressure responses were carried out according to the basic conditions given in table 4.3. The applied proportional valves start inflating the muscle at an input voltage of 3.4 V, below this voltage the valve is fully closed. The maximum chosen voltage at which the muscle is fully inflated is 6.4 V. The reference voltage from which the voltage step function starts is 2 V. First, the voltage jumps on the initial step voltage of 3.4 V at full expanded length of the muscle and resides in this voltage for $\Delta T = 20$ s. Then, the voltage resets to the basic reference of 2 V again for a period of $\Delta T = 20$ s. Then the voltage jumps to the next valve voltage which

		initial value	step size	end value
position	$[mm]$	20	-2	-20
valve voltage	$[V]$	$3.4 + U_{\text{offs.}}$	0.2	6.4

Table 4.3: Operation mode for measuring pressure responses

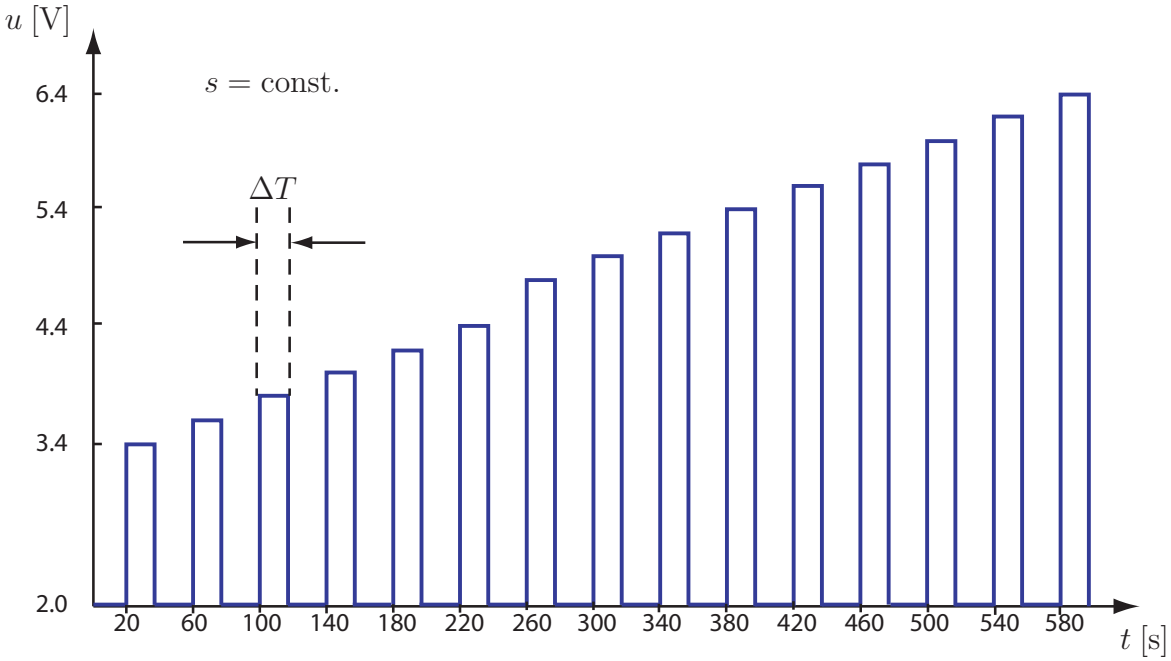

Figure 4.14: Voltage step function for inducing pressure increases at constant strokes

is now 0.2 V larger than the initial step voltage. Subsequently, the experiment is continued with steps increasing for 0.2 V until the maximum voltage of 6.4 V (see figure 4.14).

Since the muscle tends to buckle at low pressures and high contraction in fixed position the initial step voltage had to be increased with $U_{\text{offs.}}$ for low contractions. The initial voltage step ranges from 3.4 V to 4.2 V required, e.g., at the minimum stroke of $s = -20$ mm. For obtaining the pressure responses resulting from a closing valve, the ranges for the voltage steps were chosen again between 3.4 V and 6.4 V, but this time starting from the reference value 8 V(Figure 4.15). To verify if the parameters of the exponential functions depend also on the actuator stroke, the measurements were carried out for different stroke steps of 2 mm. The voltage step functions were programmed in Matlab/Simulink, and the identification was carried out using the identification software Control Desk of dSPACE (Figure 4.16).

A comparison between a set of measured pressure increases and their approximations is given in figure 4.17 for the voltage step functions beginning at 2 V and ending up in 4 V, 4.4 V and 5 V. The respective pressure rate for the opening valve is given in figure 4.18. A fair agreement between measured and approximated values can be seen except at the beginning of the time histories, where higher-order valve dynamics occur due to the sudden valve opening. Regarding the pressure decreases, the measurements and their approximations for a closing valve are shown in figure 4.19

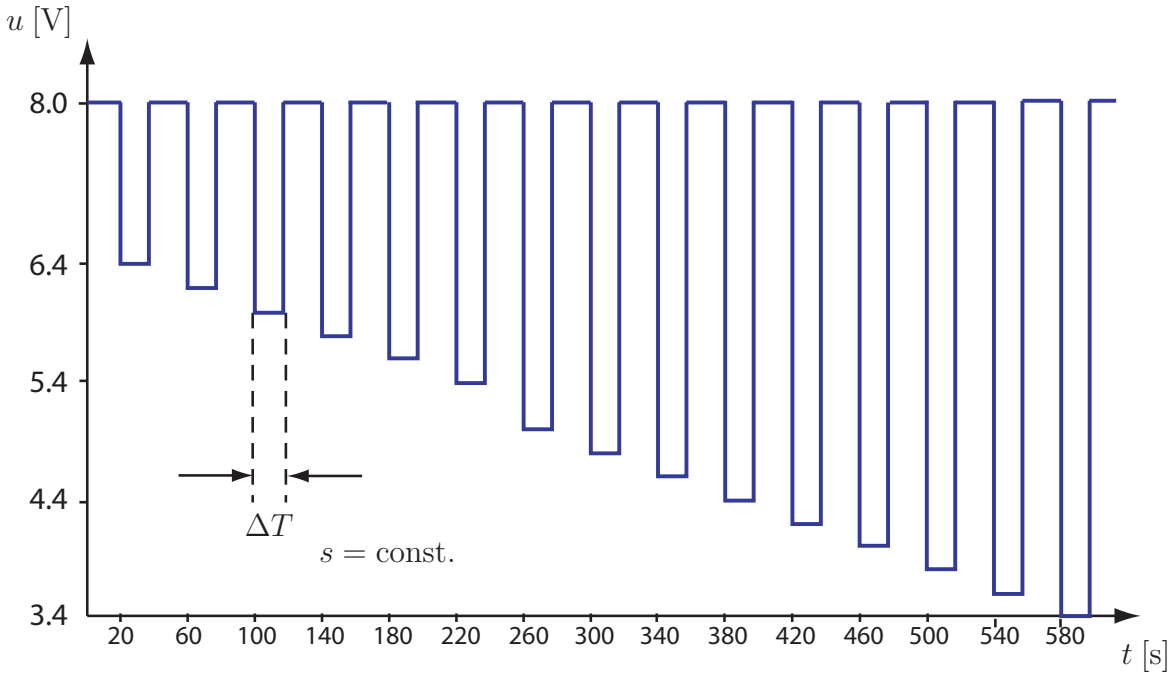

Figure 4.15: Voltage step function for inducing pressure decreases at constant strokes

for voltage jumps functions from $8\,\mathrm{V}$ to $4\,\mathrm{V}$, $4.4\,\mathrm{V}$ and $5\,\mathrm{V}$. The respective pressure rates are given in figure 4.20. The measurements are sufficiently matched with the approximations, but there are differences in the pressure rate (see fig. 4.20) at high pressures for the closing valve, which is again due to higher-order valve dynamics at the beginning of the time histories, which again stem from the sudden valve closening. A future work might identify their behavior based for example on PT_3 models. For the present care the approximations were sufficient. The parameters k_{inc1}, k_{inc2}, ℓ_{dec1} and ℓ_{dec2} are depicted in Figure 4.21 as a function of voltage step amplitude as well as actuator stroke. It can be seen that the parameters have a significant dependency of voltage but are quite insensitive to muscle stroke. This is because the dynamic behavior is mainly due to valve dynamics and do not depend on the volume of the air column in the fluidic muscle. The parameters are later determined in the simulation using look-up tables and interpolation.

4.4 Model-based force control

The task of the model-based force control is to inflate the fluidic muscle such that a given target force F^T is achieved. The control algorithm consists of a closed-loop control model as depicted in figure 4.22. The feedforward model contains the inverse of the actuator model. With the feedback of the controlled variable combined with a feedforward, the algorithm allows an improved response of the actuator control to variations of the target value and external disturbances. In the inverse model, the valve voltage is the output value and the target force is the input value. The remaining error e is inserted into a PID controller, which generates the correcting actuating signal u_c. The resulting actuating signal u is the sum of the signals u_V and u_c resulting from the feedforward and

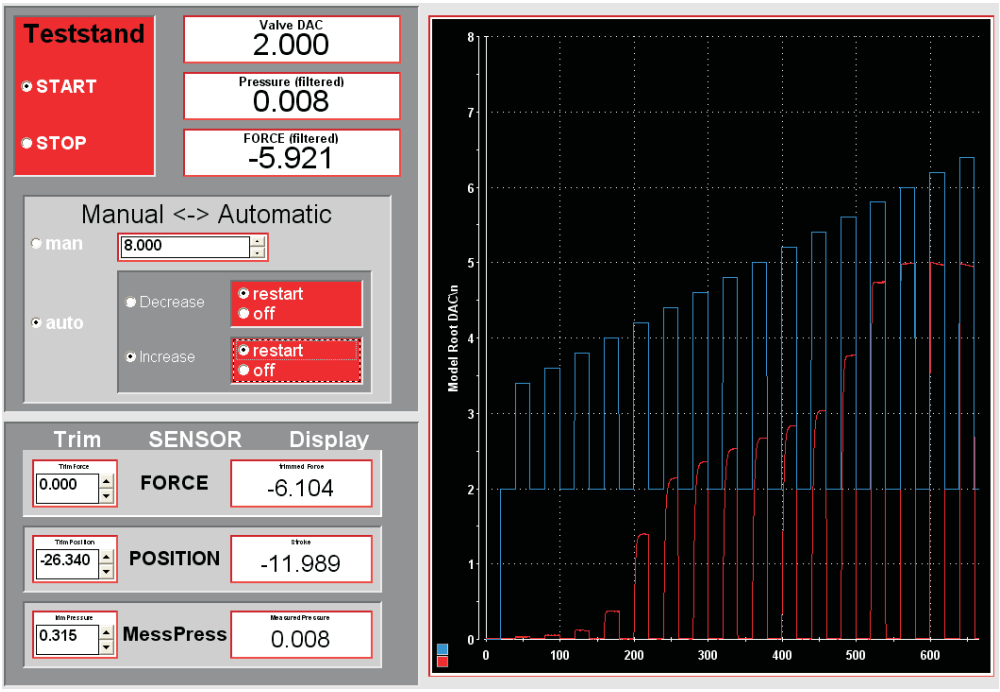

Figure 4.16: Management of measurement in Control Desk

the PID controller. In the current application, the actuating signal u is the voltage which actuates the piston of the proportional valve. In order to determine a target voltage U^T which will achieve a given target force F^T at the actuator, one has on the one hand the force relationship from equation 4.28, which can also be parametrized (for fixed s) as a univariate function of pressure p

$$F(s,p) = g(s,p) = g_s(p) \tag{4.34}$$

On the other hand, one has the differential equation 4.21, which, after resolving for the first term, yields

$$\hat{f}_{1(s,p)}(u) = \tilde{f}_1(s,u,p) = \dot{p} - f_2(s,p,\dot{s})\ . \tag{4.35}$$

For a given stroke s, stroke rate $\dot{s}$ and pressure p, equation 4.35 can be regarded as a pure function $\hat{f}_{1(s,p)}(u)$ of u which can be resolved for the target voltage as

$$u(p,s,\dot{s}) = \hat{f}^{-1}_{1,s,p}\left[\,\dot{p} - f_2(s,p,\dot{s})\,\right]\ . \tag{4.36}$$

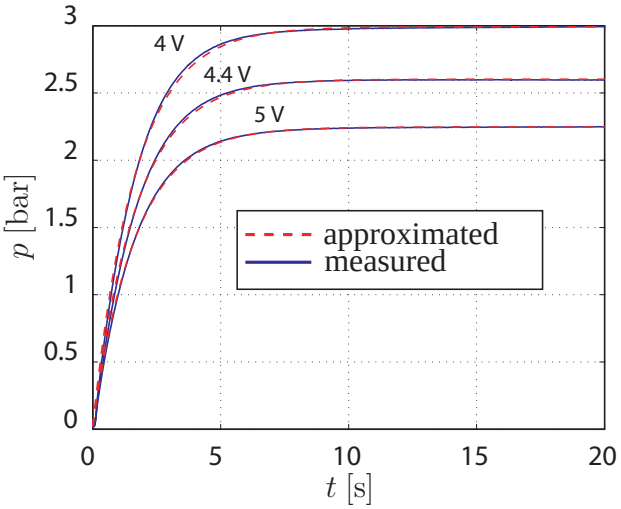

Figure 4.17: Pressure responses for opening valve

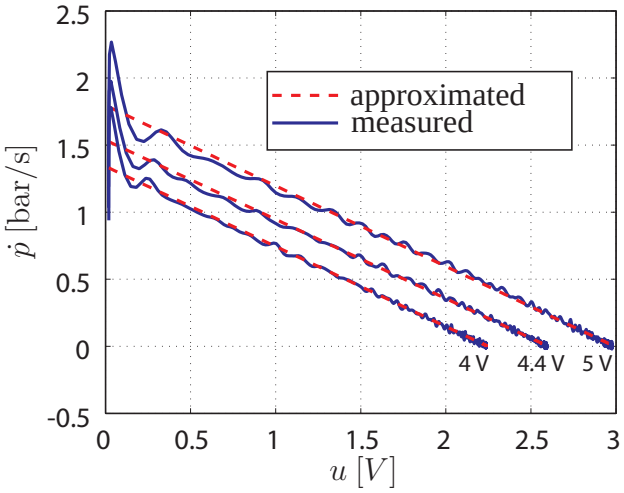

Figure 4.18: Pressure rates for opening valve

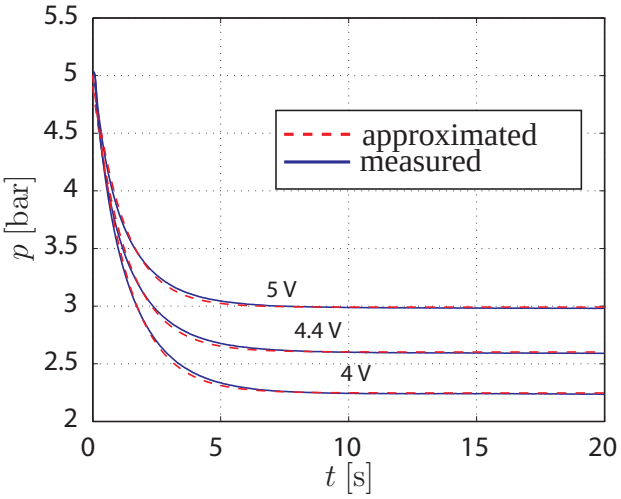

Figure 4.19: Pressure responses for closing valve

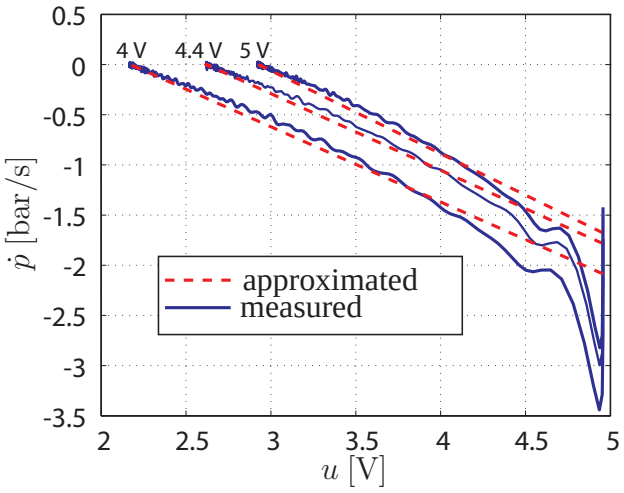

Figure 4.20: Pressure rates for closing valve

In order to evaluate this equation, one needs approximations for the stroke rate, the target pressure and the target pressure rate at any state of the system. These are proposed to be determined as follows. The stroke rate can be approximated by backward finite differences

$$\hat{\dot{s}}(t_i) = \frac{s(t_i) - s(t_{i-1})}{\Delta t}; \quad \hat{\dot{s}}(t_0) = 0\,. \tag{4.37}$$

The target pressure p^T is obtained from the inverse of the univariate force-pressure function of equation 4.34 as

$$p^T = g_s^{-1}(F^T)\,. \tag{4.38}$$

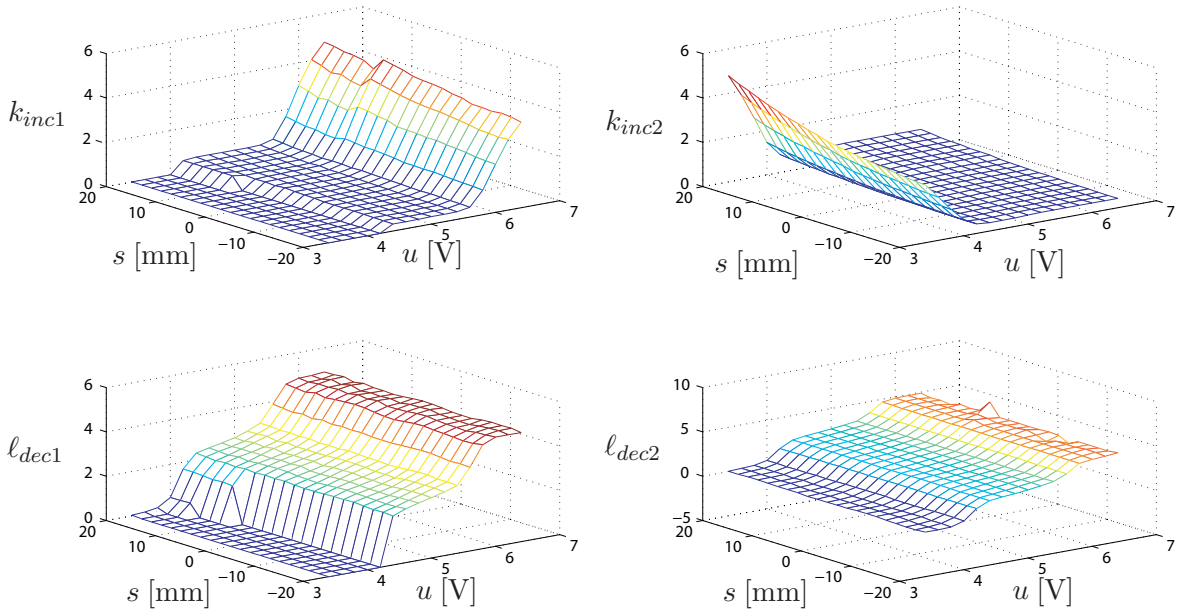

Figure 4.21: Parameters of exponential functions

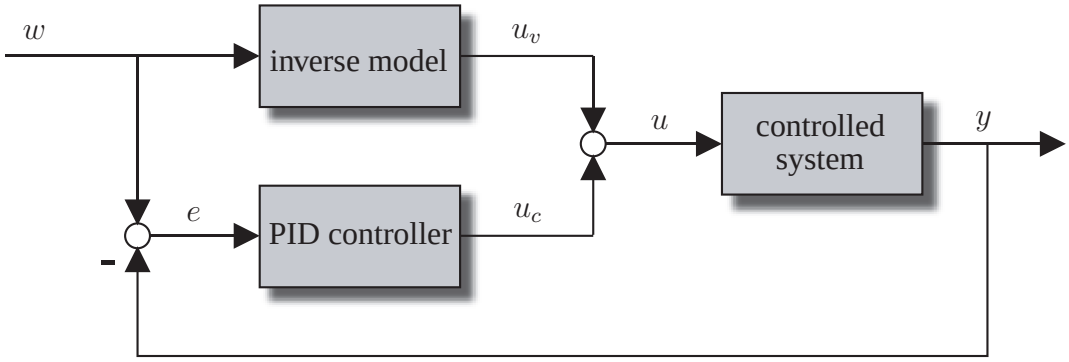

Figure 4.22: Application of approximated gas-dynamic behavior on model

Finally the target pressure rate is approximated by a virtual pressure rate $\tilde{\dot{p}}^T$ obtained by the assumption that the target pressure p^T will be achieved from the current pressure p after some time delay ΔT. The interpretation of this approach then yields

$$\tilde{\dot{p}}^T(t_i) = \frac{p^T(t_i) - p(t_i)}{\Delta T} \,. \tag{4.39}$$

After inserting the above mentioned approximations into equation 4.36, the following expression

$$U^T(t) = \hat{f}^{-1}_{1,s,p}\left(\tilde{\dot{p}}^T + \frac{p}{V(s)} \cdot \frac{\mathrm{d}V(s)}{\mathrm{d}s}\hat{\dot{s}}\right) \tag{4.40}$$

is obtained for the target valve-voltage.

By regarding the obtained equations, the control scheme in Figure 4.23 is achieved. In case of a

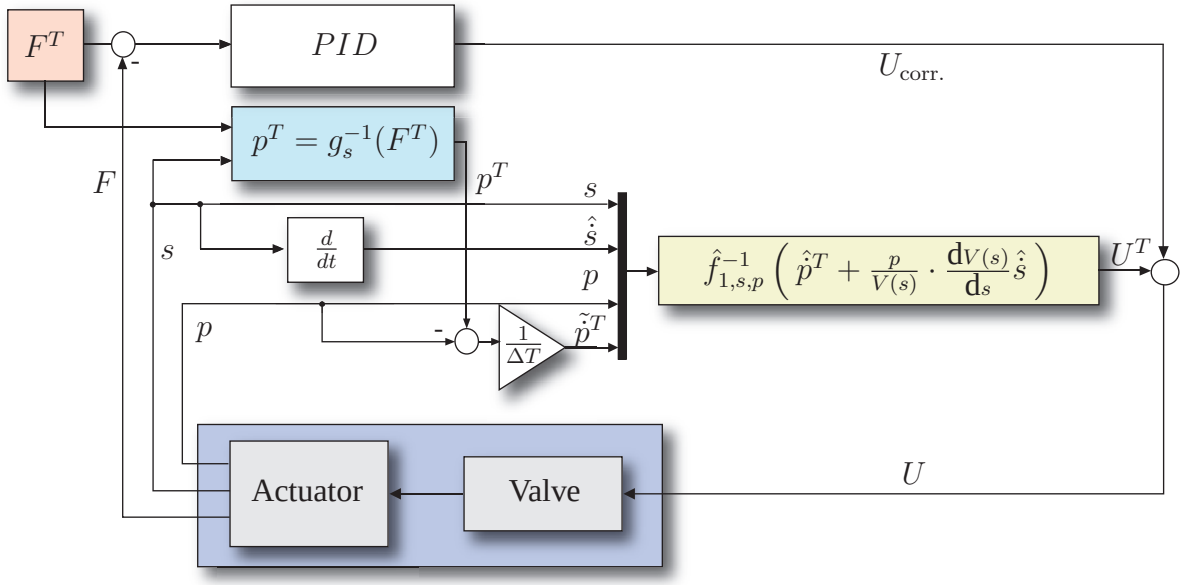

Figure 4.23: Actuator control scheme [23]

perfect inverse model, the measured force is equal to the target force, but however due to modeling inaccuracies there can remain slight differences between the target force F^T and the measured force F. In order to reduce the differences, the error $e = F^T - F$ is inserted into a PID controller generating a correcting voltage which then is added to the target voltage. The total voltage $U = U^T + U_{\text{corr.}}$ then actuates the valve which transmits the pressure p to the fluidic muscle. As a consequence, the fluidic muscle produces the target force.

4.5 Uniaxial test stand

All test runs of the identification procedure (section 4.3) and the closed-loop control (section 4.4) were conducted on the test bed shown in Figure 4.24. In order to limit the variability of the identification parameters, each actuator was always operated with its own assigned valve and sensors. Thus, the properties of the actuators were disposed on six individual actuator systems (valve-actuator-sensors). Since the experiments conducted on each actuator are significant for the outcome of the 6-DOF control on the parallel platform, it had to be ensured that the properties of an actuator which is fixated on the uniaxial test bed shall not differ from the conditions when embedded into the 6-DOF platform. Therefore, when the actuators are shifted from the 6-DOF platform to the test bed for experiments, the respective actuator is kept together and is not dismantled before it is installed on the test stand. Here, the attachment bolts on the uniaxial test bed are same to that one of the parallel platform. Moreover, the uniaxial test bed is located in the same lab and fixated on the same basement next to the parallel platform for keeping the environmental conditions as similar as possible. The assembly was provided with slots and the respective sliding bocks with screw connections, such that the framework was flexible enough for modifications.

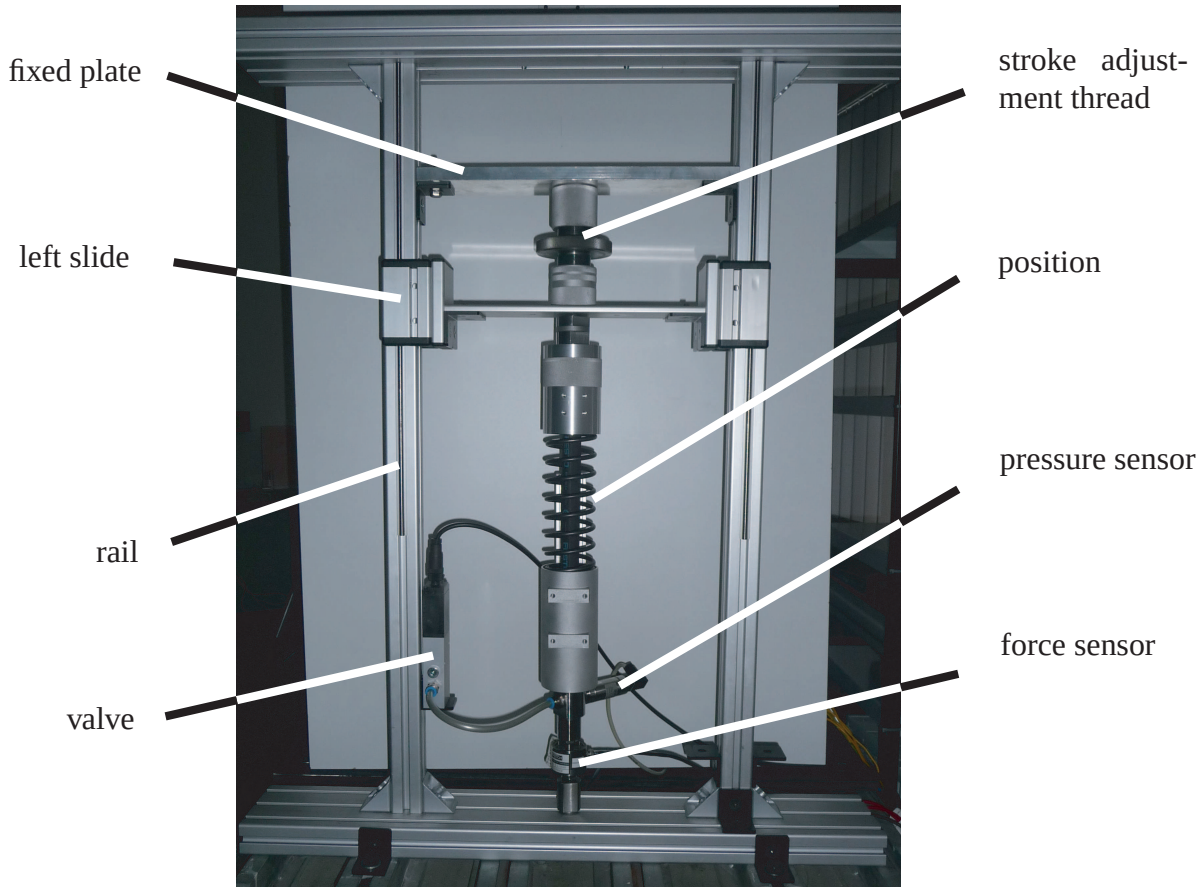

Figure 4.24: Uniaxial test stand

The stand consists of a horizontal plate which is connected from both ends with two respective slides. Each slide is provided with two opposite roller pairs which are guided by rails embedded into the left and right pillar (Figure 4.24). The top of the tested actuator is connected to the horizontal mobile plate and the bottom is connected to the force sensor which is fixated on the bottom plate of the frame. As the configuration of the actuator components is not changed, also the position encoder and the pressure sensor are connected in the same way to the actuator as it has been done on the parallel platform. In Figure 4.24, the position encoder is located behind the actuator and the pressure sensor is connected to the bottom of the actuator. The valve is fastened to the left pillar for keeping the distance to the fluidic muscle as low as possible. For all measurements, the movable plate was connected to a horizontal fixated plate. The plates were connected to each other via a stroke adjustment unit, which consisted of a cylindrical element with two male threads paired with female thread bolts at the top and at the bottom. The upper bolt/screw connection consisted of a left hand fine thread and the lower one had a right hand fine thread. Hence, with rotating the center part in clockwise or counter clockwise direction, the distance between the upper and lower bolt can be increased or decreased. Since the upper bolt is connected to the fixed plate and the lower bolt is connected to the movable plate, the position of the mobile plate linked to the top of the actuator can be varied accurately. The stroke prescription of the actuator with the described bolt-screw unit was significant for the measurements of $F = g(s, p)$ and the measurements of the pressure increases and decreases at different strokes.

The signal flow between the components of the test stand and the corresponding electrical instruments is shown in Figure 4.25. All three measured signals are inserted into an analog/digital converter board (dSPACE DS 2002). This board has two independent A/D converters with 16 multiplexed inputs with a 16-bit resolution each, such that in general 32 input signals can be sampled. For the hexapod, 18 inputs are used due to the six actuator systems with three sensors each. The

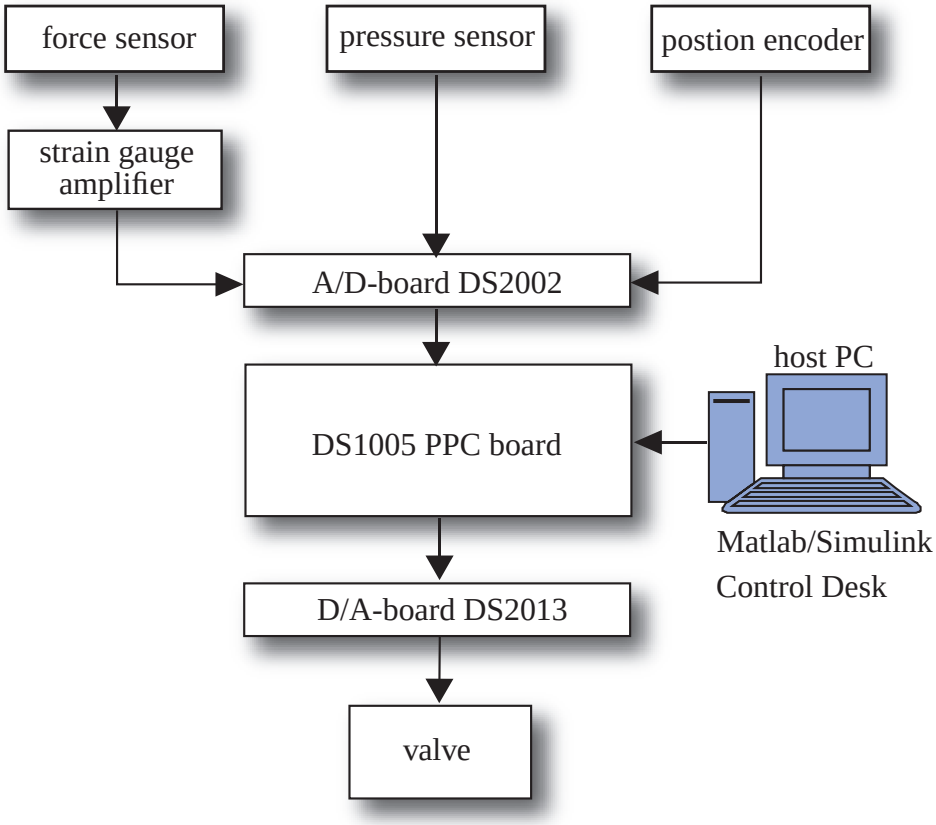

Figure 4.25: Signal flow chart

pressure sensor and the position encoder have an output of $0 - 10\,\mathrm{V}$, in contrast the force sensor has to be amplified with a strain gauge amplifier, in order to get an output signal of $0 - 10\,\mathrm{V}$. The A/D board is connected to the DS 1005 PPC board which contains the controller unit including a PowerPC750 processor. This controller board is connected via a glas fibre cable to a host PC, on which Matlab/Simulink is run.

The algorithms for the measurements and the closed-loop control (sections 4.3 and 4.4) are programmed with Simulink, specific functions of the algorithm were written in Matlab and integrated into the Simulink model file. The obtained model in Simulink is transcribed into a C-code using a cross compiler, the obtained C-file is then transmitted to the controller board. The control unit has its own operating system which is running independent from the operation system of the host PC.

The signal output of the controller board is processed with the D/A board DS 2013. This board features 32 analog outputs which are linked to BNC interfaces. The BNC interfaces of the A/D

and D/A board allow convenient interconnection to the analog sensors and valves. In this case of the uniaxial test stand the D/A board is connected to one single valve (Figure 4.25) which inflates the fluidic muscle which is installed on the test stand.

An overview of the pneumatic components belonging to the test stand is presented in the pneumatic schematic in Figure 4.26. Before the incoming compressed air is transmitted to the valve it is preprocessed with pressure reservoirs (1) and a service unit comprising the components from 2 to 5 (FESTO). Pressure reservoirs of 2 liters volume each help to compensate unsteady pressure variations of the compressed air between 6.1 and 7.0 bar of the pressure supply line. The entrance of the service unit consists of a manual on-off valve, which slowly increases the pressure after it is switched on, such that the pneumatic components are pressurized smoothly during the start-up phase.

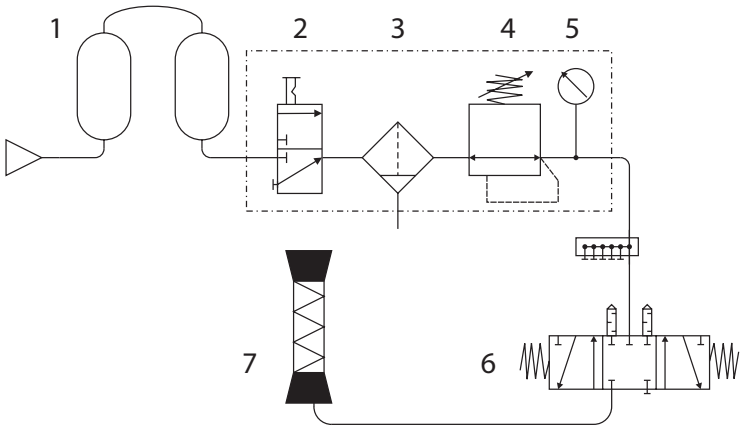

1. pressure reservoirs
2. manual on-off valve
3. condensate separator and air filter
4. pressure controller
5. manometer
6. proportional valve
7. fluidic muscle

Figure 4.26: Pneumatic schematic

The rack which carries all the electrical instruments belonging to the test stand is depicted in Figure 4.27. The BNC boxes which are connected to the A/D and D/A boards of the control unit are placed on the top of the rack. All the power units of the pressure sensors, position encoders and valves are integrated in a special housing which is found on the second level of the rack below the BNC boxes. The force sensors need an own amplifier which is located next to the dSPACE system box. The pressure reservoirs and the service unit are placed at the very bottom level of the instruments rack, the reservoir tanks are connected to the supply pressure interface which is located next to the rack.

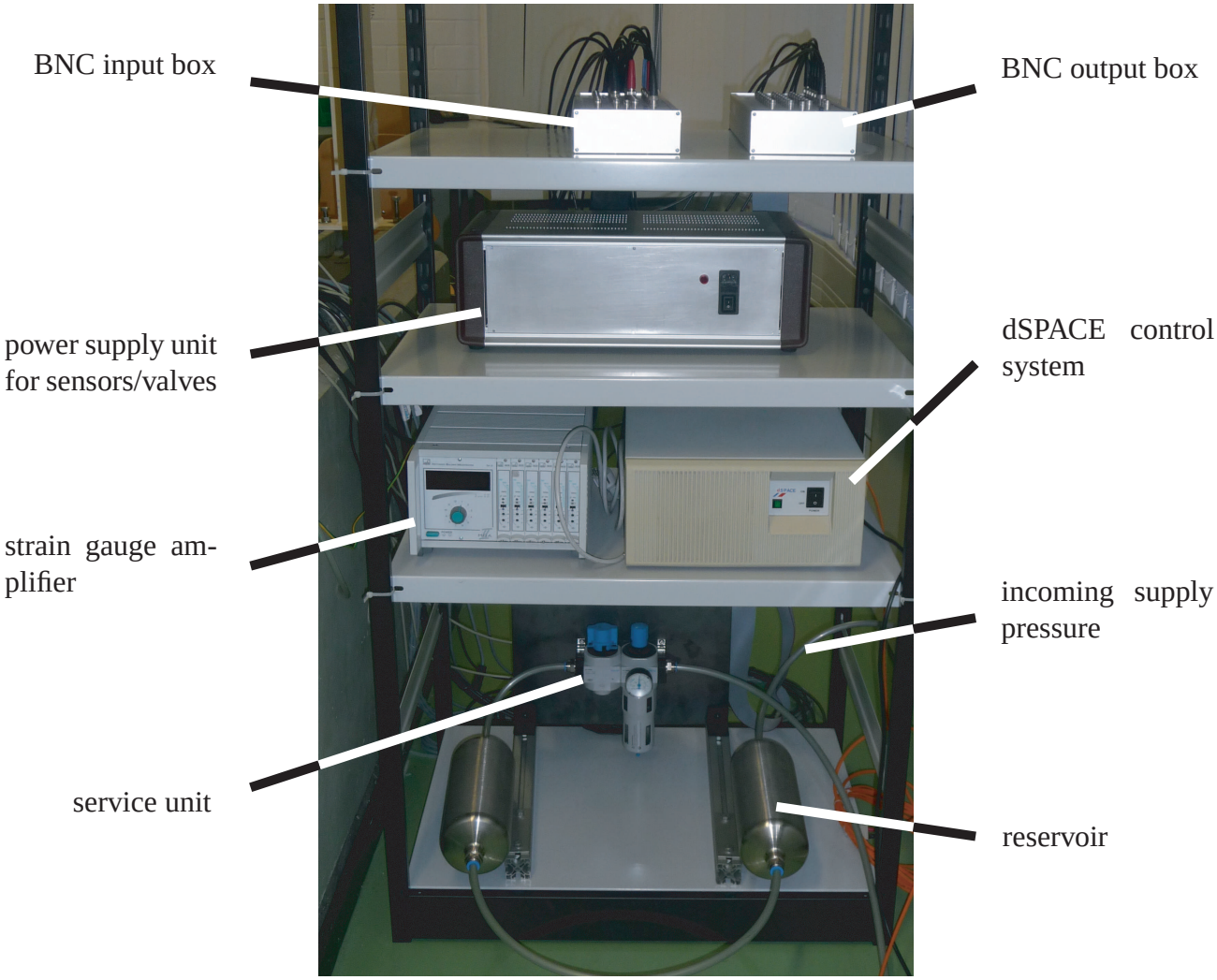

Figure 4.27: Instruments rack

4.6 Experimental results of actuator control

Although the muscles are of the same production series and are connected with the same standard components as valves, pressure adapters etc., the individual voltage-pressure behaviors of the six actuators may diverge. For this reason, an own inverse model for each actuator was determined.

Due to the high gain of the fluidic muscles from pressure to force (10 mbar leads to an oscillation of $3\,\mathrm{N}$) the accuracy of the current pressure sensors allows only for a force control with an accuracy of 3 to $4\,\mathrm{N}$. Thus, this tolerance is used to assess the following experiments.

The first test involves a pure feed-forward test of the fluidic models. Before the inverse model was applied in the control, the model was tested. The model was tested with voltage step signals. The figures 4.28 and 4.29 show the results for a voltage jump from $0\,\mathrm{V}$ to $5.5\,\mathrm{V}$ and from $0\,\mathrm{V}$ to $6\,\mathrm{V}$, respectively. The results for the lower voltage of $5.5\,\mathrm{V}$ show that the measured pressure and position are almost matched in each point with the simulation results. For the larger voltage jump with $6\,\mathrm{V}$ there are slight differences in the transient area of the simulated pressure and positions. This is due to the dynamics of the valve and needs to be compensated by control.

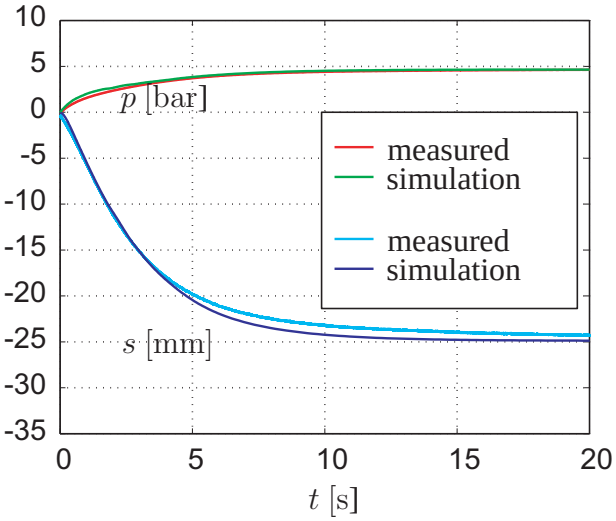

Figure 4.28: Step response for $u = 5.5$ [V]

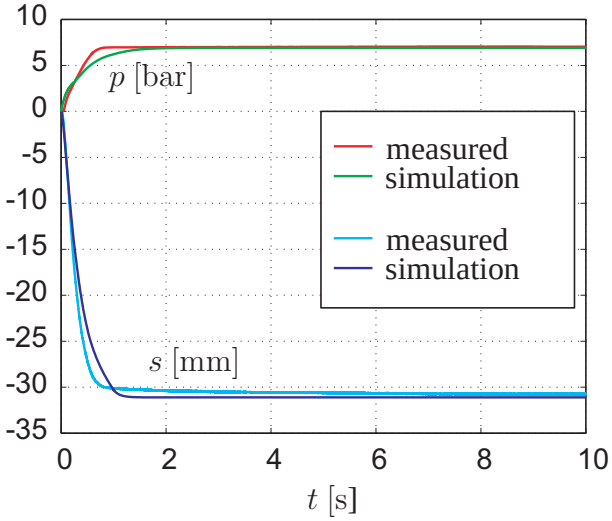

Figure 4.29: Step response for $u = 6$ [V]

A second feed-forward test was performed with a periodic triangular target (Figure 4.30). The diagram (”-”tensile forces; ”+” pressure forces) shows that the target value is followed by the measured value. Hence, the simplification of the pressure rate ODE and the approximation of the volume-stroke and pressure/force-stroke relationship in the inverse model is suitable for a model-based force control of the actuator.

For the adjustment of the PI controller gains, a Ziegler-Nichols method was tested.

However, this controller performed instably due to the nonlinearity of the system. Instead, a set of PI parameters was determined using sinusoidal and triangular reference signals. A maximum error of ± 3 N was allowed. Table 4.4 shows the proportional and integral gains (K_P, K_I) of the PI controller and the selected quotient $\frac{1}{\Delta T}$. The determined parameters of table 4.4 were interpolated using *lookup-table blocks* in Simulink. We verified that a decreased value of ΔT led to a better performance of the feedforward (inverse model) at tensile forces. Furthermore, it can be seen that all parameters have similar values when the actuator force is within ± 100N. However, at higher tensile forces the values vary stronger.

In a first step, a quasistatic sinusoidal trajectory with 80 s period was prescribed. Figures 4.31 to 4.33 show the results for force variation between $+250$ N and -250 N. One recognizes that the achieved error does not exceed the demanded range and is even smaller than the required ± 3 N.

Hence, the PI controller and the inverse model perform satisfactorily using the aforementioned procedure for slow variations.

When applying the triangular test signal of Figure 4.30, the error remains within ± 5N. These errors result from the sudden change of slope of the force time history and the jumps in the pressure rate.

The effect of sudden pressure rate changes is even more pronounced when step functions are applied as inputs. In Figure 4.35 the results for step inputs with an amplitude of ± 200N are

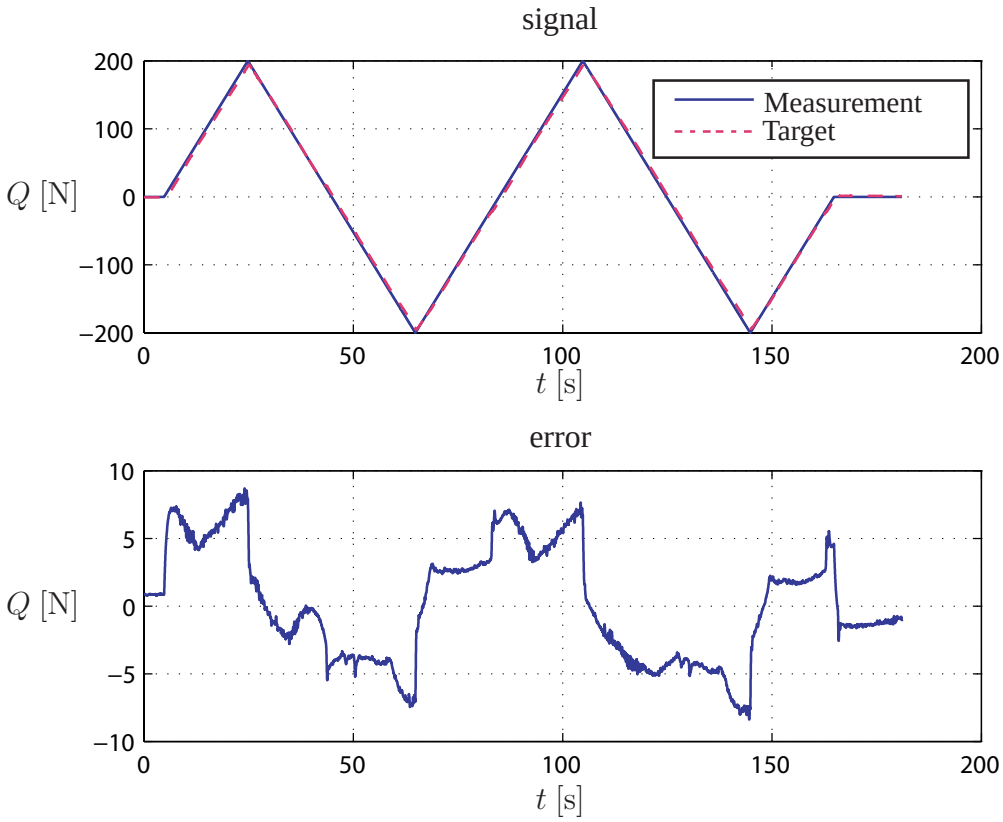

Figure 4.30: Actuator force control without PI controller

depicted. It can be observed that unstable situations are avoided; however the errors reach an amount of 50 % of the step value specifically at the beginning of the force jumps.

The results show that the control behavior is satisfactory for slow (quasistatic) force changes. However, for fast (dynamic) force changes, further needs to be done. This involves higher-order valve dynamics models as well as better environment models.

Force [N]	K_P	K_I	$\frac{1}{\Delta T}$
200	0.004	0.02	2
150	0.004	0.0275	2
100	0.004	0.0275	2
50	0.004	0.0325	2
0	0.004	0.06	2
-50	0.004	0.06	2
-100	0.004	0.06	2
-150	0.004	0.035	2
-200	0.004	0.015	4
-250	0.001	0.015	4
-300	0.001	0.015	4
-350	0.001	0.02	4
-400	0.0005	0.04	6

Table 4.4: Experimentally determined gains of PI controller and reciprocals of ΔT

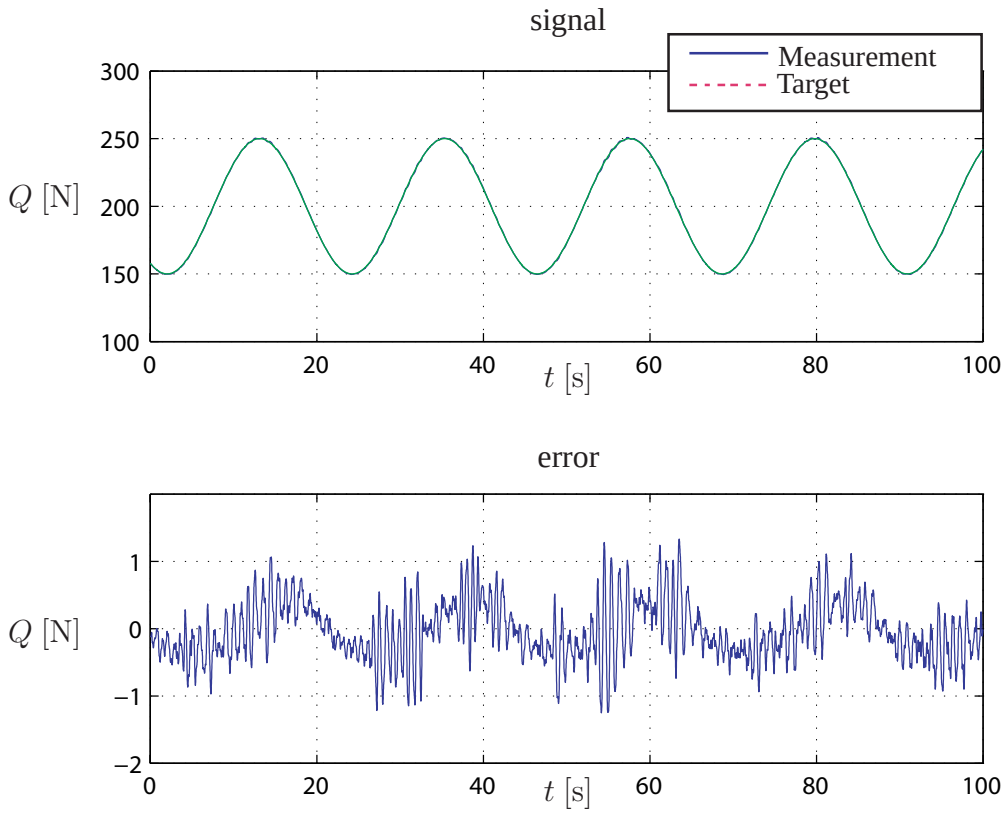

Figure 4.31: Sinusoidal signal with offset force of 200 N

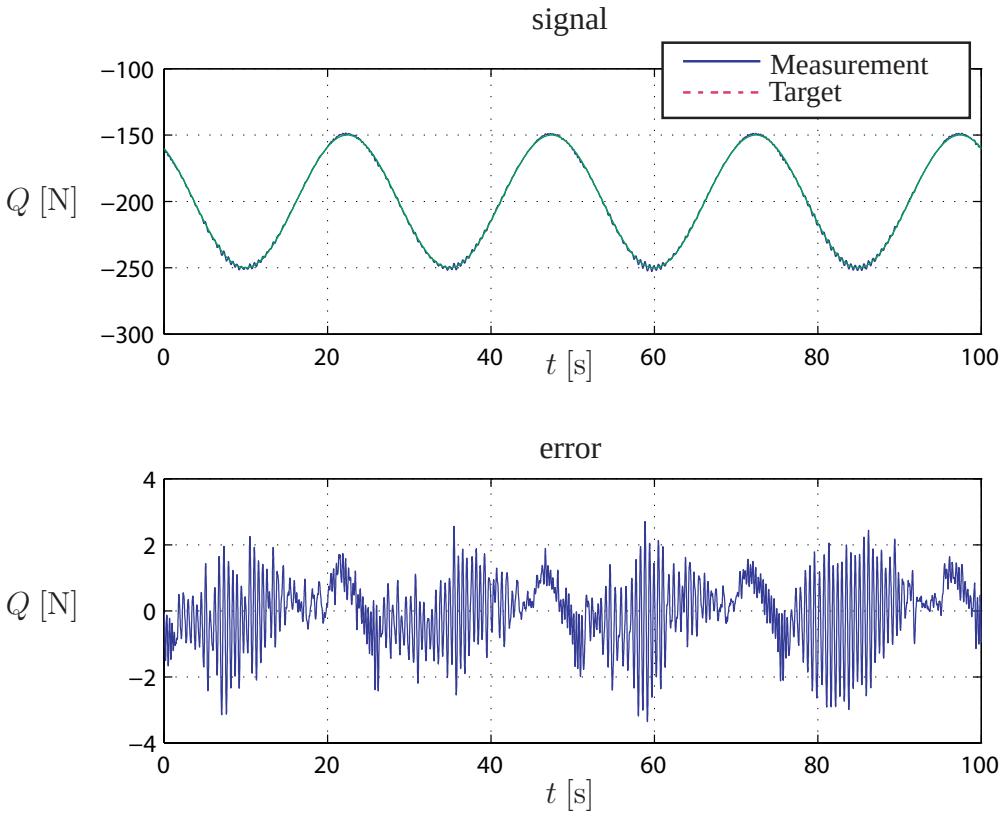

Figure 4.32: Sinusoidal signal with offset force of -200 N

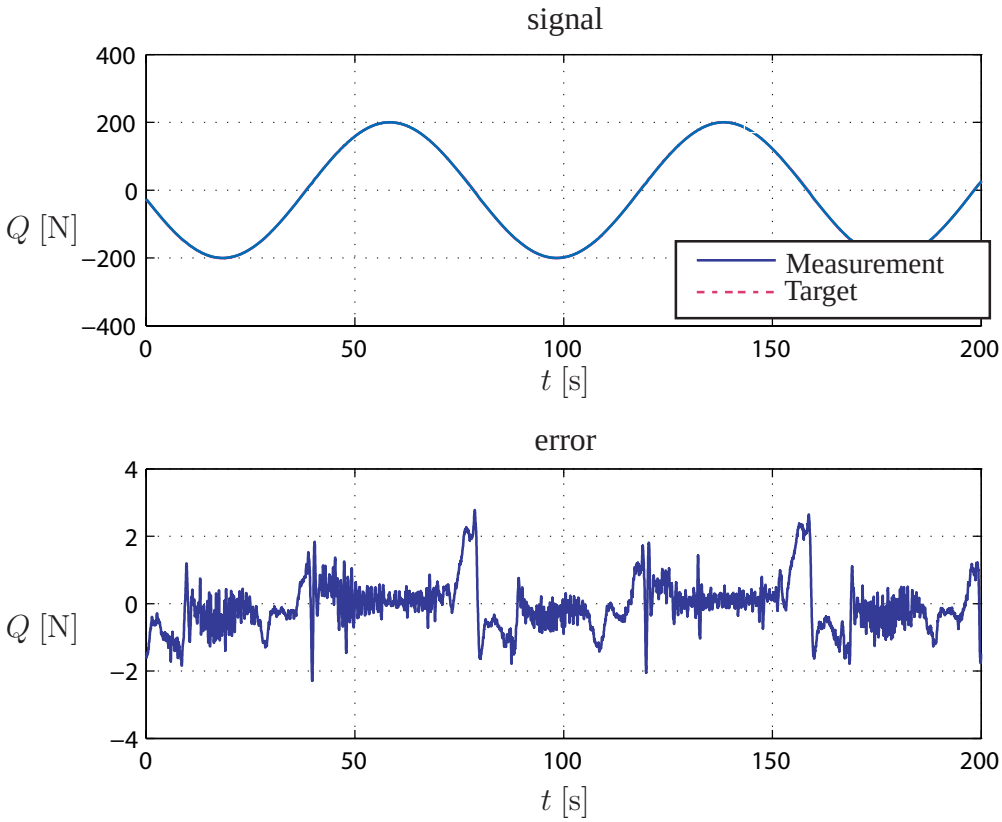

Figure 4.33: Actuator force control with sinusoidal signal

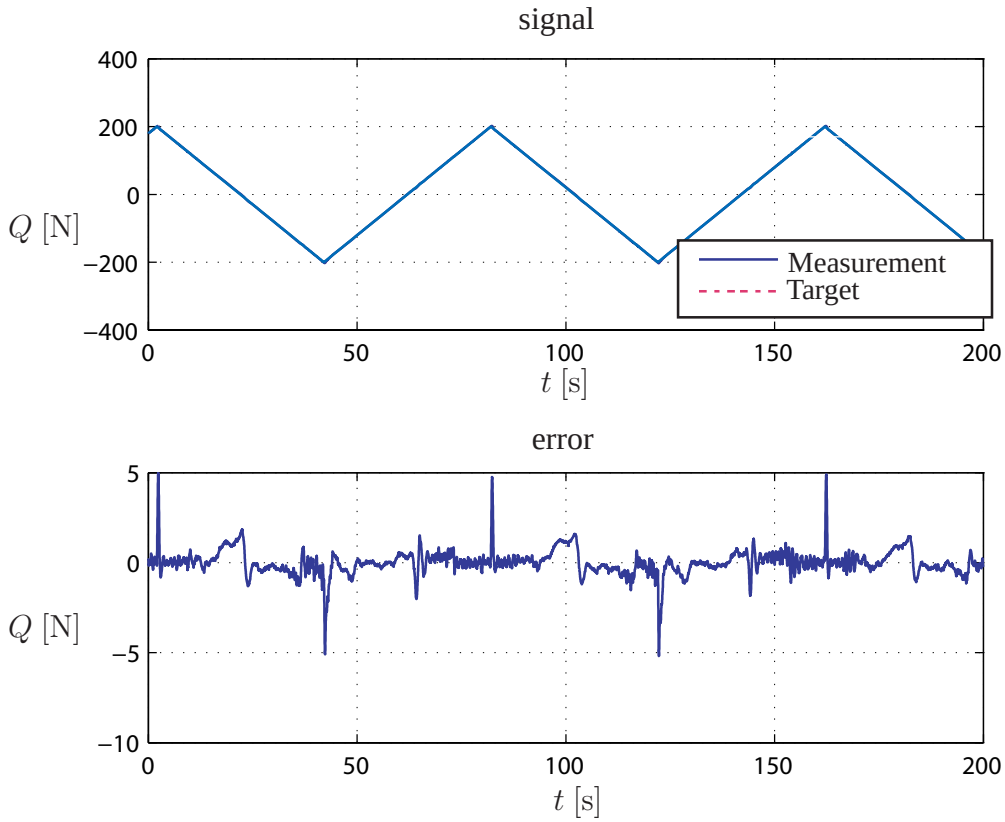

Figure 4.34: Actuator force control with triangle signal

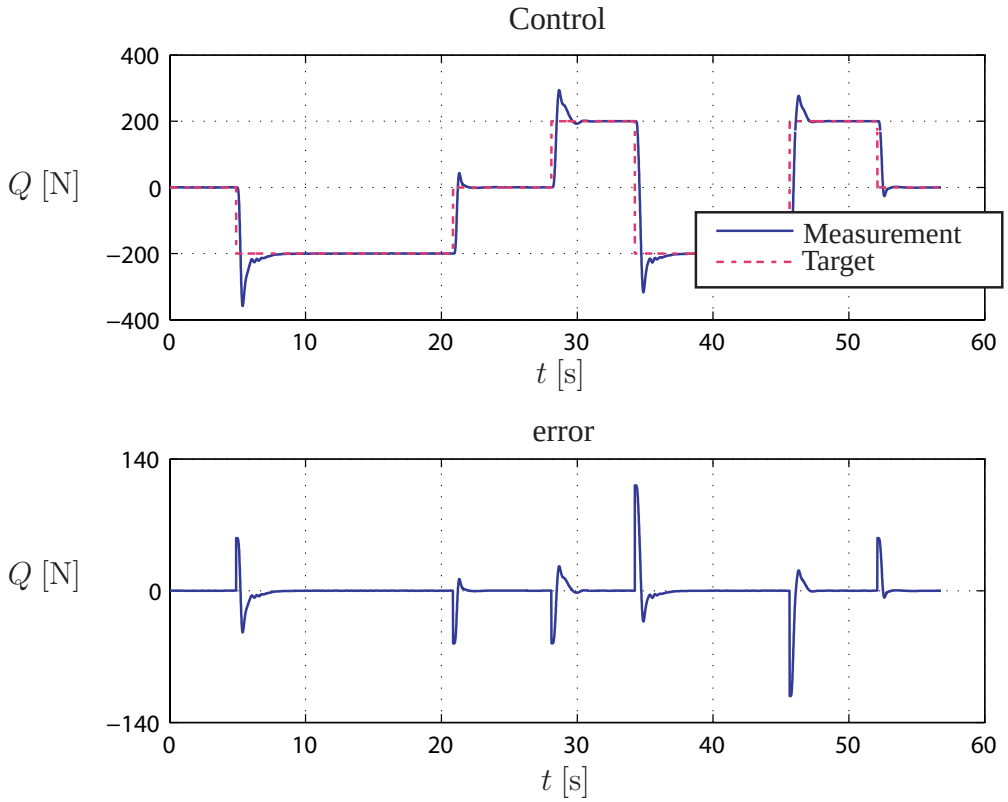

Figure 4.35: Actuator force control with jump variation

5 Application to 6-DOF Platform

In this chapter, the final platform control and its experimental validation are presented. To this end, first the kinetostatics and dynamics of the platform are described. Then, the central control scheme and its implementation in a dSPACE system are discussed. The last section describes the experimental results obtained for the platform.

5.1 Kinetostatics of the passive components of the platform

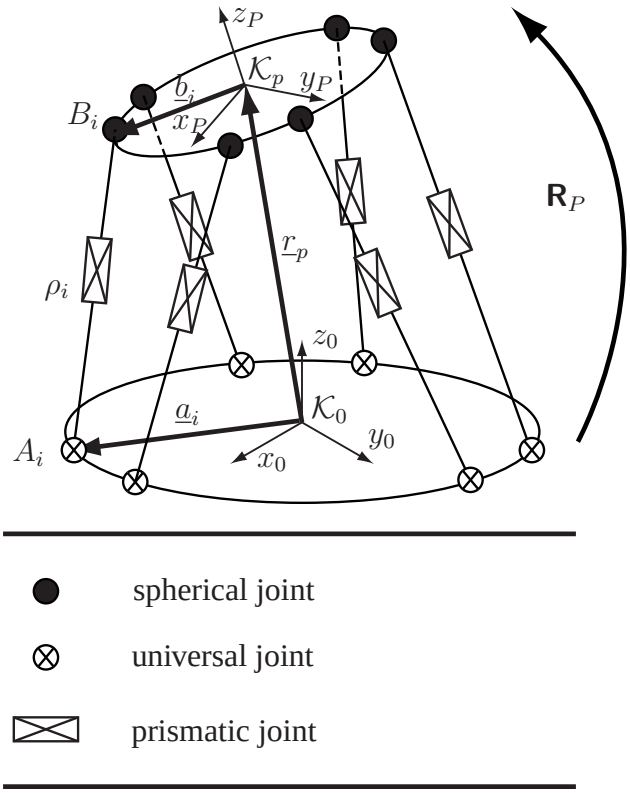

Figure 5.1: Kinematic scheme of the Hexaspine platform

The structure of the Hexaspine platform (Figure 5.1) consists of a rigid base plate and a motion plate, both connected with six links arranged with a universal joint, a prismatic joint and a spherical joint. The prismatic joint in this case is the actuated joint. The current leg length of the i-th leg

is ρ_i. $\mathcal{K}_0$ and $\mathcal{K}_p$ are the respective frames of the base and motion plate. The rotation matrix transforming coordinates with respect to the moving frame to coordinates with respect to the base frame is:

$$\mathbf{R}_P = \begin{bmatrix} \cos\beta\cos\gamma & -\cos\beta\sin\gamma & \sin\beta \\ \cos\alpha\sin\gamma + \sin\alpha\sin\beta\cos\gamma & \cos\alpha\cos\gamma - \sin\alpha\sin\beta\sin\gamma & -\sin\alpha\cos beta \\ \sin\alpha\sin\gamma - \cos\alpha\sin\beta\cos\gamma & \sin\alpha\cos\gamma + \cos\alpha\sin\beta\sin\gamma & \cos\alpha\cos beta \end{bmatrix} .$$

The rotation is described with bryant angles, using respectively α, β and γ according to the sequence x, y and z.

The vectors $\underline{a}_i$ and $\underline{b}_i$ connect the origins of the moving and the fixed platform to the corresponding attachment points of the legs. There are two methods for solving the kinematics of the current mechanism. The determination of the leg strokes $\underline{\rho}$ for a given pose $\underline{X}$, which includes the position coordinates P_x, P_y, P_z with respect to the frame $\mathcal{K}_0$ and the orientation angles α, β and γ, is called inverse kinematics.

For parallel mechanisms this method is advantageous, since the leg strokes can be computed independently of each other with one single solution for each leg. The six leg lengths are defined as:

$$\underline{\rho} = [\rho_1\ \rho_2\ \rho_3\ \rho_4\ \rho_5\ \rho_6]^{\mathrm{T}} . \tag{5.1}$$

The pose of the platform at $\mathcal{K}_P$ may be described with the vector

$$\underline{X} = [P_x\ P_y\ P_z\ \alpha\ \beta\ \gamma]^{\mathrm{T}} . \tag{5.2}$$

According to the definition of inverse kinematics, all six leg lengths of the platform can be determined for a given pose by a nonlinear function

$$\underline{\rho} = f(\underline{X}) . \tag{5.3}$$

The position and orientation of the frame $\mathcal{K}_P$ is defined by the vector $\underline{r}_P$ and the rotation matrix $\mathbf{R}_P$ (Figure 5.1). The leg length ρ_i of a leg A_iB_i (Figure 5.1) can be determined as follows:

$$\rho_i = \| -\boldsymbol{a}_i + \boldsymbol{r}_p + \mathbf{R}_P\,\boldsymbol{b}_i \| , \tag{5.4}$$

where the vectors $\boldsymbol{a}_i$ and $\boldsymbol{b}_i$ are constant and known.

Kinetostatic transmission elements are units which transmit motion and forces. The transmission behavior of a kinetostatic transmission element can be described by considering a simple element mapping a set of n scalar input variables $\underline{q} \in \mathbb{R}^n$ to a set of m scalar output variables $\underline{q}' \in \mathbb{R}^m$, as displayed in Figure 5.2. The transmission of motion involves the mapping of the input variables

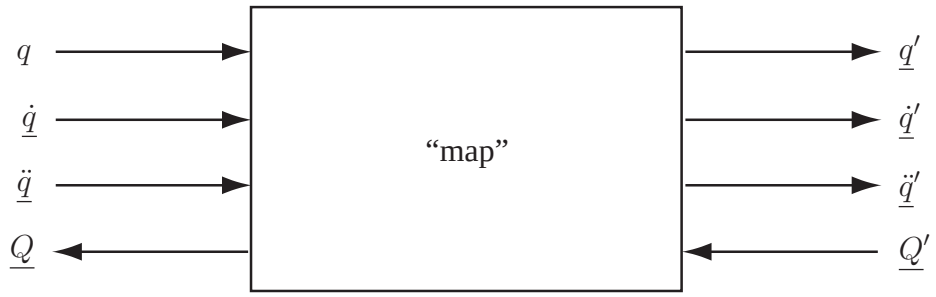

Figure 5.2: General kinetostatic transmission element of Kecskeméthy and Hiller [53]

$\underline{q}$ to a corresponding set of output variables $\underline{q}'$. As well, the time derivatives $\dot{\underline{q}}$ and $\ddot{\underline{q}}$ of the input coordinates, i.e., the velocity and acceleration are mapped to the corresponding time derivatives $\dot{\underline{q}}'$ and $\ddot{\underline{q}}'$ of the output coordinates. Apart from the kinematic transmission functions, the kinetostatic transmission element also induces a transmission of forces. This transmission is directed in opposite direction to the transmission of motion, mapping the forces $\underline{Q}'$ at the output of the kinetostatic transmission element to corresponding forces $\underline{Q}$ at the input [51]. The transmission of motion is governed by the following formulas:

$$\begin{aligned} \underline{\text{position:}} \qquad \underline{q}' &= \phi(\underline{q}) \,, \\ \underline{\text{velocity:}} \qquad \dot{\underline{q}}' &= \mathbf{J}_\phi \, \dot{\underline{q}} \,, \\ \underline{\text{acceleration:}} \qquad \ddot{\underline{q}}' &= \mathbf{J}_\phi \, \ddot{\underline{q}} + \mathbf{J}_\phi \, \dot{\underline{q}} \;. \end{aligned} \tag{5.5}$$

where $\mathbf{J}_\phi$ represents the *Jacobian* of the transmission element and is defined as:

$$\mathbf{J}_\phi = \frac{\partial \underline{\phi}}{\partial \underline{q}} \in \mathbb{R}^{m \times n} \,. \tag{5.6}$$

For the transmission of forces it is assumed that the transmission is ideal, i.e., that it neither generates nor consumes power. Then, due to the equivalence of virtual work at the input and output, it follows

$$\delta \underline{q}^{\mathrm{T}} \, \underline{Q} = \delta \underline{q}'^{\mathrm{T}} \, \underline{Q}' \,. \tag{5.7}$$

After substituting with $\delta \underline{q}' = \mathbf{J}_\phi \, \delta \underline{q}$ one obtains

$$\delta \underline{q}^{\mathrm{T}} \, \underline{Q} = \delta \underline{q}^{\mathrm{T}} \, \mathbf{J}_\phi^{\mathrm{T}} \underline{Q}' \, , \tag{5.8}$$

which holds for all $\delta \underline{q} \in \mathbb{R}^n$. Hence, a relationship between $\underline{Q}$ and $\underline{Q}'$ is obtained which describes the force transmission as follows:

$$\underline{Q} = \mathbf{J}_\phi^{\mathrm{T}} \, \underline{Q}' \, . \tag{5.9}$$

In general, the Jacobian $\mathbf{J}_\phi$ is not quadratic, so equation 5.9 cannot be solved for $\underline{Q}'$. That is why for most transmission elements the relationship of force cannot be reversed. Hence, the natural direction of force transmission is in opposite direction to the motion mapping [53], as it is described in Figure 5.2 .

The basic kinetostatic equations related to the Hexaspine platform can be established using the standard kinematic terminology, which was introduced in the previous section 5.1. Hence, the kinematics of the platform is described by the six scalar constraint equations

$$\rho_i^2 = \| \, \underline{r}_P + \mathbf{R}_P \, \underline{b}_i - \underline{a}_i \, \|^2 \quad i = 1, \ldots, 6 \tag{5.10}$$

where ρ_i (see Figure 5.3) is the current length of the i-th leg. For the velocity kinematics, angular

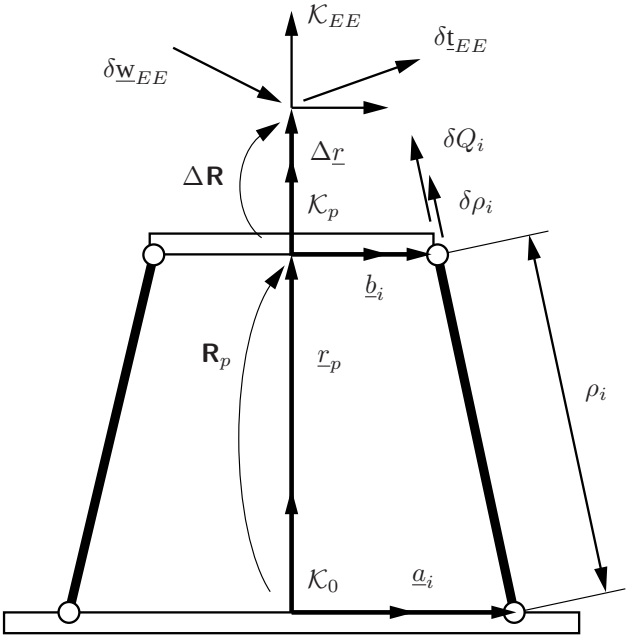

Figure 5.3: Kinetostatics of parallel platform

velocity $\boldsymbol{\omega}_P$ and linear velocity $\boldsymbol{v}_P$ at the origin of $\mathcal{K}_P$ are collected in the twist

$$\underline{\mathrm{t}}_P = [\boldsymbol{v}_P^{\mathrm{T}}, \boldsymbol{\omega}_P^{\mathrm{T}}]^{\mathrm{T}} \, . \tag{5.11}$$

Denoting again by $\delta \underline{\mathrm{t}}_P$ an infinitesimal change of pose, the relationship between small variations of leg lengths and small variations of pose is

$$\delta \underline{\mathrm{t}}_P = \mathbf{J}_P \, \delta \underline{\rho} \, , \tag{5.12}$$

where $\mathbf{J}_P$ is the Jacobian of the corresponding velocity mapping.

The operation point of the platform, called the end-effector frame $\mathcal{K}_{EE}$, is assumed to be offset with respect to the platform reference frame by an offset vector $\Delta \boldsymbol{r}$ and a relative rotation matrix $\Delta \mathbf{R}$ as depicted in Figure 5.3. Twists with respect to the platform frame are transformed to twists with respect to the end-effector frame by

$$\underline{\mathrm{t}}_{EE} = {}^{EE}\mathrm{X}_P \, \underline{\mathrm{t}}_P \, , \tag{5.13}$$

where ${}^{EE}\mathrm{X}_P$ is the spatial transformation matrix

$${}^{EE}\mathrm{X}_P = \begin{bmatrix} \Delta \mathbf{R}^{\mathrm{T}} & 0 \\ -\widetilde{\Delta \boldsymbol{r}} \, \Delta \mathbf{R}^{\mathrm{T}} & \Delta \mathbf{R}^{\mathrm{T}} \end{bmatrix} . \tag{5.14}$$

The overall transformation from infinitesimal leg length variations to infinitesimal variations of the end-effector frame becomes

$$\delta \underline{\mathrm{t}}_{EE} = \mathbf{J}_{EE} \, \delta \underline{\rho} \; ; \text{ with } \; \mathbf{J}_{EE} = {}^{EE}\mathrm{X}_P \, \mathbf{J}_P \, . \tag{5.15}$$

Using the duality of force and velocity transmission, the force transmission for the parallel platform becomes

$$\underline{Q} = \mathbf{J}_{EE}^{\mathrm{T}} \, \underline{\mathrm{w}}_{EE} \, , \tag{5.16}$$

where $\underline{Q} = [Q_1, \ldots, Q_6]^{\mathrm{T}}$ are the pushing leg forces, and $\underline{\mathrm{w}}_{EE} = [\boldsymbol{F}_{EE}^{\mathrm{T}}, \boldsymbol{M}_{EE}^{\mathrm{T}}]^{\mathrm{T}}$ is the wrench applied at the end-effector of the parallel platform, consisting of the moment $\boldsymbol{M}_{EE}$ and the force $\boldsymbol{F}_{EE}$ being applied to the origin of $\mathcal{K}_{EE}$. With the preceding quantities, the stiffness of the platform at the end-effector frame becomes

$$\mathbf{K}_{EE} = \mathbf{J}_{EE}^{-\mathrm{T}} \, \mathbf{K}_\rho \, \mathbf{J}_{EE}^{-1} \, , \tag{5.17}$$

where $\mathbf{K}_\rho = \mathrm{diag}\{k_1, \ldots, k_6\}$ with k_i corresponding to the local stiffness of the individual legs. As $\mathbf{J}_{EE}$ depends on both the platform geometry and the location of the tool-center point, it is evident that the offset of the tool-center point has the same order of the influence on stiffness as the platform geometry.

5.2 Platform-control concept

The model-based force control of the single actuator (section 4.4) was embedded into the force control of the platform. This was performed by running each actuator with its individually identified model-based force control. The aim was to produce defined forces and torques at the end effector of the platform. For these force-control experiments, the motion platform was fixed rigidly to an external rack by using a shaft as junction element. Before the manipulator was fixated, each leg was contracted to the previously defined operation point of -20 mm.

In order to compute the actuator forces which result from a target wrench, a computer model of the platform is needed which contains the kinetostatic model (section 5.1) of the parallel manipulator. The kinetostatic model of the platform was implemented in the multibody C++ library MBILE [52]. According to the platform-control scheme shown in Figure 5.4, the target wrench $\underline{\mathrm{w}}_{EE}$, which shall be produced with the end effector, is processed with the platform model programmed in MBILE computing the corresponding inverse Jacobian. Hereby, using the kinetostatic transmission method the platform target wrench $\underline{\mathrm{w}}_{EE}$ is mapped to the six actuator forces Q_i ($i = 1, \ldots, 6$). Hereby, friction was neglected.

The transmission equation for the ideal manipulator is considered as

$$\underline{Q} = \mathbf{J}_{EE}^{T}\, \underline{\mathrm{w}}_{EE}\,. \tag{5.18}$$

The six target forces are transmitted to the dSPACE control-unit which computes the six model-based control loops yielding the voltage signals to the valves of the six platform actuators. The feedback is given by 18 sensors measuring the pressure, force and position of each actuator. The

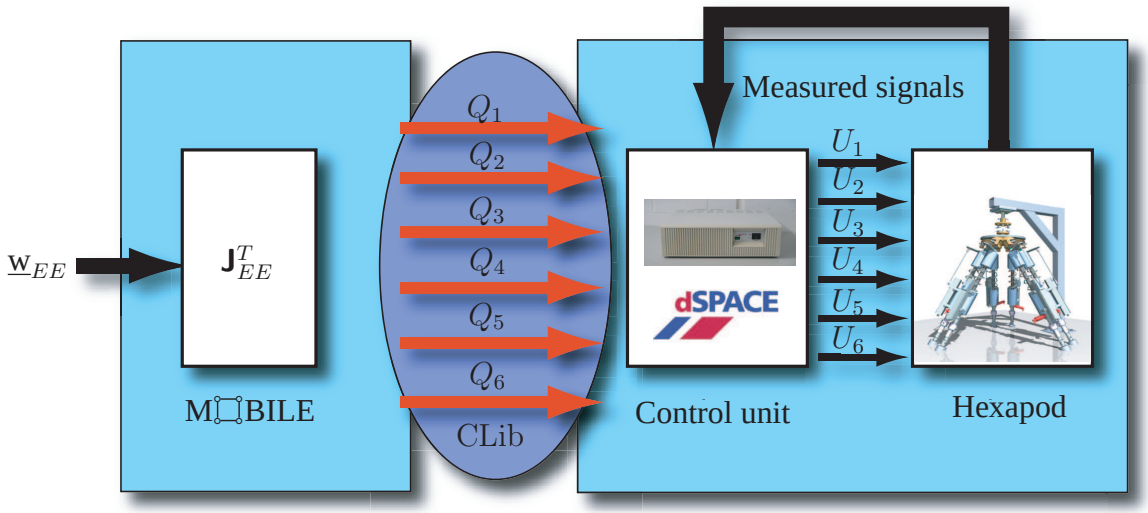

Figure 5.4: Platform control scheme

platform control was executed with a control rate of 10 ms and each actuator was processed with its own model-based force control containing the individually identified parameters.

In general, arbitrary wrench-time histories can be applied to the end effector within the limits given in Table 3.6. The platform control can also be run by applying directly six actuator target forces on the platform control without computing a target wrench before. The graphical user interface is shown in Figure 5.5.

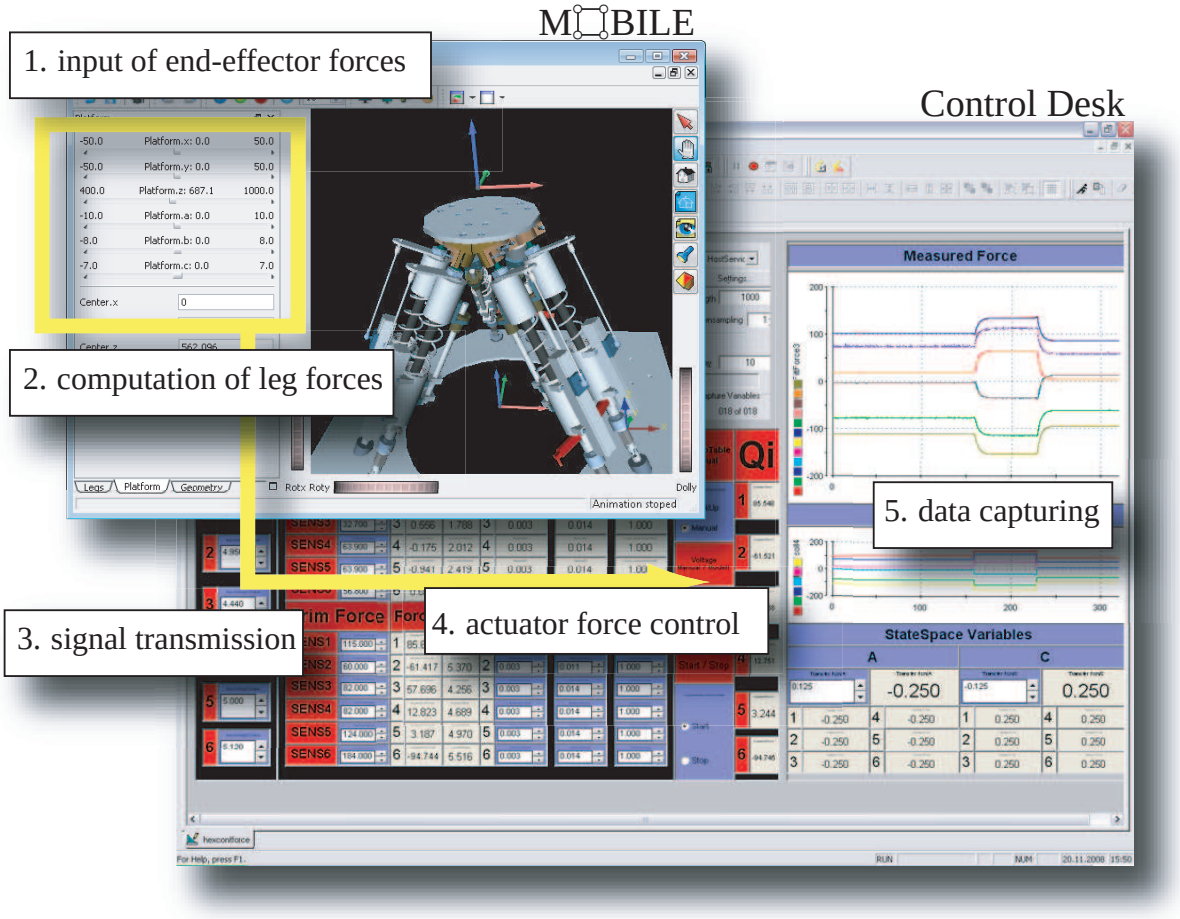

Figure 5.5: Graphical user interfaces for platform control

5.3 Experimental results of platform control

According to Table 3.6, the platform can lift approximately 100 kg. For the verification of the platform control, test runs have been applied producing either forces or moments with fixed end effector.

Each test run is divided into three steps, with (1) a pure x-load, then (2) the superposition of x- and y-load and finally (3) the interaction of loads in all three directions (x, y, z) with $F_x = F_y = F_z =$

-40 N (Figure 5.6). The target values were prescribed as PT_1 outputs of step functions in order to avoid the errors stemming from pressure rate jumps as described in section 5.3.

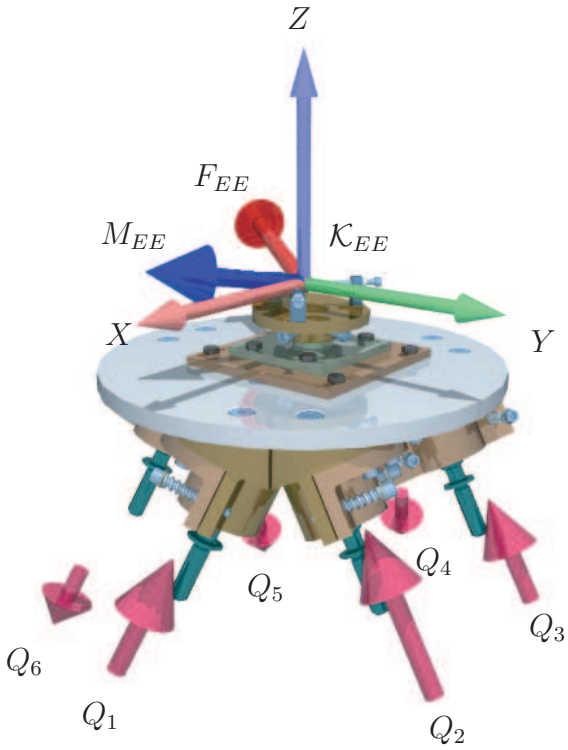

Figure 5.6: Forces at platform (Q_i: "+" for pushing; "-" for pulling)

Figure 5.7 shows the corresponding results. The selected time constant is $\Delta T = 2\mathrm{s}$. The measured values are given in solid lines; the target values are given in dashed lines. The response specifications as settling time t_s and overshoot M_p of the corresponding actuator force responses are given in reference to the ideal step functions.

The results in Figure 5.7 show a fair agreement of the target and measured values in the steady-state domain. However, at the beginning in the transient region of the force response, one can recognize larger errors. The maximum overshoot, here indicated at the force response Q_1 of actuator 1, is $Q_p = 4.4$ N and the time for reaching the steady-state domain is $t_s = 27$ s.

In the second test run, pure torques at the end effector (Figure 5.8) were applied in three steps similarly to the force test,with moment components $M_x = M_y = M_z = 2\,\mathrm{Nm}$. The time increment was chosen as $\Delta T = 2$ s.

Again, good agreement between the measured and the target values can be observed after the system has reached the stationary condition. But again at the beginning in the transient region the actuator forces are facing overshoots. The maximum overshoot here is $Q_p = 2.5$ N and the settling time is $t_s = 20$ s. In both above described test runs, the application of the time constant $\Delta T = 2$ s leads to overshoots in the transient domain but a good matching of the values in steady-state area.

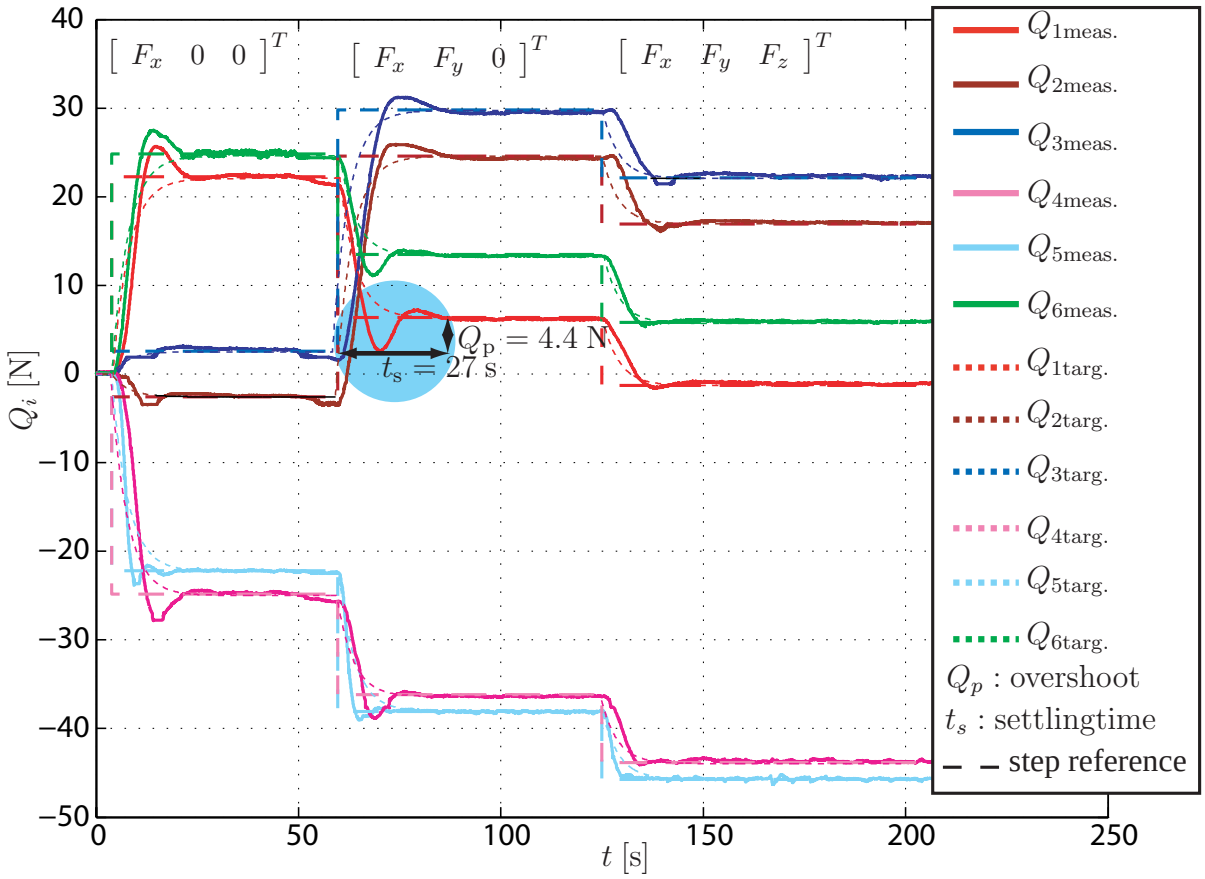

Figure 5.7: Resulting actuator forces Q_i for end-effector forces with $\Delta T = 2\ \mathrm{s}$

In order to evaluate the influence of the chosen virtual time constant ΔT on the platform control, further test runs were performed with varying ΔT. In Figure 5.9, the results for a decreased value of $\Delta T = 0.5\ \mathrm{s}$ are plotted. It becomes obvious that the decreased time increment raises the overshoots of all actuator-force responses. In order to compare with the described specifications of Figure 5.7, here also the overshoot and settling time of actuator 1 is indicated, which is $Q_p = 5.6\ \mathrm{N}$ and $t_s = 22\ \mathrm{s}$. This means that despite the larger overshoot the force response decays faster into the target value. It can be recognized that this behavior is followed by all six actuators.

Hence, decreasing ΔT can shorten the response time of the control, but also leads to higher overshoots. Especially, the fifth actuator is performing large overshoots up to $8\ \mathrm{N}$ and is facing instability in the steady-state region after the second step function was applied. Subsequently, another test run was executed with the same target values, this time using an increased time constant with $\Delta T = 6\ \mathrm{s}$ (Figure 5.10). Here, it becomes evident that each actuator is not pursuing any overshoot before yielding into the target values. In particular, actuator 6 is following the delayed reference signal fairly good in the first two sequences. However, the time to reach the target values of all actuators is relatively large, as indicated at the force response of actuator 1, where the corresponding settling time is $t_s = 30\ \mathrm{s}$, and thus, larger than the comparative values of the previous test runs. At all test runs, the gains of the PI controller in each of the six actuator-control loops were equal with $K_p = 0.004$ and $K_i = 0.03$. The characteristics of the actuator-force responses with respect

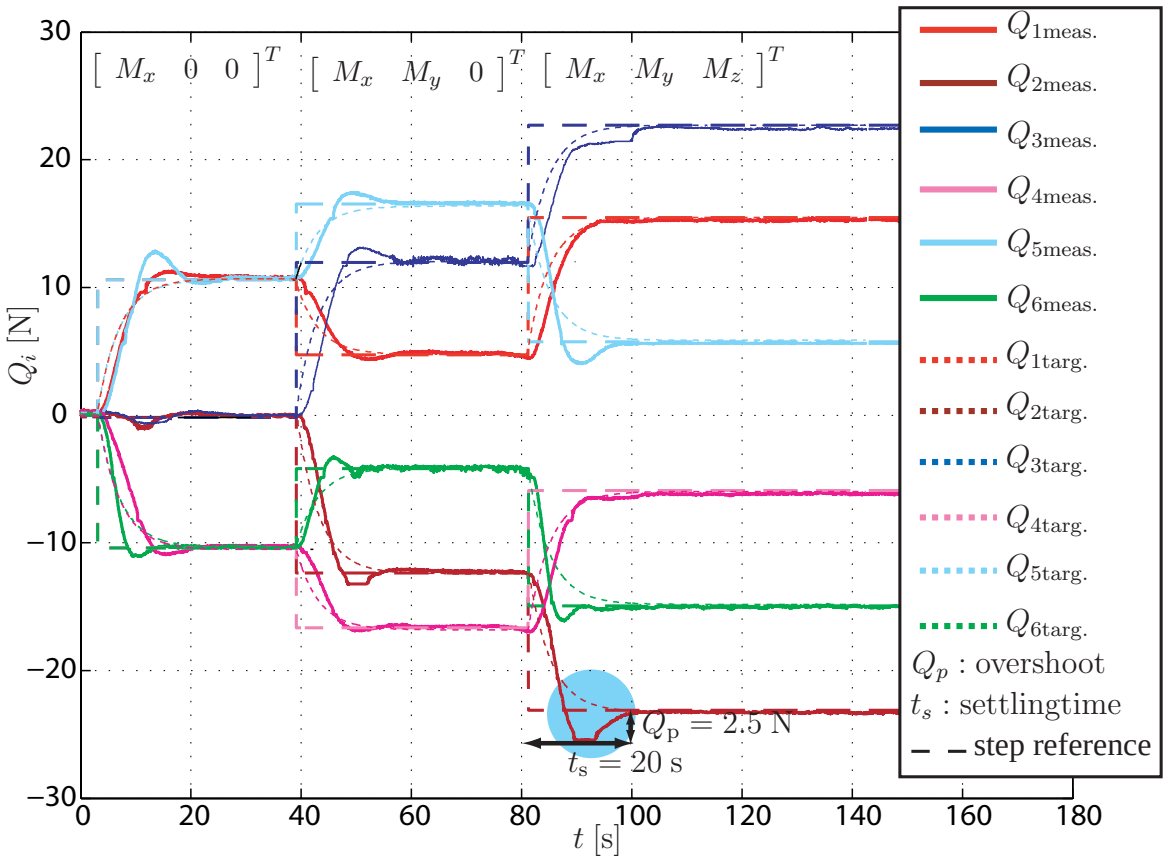

Figure 5.8: Resulting actuator forces Q_i for end-effector torques with $\Delta T = 2\,\text{s}$

	overshoot Q_p [N] (actuator 1)	settling time [s] (actuator 1)	maximal steady-state error [N]
$\Delta T = 0.5\,\text{s}$	5.6	22	0.69
$\Delta T = 2\,\text{s}$	4.4	27	0.77
$\Delta T = 6\,\text{s}$	0	30	0.49

Table 5.1: Specific properties of actuator-force responses

to the chosen ΔT are specified in table 5.1. In addition to the settling time and overshoot, also the maximal steady-state errors are indicated here.

It is obvious that the steady-state behavior is matched well with all three chosen virtual time increments ΔT, as the steady-state error is below 1 N. The best steady-state performance is achieved with $\Delta T = 6\,\text{s}$. This shows that the developed platform and the established control are well-suited for slowly varying force protocols. Moreover, as already mentioned above, one can see that the decrease of the time increment can improve the ability to respond fast to the target values ($t_s = 22\text{s}$ for $\Delta T = 6\,\text{s}$), but also raises the overshoots and the risk of entering an unstable condition. In contrast to it, a large ΔT can avoid fully the appearance of overshoots, but can increase the time for reaching the target value.

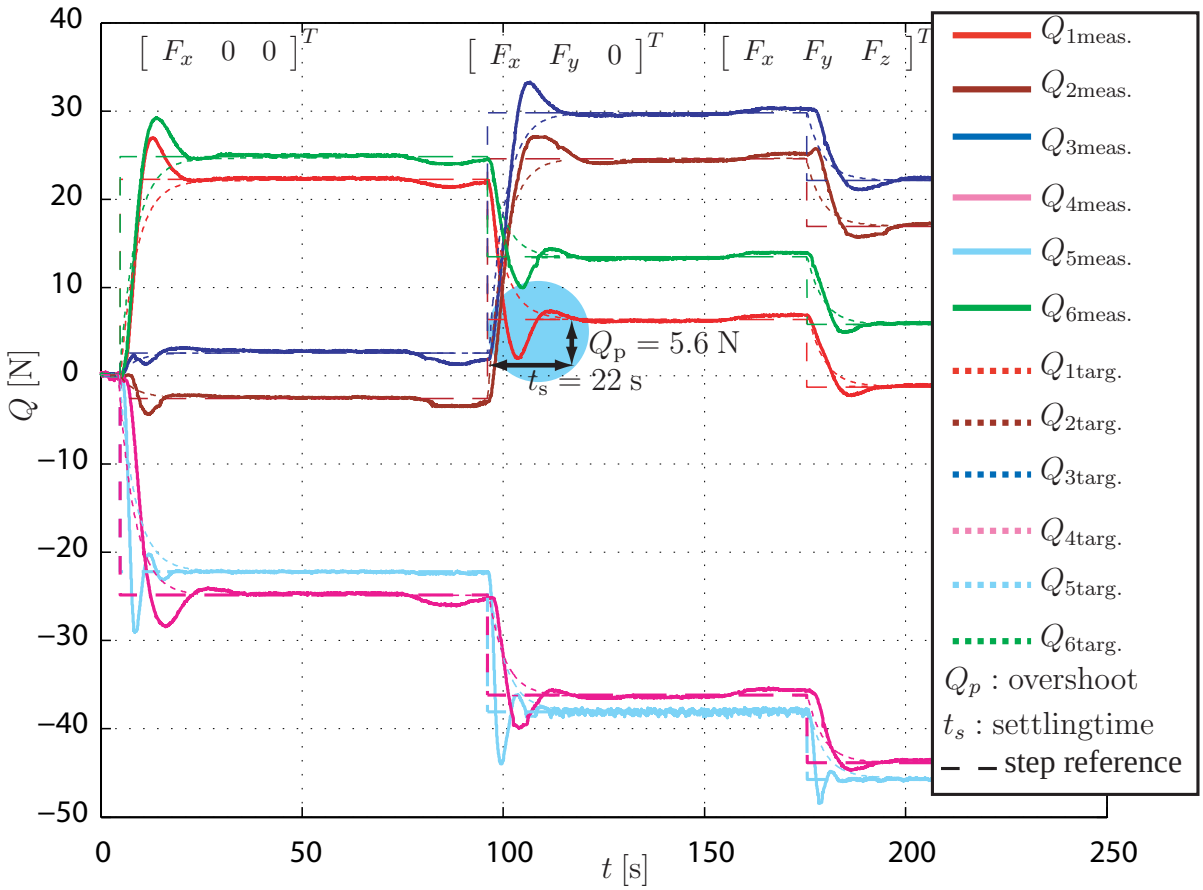

Figure 5.9: Resulting actuator forces Q_i for end-effector forces with $\Delta T = 0.5\ \mathrm{s}$

The steady-state performance of the developed control algorithm suffices to the requirements of a fine tuned force and torque control as far as slow variations are applied. However, the transient response-properties of the system require further improvement, as both, a good quasistatic and dynamic performance is advantageous for the exact reproduction of arbitrary force and torque functions.

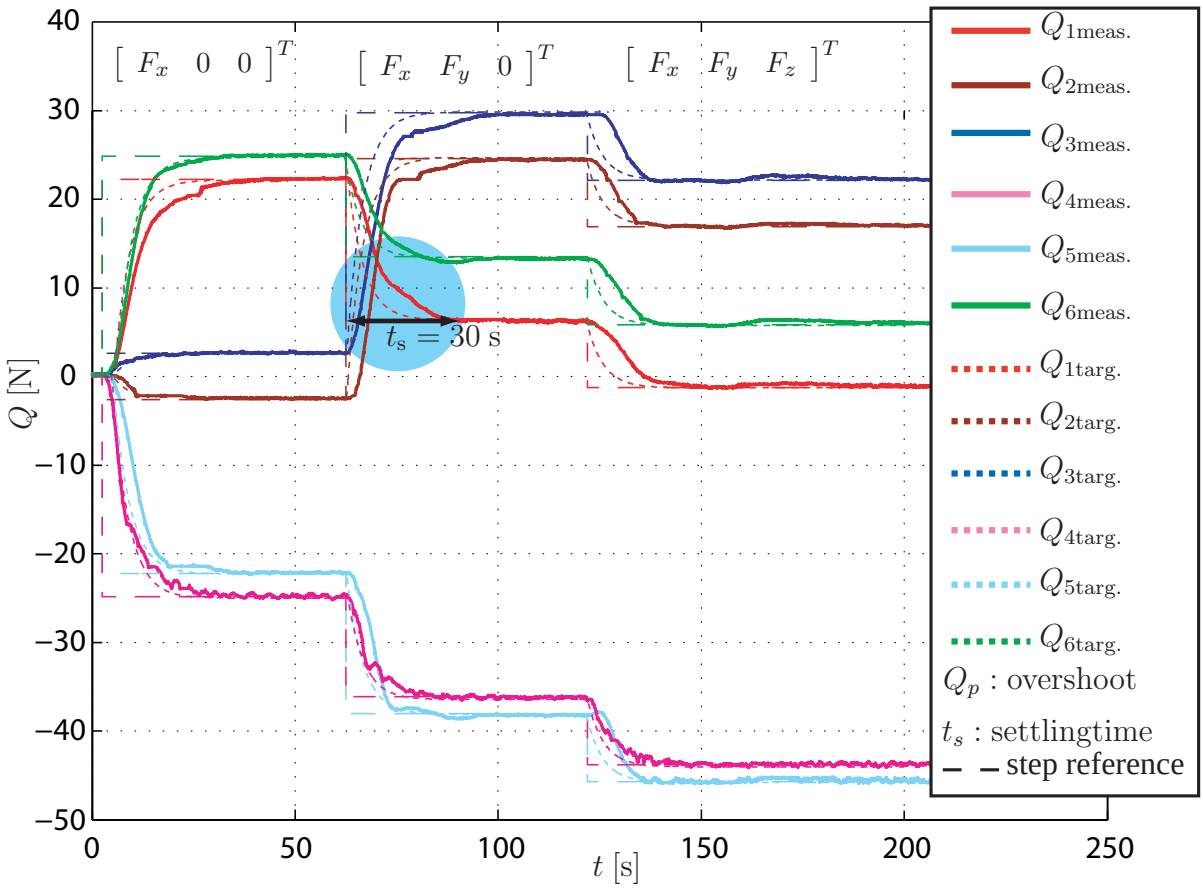

Figure 5.10: Resulting actuator forces Q_i for end-effector forces with $\Delta T = 6$ s

6 Conclusions and Outlook

In the present work, a force and torque controlled parallel robot driven by six actuator legs was developed and evaluated. The manipulator was designed for its future application as a physical simulator of cervical spine motion and was built as a Gough-Stewart type platform. Each actuator consists of a fluidic muscle which is combined with a prestressed coil spring in order to produce compressive as well as tensile forces. Through geometric limit analyses, it was verified that the workspace of the mobile platform fulfills the required motion and force range prescriptions for a cervical vertebrae pair. Hereby, the offset of the tool-center point to the mobile platform was chosen such that under the conditions of restricted actuator strokes the motion range requirements were fulfilled. Further, it was proven by interval analysis that the manipulator can produce the necessary intervertebral forces within the target workspace.

All six actuators were identified by analyzing their volume-stroke, force-stroke-pressure and gas dynamics relationships. The model-based force control of each actuator uses an exponential approximation of the transient pressure responses. Each actuator control loop contains the individually identified parameters of the corresponding fluidic muscle and valve. The six actuator control loops are embedded into the force and torque control of the parallel manipulator. The platform-control algorithm includes a kinetostatic platform model, which computes the corresponding required leg forces in order to achieve the target forces and torques at the end effector of the platform. For the verification of the single actuator control, test runs were carried out on a uniaxial test bed. It was shown that the presented actuator control can deal with target-force values which do not have rapid changes, as it was demonstrated with sinusoidal test signals featuring lower frequencies. Concerning the platform control, experiments with varying forces and torques against a rigid counterpart showed the useability of the concept.

The steady-state performance of the developed control algorithm sufficed to the requirements of a fine-tuned force and torque control as far as slow force variations were applied.

At this stage, the realized Hexaspine manipulator, the developed model-based actuator control and the implemented end-effector force and torque control have laid the foundation for further research in different aspects. The transient response-properties of the system still feature a larger difference between reference and measured values. Therefore, the system requires further improvement, as both, a good quasistatic and dynamic performance is advantageous for the exact reproduction of intervertebral force-displacement properties. Measurements have shown that the valve-muscle system features transients of second or third order (PT_2/ PT_3) at large step voltages when the valve

piston executes a large and abrupt opening or closing of the orifice. Therefore, a mathematical model of higher order describing more accurately the dynamic properties of the valve-muscle system could enhance the transient behavior of the controlled system.

Concerning the actuator itself, the behavior of pneumatic muscles may be time variant, as due to the dry friction of the rubber and the fibers heat is produced that influences the material characteristics after longer operation times. In literature it was observed that a cold muscle behaves different to a warm muscle leading to hysteresis in the force-stroke relationship. Another issue is that the fluidic muscles tend to change their voltage-pressure behaviors after longer time-periods (weeks, months) regardless of if the actuator was operated or not. That leads to difficulties when the model of each actuator system (valve and muscle) is calibrated in its voltage-pressure behavior. An adaptive control which calibrates the corresponding system parameters to the current conditions could lead to better transient responses. Moreover, in order to achieve stable control with soft environment, one could attempt to integrate the information about the current environment's compliance into the controller.

In closing, the present platform embodies a directly force-controlled manipulator for slow force protocols that in addition features the compliance when applied to a body. This is an advantage over position controlled platforms for which constraint forces can become very large. This is useful for simulating or measuring the force-displacement properties of a cervical pair but also for other physiological units, as the knee, hip and wrist joint.

Another field, for instance, can be the execution of specific loading-protocols on hip or knee prostheses, which is still widely done with position-controlled devices or test beds featuring only one degree of freedom. Finally, the parallel manipulator can be used also for producing force-protocols which are required for the examination of general mechanical components.

Bibliography

[1] **Ahn, K. and Nguyen, H.** (2007): Intelligent switching control of a pneumatic muscle robot arm using learning quantization neural network. *Science Direct, Mechatronics*, pages 255 – 262.

[2] **Ahn, K. and Thanh, T.** (2005): Intelligent phase plane switching control of pneumatic artifcial muscle manipulators with magneto-rheological brake. *Science Direct, Mechatronics*.

[3] **Ahn, K. and Thanh, T.** (2006): Nonlinear PID control to improve the control performance of 2 axes pneumatic artificial muscle manipulator using neural network. *Science Direct, Mechatronics*, page 577587.

[4] **Aracil, R.; Saltarén, R.; Sabater, J. and Reinoso, O.** (2006): Robots paralelos: máquinas con un pasado para una robótica del futuro. *Revista Iberoamericana de Automática e Informática Industrial*, 3:16–28.

[5] **Aschemann, H. and Hofer, E. P.** (2005): Flatness-based Trajectory Planning and Control for a Parallel Robot Actuated by Pneumatic Muscles. *ECCOMAS Thematic Conference Multibody Dynamics Advances in Computational Multibody Dynamics*.

[6] **Birglen, L.** (2003), Haptic Devices Based on Parallel Mechanisms. State of the Art.
URL `http://parallemic.org`

[7] **Bonev, I.** (2003), The True Origins of Parallel Robots.
URL `http://www.parallemic.org`

[8] **Bonev, I. and Ryu, J.** (2001): A geometrical method for computing the constant-orientation workspace of 6-PRRS parallel manipulators. *Mechanism and Machine Theory*, 36:1–13.

[9] **Bruyninckx, H.** (2005), Parallel robots, The Robotics WEBook.
URL `http://www.roble.info/robotics/parallel`

[10] **Caldwell, D.-G.; Medrano-Cerda, G. A. and Goodwin, M. J.** (1993): Measurement and modeling of McKibben pneumatic artificial muscles. *Proc. of the IEEE International Conference on Sys- tems, Man and Cybernetics*, page 423428.

[11] **Caldwell, D. G.; Medrano-Cerda, G. A. and Goodwin, M. J.** (1995): Control of Pneumatic Muscle Actuators. *IEEE Control Systems Magazine*, page 4048.

[12] **Chan, S. and Lilly, J.** (2003): Fuzzy PD+I learning control for a pneumatic muscle. *IEEE, International Conference on Fuzzy Systems*.

[13] **Chazal, J.; Tanguy, A.; Bourges, G.; Gaurel, G.; Escande, G.; Guillot, M. and Vanneuville, G.** (1985): Biomechanical properties of the spinal ligaments and a histological study of the supraspinal ligament in traction. *Journal of Biomechanics*, pages 167–176.

[14] **Chou, C.-P. and Hannaford, B.** (1996): Measurement and modeling of McKibben pneumatic artificial muscles. *Robotics and Automation, IEEE*, pages 12:90–102.

[15] **Clavel, R.** (1988): DELTA, a fast robot with parallel geometry. *18th Int. Symposium on Industrial Robot*, pages 91–100.

[16] **Culver, C. C.; Neathery, R. F. and Mertz, H.** (1972): Mechanical necks with human-like responses. *Society of Automotive Engineers SAE, Proc. of the 16th Stapp Car Crash Conference*, pages 61–75.

[17] **Daerden, F.** (1993): *Conception and realization of Pleated Pneumatic Artificial Muscles and their use as compliant actua- tion elements*. PhD Thesis, Vrije Universiteit Brussel.

[18] **Daerden, F. and Lefeber, D.** (2001): The concept and design of pleated pneumatic artificial muscles. *International Journal of Fluid Power*, 2(3):4150.

[19] **Daerden, F. and Lefeber, D.** (2002): Pneumatic artificial muscles: Actuators for robotics and automation. *European journal of mechanical and environmental engineering*.

[20] **Dasgupta, B. and Mruthyunjaya, T.** (1998): Singularity-free path planning for the stewart platform manipulator. *Mechanism Machine Theory*, 33:711–725.

[21] **Dasguptaa, B. and Mruthyunjaya, T.** (2000): The Stewart platform manipulator: a review. *Mechanism Machine Theory*, 35:15–40.

[22] **de Jager, M.** (1996): *Mathematical head-neck models for acceleration impacts*. Ph.D. thesis, Technische Universiteit Eindhoven, Eindhoven.

[23] **Dhanu Singh, M.; Liem, K.; Neumann, R. and Kecskeméthy, A.** (2007): Force Control of a Fluidic-Muscle Driven Parallel Platform. *Sixth International Congress on Industrial Applied Mathematics (ICIAM) and GAMM Annual Meeting*, Zurich.

[24] **Dong, J.; Yao, Q. and Ferreira, P.** (2008): A novel parallel-kinematics mechanism for integrated, multi-axis nanopositioning. *Precision Engineering*, 32:20–33.

[25] **Dvorak, J.; Panjabi, M.; Novotny, J. and Antinnes, J.** (1991): In vivo flexion/extension of normal cervical vertebrae. *Journal of Orthopaedic Research*, 9:828–834.

[26] **Faugere, J. and Lazard, D.** (1995): Combinatorial classes of parallel manipulators. *Mechanism and Machine Theory*, pages 765–776.

[27] **Festo & Co. KG** (2007), Fluidic Muscle MAS, Powerful, dynamic, stick-slip-free. Information material.
URL `http://festo.com`

[28] **Frindt, M.** (2001): *Modulbasierte Synthese von Parallelstrukturen für Maschinen in der Produktionstechnik*. Ph.D. thesis, Technische Universität Braunschweig, Braunschweig.

[29] **General Website** (2009), Drives & controls: The tripods are coming.
URL `http://www.drives.co.uk/features.asp?id=6`

[30] **General Website** (2009), Synovial Joints - Plane Joints.
URL `http://anatomy.med.umich.edu/modules/`

[31] **Goldsmith, W. and Deng, Y. C.** (1984): Numerical evaluation of a human head-neck model to dynamic loading. *Society of Automobile Engineers SAE, Special Publications*, pages 79–95.

[32] **Goldsmith, W. and Deng, Y. C.** (1987): A response of a human head/neck/upper-torso replica to dynamic loading-I. Physical model. *Journal of Biomechanics*, 20:471–486(5).

[33] **Goldsmith, W. and Deng, Y. C.** (1987): A response of a human head/neck/upper-torso replica to dynamic loading-II. Analytical/numerical model. *Journal of Biomechanics*, 20:487–497(5).

[34] **Gosselin, C. and Angeles, J.** (1990): Singularity analysis of closed-loop kinematic chains. *IEEE Transactions on Robotics and Automation*, 6(3):281290.

[35] **Gough, V.** (1956-1957): Contribution to discussion of papers on research in automobile stability, control and tyre performance. *Proc. Auto Div. Inst. Mech. Eng.*

[36] **Gough, V. and Whitehall, S.** (1962): Universal tyre test machine. *Proceedings 9th International Tech. Congress F.I.S.I.T.A*, pages 117:117–135.

[37] **Hebsacker, M.; Treib, T.; Zirn, O. and Honegger, M.** (1999): *Hexaglide 6 DOF and Triaglide 3 DOF Parallel Manipulators*. Parallel Kinematic Machines - Advanced Manufacturing Series - Springer Verlag.

[38] **Hesse, S.** (2003): *The Fluidic Muscle in Application*. Handling, Pneumatics (Blue Digest on Automation), Festo Didactics.

[39] **Hesselroth, T.; Sarkar, K.; van der Smaght, P. P. and Schulten, K.** (1994): Neural network control of a pneumatic robot arm. *IEEE Transactions on Systems, Man and Cybernetics*, page 2838.

[40] **Hildebrandt, A.; Sawodny, O.; Neumann, R. and Hartmann, A.**: A Flatness Based Design for Tracking Control of Pneumatic Muscle Actuators.

[41] **Hill, A.** (1938): The heat of shortening and the constants of muscle. *Proceedings of the Royal Society*, pages 136–195.

[42] **Honegger, M.; Codorey, A. and Burdet, E.** (1997): Adaptive control of the Hexaglide, a 6 dof parallel manipulator. *IEEE International Conference on Robotics and Automation*, pages 543–548.

[43] **Hunt, K.** (1983): Structural kinematics of in parallel-actuated robot arms. *ASME Journal of Mechanisms, Transmissions, and Automation in Design*, 105:705–712.

[44] **Huston, J. C. and Advani, S. H.** (1976): Three-dimensional model of the human head and neck for automobile crashes. *Mathematical Modeling of Biodynamic Response to Impact, Society of Automotive Engineers SAE, Special Publications*, pages 9–20.

[45] **Innocenti, C. and Parenti Castelli, V.** (1994): Exhaustive enumeration of fully-Parallel kinematic chains. *ASME International Winter Annual Meeting, Chicago*, pages DSC–Vol.55–2:1135–1141.

[46] **Inoue, K.** (1987): Rubbertuators and applications for robotics. *4th International Symposium on Robotics Research*, page 5763.

[47] **Jansen, T. H. and DiAngelo, D. J.** (1997): Influences of the location of vertebral 'IAR' on the cervical spine kinematics. Technical report, School of Biomedical Engineering, University of Tennessee.

[48] **Jiping, H.; Koeneman, E.; Schultz, R.; Huang, H.; Wanberg, J.; Herring, D.; Sugar, T.; Herman, R. and Koeneman, J.** (2004): Spring over muscle (SOM) actuator for rehabilitation devices. *Engineering in Medicine and Biology Society*, pages 2726–2729.

[49] **Jiping, H.; Koeneman, E.; Schultz, R.; Huang, H.; Wanberg, J.; Herring, D.; Sugar, T.; Herman, R. and Koeneman, J.** (2005): Design of a robotic upper extremity repetitive therapy device. *International Conference on Rehabilitation Robotics*, pages 95 – 98.

[50] **Kapandji, I.** (1992): *Funktionelle Anatomie der Gelenke*, volume Bd.3. Ferdinand Enke Verlag.

[51] **Kecskeméthy, A.** (1993): *Objektorientierte Modellierung der Dynamik von Mehrkrpersystemen mit Hilfe von Übertragungselementen*. Ph.D. thesis, University of Duisburg, Nr. 88 in Fortschrittsberichte VDI Verlag GmbH, Duisburg.

[52] **Kecskeméthy, A.** (2003): *MOBILE 1.3 User's guide and reference manual*. University of Duisburg-Essen.

[53] **Kecskeméthy, A. and Hiller, M.** (1994): An object-oriented approach for an effective formulation of multibody dynamics. *Computer Methods in Applied Mechanics and Engineering*, pages 115:287–314.

[54] **Kecskeméthy, A.; Lange, C. and Grabner, G.** (2000): Simulating Cervical Vertebrae Motion Using Elementary Contact Pairs. *26th Biennial Mechanisms and Robotics Conference, ASME*, 7:953–961.

[55] **Klute, G.; Czerniecki, J. and Hannaford, B.** (2002): Artificial muscles: actuators for biorobotic systems. *Int J Robotics*, page (4):295309.

[56] **Kumar, S.; Narayan, Y.; Amell, T. and Ferrari, R.** (2002): Electromyography of superficial cervical muscles with exertion in the sagittal, coronal and oblique planes. *European Spine Journal*, 11:27–37.

[57] **Lange, C.** (2001): *RoboSpine – Ein virtueller Halswirbelmechanismus für die anthropomorphe Reproduktion der Zwischenwirbelbewegung*. Ph.D. thesis, Technische Universität Graz, Graz.

[58] **Latham, F.** (1957): A study of body ballistics: Seat ejections. *Proceedings of the Royal Society*, pages B147:121–139.

[59] **Liem, K.; Dhanu Singh, M. and Kecskeméthy, A.** (77th Annual Scientific Conference of GAMM): Analysis of Vertebrae Motion with Computer Simulation using Elementary Contact Pairs. *GAMM*, Luxembourg.

[60] **Liem, K.; Kecskeméthy, A. and Merlet, J.-P.** (2007): HexaSpine: A Parallel Platform for Physical Cervical Spine Simulation - Design and Interval-Based Verification. *12th IFToMM World Congress in Mechanism and Machine Science*, Besançon, France.

[61] **Lorenz, B. and Pohl, M.**: Mechatronischer Entwurf eines Bewegungssimulators mit pneumatischen Zugaktoren in Hexapod-Struktur. Technical report, Festo AG & Co. KG and Fachhochschule Bochum.

[62] **Ma, O. and Angeles, J.** (1991): Optimum architecture design of platform manipulators. *ICAR, Fifth International Conference on Advanced Robotics. Robots in Unstructured Environments*, Vol.2:p. 1130–5.

[63] **Melvin, J. W.; McElhaney, J. H. and Roberts, V. L.** (1972): Improved Neck Simulation for Anthropometric Dummies. *Society of Automobile Engineers SAE, Proc. of the 16th Stapp Car Crash Conference, Nr. 720958*, pages 45–60.

[64] **Merlet, J.-P.** (1999): *The importance of optimal design for parallel structures*. Parallel Kinematic Machines - Advanced Manufacturing Series - Springer Verlag.

[65] **Merlet, J.-P.** (2006): *Parallel Robots*. Springer.

[66] **Merlet, J.-P.** (September 2004): *A C++ algorithms library of interval analysis for equation systems*, volume version 2.3. The COPRIN project.

[67] **Moriwaki, T.** (1999): *Survey of R&D Activities related to parallel mechanisms in Japan*. Parallel Kinematic Machines - Advanced Manufacturing Series - Springer Verlag.

[68] **Moroney, S.; Schultz, A.; Miller, J. and Andersson, G.** (1988): Load-displacement Properties of Lower Cervical Spine Motion Segments. *Journal of Biomechanics*, 21:769–779.

[69] **Myklebust, J.; Pintar, F.; Yoganandan, N.; Cusick, J.; Maiman, D.; Myers, T. and Sances, A.** (1988): Tensile strength of spinal ligaments. *Spine*, 13:526–531.

[70] **Nelson, T. S. and Cripton, P. A.** (2008): Biofidelic Surrogate Neck for Axial Impacts. Technical report, Departments of Mechanical Engineering and Orthopaedics, University of British Columbia.

[71] **Neugebauer, R.** (2006): *Parallelkinematische Maschinen*. Springer Verlag.

[72] **Panjabi, M.** (1973): Three-dimensional mathematical model of the human spine structure. *Journal of Biomechanics*, 6:671–680.

[73] **Panjabi, M.; Oxland, T.; Takata, K.; Goel, V.; Duranceau, J. and Krag, M.** (1988): Articular facets of the human spine: Quantitative three-dimensional anatomy. *Spine*, 13:526–531.

[74] **Panjabi, M. M. and Myers, B. S.** (1995): Cervical spine protection report prepared for NOCSAE. Technical report, Biomechanics Laboratory, Yale University and Department of Biomedical Engineering, Duke University.

[75] **Parenti Castelli, V.** (1999): *Classification and Kinematic Modelling Modelling of Fully-Parallel Manipulators-A Review*. Parallel Kinematic Machines - Advanced Manufacturing Series - Springer Verlag.

[76] **Parenti Castelli, V. and Innocenti, C.** (1990): Direct position analysis of the stewart platform mechanism. *Mechanism Machine Theory*, 25:611–621.

[77] **Penning, L.** (1989): *Funstional anatomy of joints and discs*. Number 33-56 in 2.Edition, J.B. Lippincott Company, Philadelphia.

[78] **Pierrot, F. and Uchiyama, M.** (1990): A New Design of a 6-DOF Parallel Robot. *Journal ref: Journal of Robotics and Mechatronics*.

[79] **Pohl, M.**: Mechatronischer Entwurf eines Bewegungssimulators mit pneumatischen Zugaktoren in Hexapod-Struktur. Technical report, Fachhochschule Bochum, Fachbereich: Mechatronik und Maschinenbau.

[80] **Pritschow, G.; Eppler, C. and Lehner, W.-D.** (2002): Highly dynamic drives for parallel kinematic machines with constant arm length. *1st Int. Colloquium, Collaborative Research Centre*, pages 199–211.

[81] **Roddeck, W.** (2003): *Einführung in die Mechatronik*. 2. Auflage, Teubner.

[82] **Ryu, J. and Cha, J.** (2003): Volumetric error analysis and architecture optimization for accuracy of HexaSlide type parallel manipulators. *Mechanisms and Machine Theory*, 38:227–240.

[83] **Schulte, H.** (1961): The characteristics of the McKibben artificial muscle. *The application of external power in prosthetics and orthotics, Publication 874 of the National Academy of SciencesNational Research Council, Lake Arrowhead.*, page pp. 94115.

[84] **Shea, M.; Edwards, W. T.; White, A. A. and Hayes, W. C.** (1991): Variations of stiffness and strength along the human cervical spine. *Journal of Biomechanics*, 24:95–107.

[85] **Smith; van Ness and Abbott** (1996): *Introduction to Chemical Engineering Thermodynamics*, volume 5th edition.

[86] **St-Onge, B. and Gosselin, C.** (2000): Singularity Analysis and Representation of the General Gough-Stewart Platform. *The Int. Journal of Robotics Research*, 19:271–288.

[87] **Stewart, D.** (1965): A platform with six degrees of freedom. *Proceedings of the Inst. of Mech. Eng.*, pages 180(1):371–386.

[88] **Stokes, I. A.; Gardner-Morse, M.; Churchill, D. and Laible, J. P.** (2002): Measurement of a spinal motion segment stiffness matrix. *Journal of Biomechanics*, 35:517–521.

[89] **Sugar, T.; Jiping, H.; Koeneman, E.; Koeneman, J.; Herman, R.; Huang, H.; Schultz, R.; Herring, D.; Wanberg, J.; Balasubramanian, S.; Swenson, P. and Ward, J.** (2007): Design and Control of RUPERT: A Device for Robotic Upper Extremity Repetitive Therapy. *IEEE Transactions on Neural Systems and Rehabilitation Engineering*, pages 336 – 346.

[90] **Sukovich, W.; Brink-Danan, S. and Hardenbrook, M.** (2006): Miniature robotic guidance for pedicle screw placement in posterior spinal fusion: early clinical experience with the SpineAssist. *The international journal of medical robotics and computert assisted surgery*, 2:114–122.

[91] **Thacker, B.; Nicolella, D. P.; Kumaresan, S.; Narayan, Y. and Pintar, F. A.** (2001): Probabilistic finite element analysis of the human lower cervical spine. *Journal of Mathematical Modeling and Scientific Computing*, pages 13(1–2): 12–21.

[92] **Uchiyama, M.** (1994): A 6 d.o.f. parallel robot HEXA. *Journal ref: Journal of Robotics and Mechatronics*, page 8(6):601.

[93] **Verrelst, B.; Daerden, F.; Lefeber, D.; Van Ham, R. and Fabri, T.**: Introducing Pleated Pneumatic Artificial Muscles for the Actuation of Legged Robots: a One-dimensional Set-up. Technical report, Vrije Universiteit Brussel, Dep. Of Mechanical Engineering.

[94] **Verrelst, B.; Vanderborght, B.; Vermeulen, J.; Van Ham, R.; Naudet, J. and Lefeber, D.** (2005): Control architecture for the pneumatically actuated dynamic walking biped Lucy. *Mechatronics*, pages 703–729.

[95] **Vorndran, S.** (2002): Low-Inertia Parallel-Kinematics Systems for Submicron Alignment and Handling.
URL `http://parallemic.org`

[96] **Walker, J.; Harris, E. H. and Pontius, U. R.** (1973): Mass, volume, center of mass, and mass moments of inertia of head and head and neck of human body. *Society of Automotive Engineers SAE, Proc. of the 17th Stapp Car Crash Conference*, pages 522–537.

[97] **Wang, J. and Masory, O.** (1993): On the accuracy of a Stewart platform. I. The effect ofmanufacturing tolerances. *Proc. of IEEE Conference on Robotics and Automation*, pages (1)114–120.

[98] **Wedler, A.; Friederichs, J.; Hackelöer, F. and Denkena, B.** (2008): New Compliant Mc-Kibben Actuator Driven by Pneumatic Actuators as a Hexapod Platform in Robotic Applications. Technical report, Institute of Production Engineering and Machine Tools, Leibniz University Hannover.

[99] **White, A. and Panjabi, M.** (1990): *Clinical Biomechanics of the Spine*. J.B. Lippincott.

[100] **Wurst, K.** (1999): *LINAPOD machine tools as Parallel Link Systems Based on a Modular Design*. Parallel Kinematic Machines - Advanced Manufacturing Series - Springer Verlag.

[101] **Yang, L. and Lilly, J.** (2003): Sliding mode tracking for pneumatic muscle actuators in bicep/tricep pair configuration. *American Control Conference*, pages 4669 – 4674.

[102] **Yoshikawa, T.** (1982): Manipulability of robotic mechanisms. *The Int. J. of Robotics Research*, 1(1).

[103] **Zhu, X.; Tao, G.; Yao, B. and Cao, J.** (2008): Adaptive robust posture control of a parallel manipulator driven by pneumatic muscles. *Science Direct, Automatica*, pages 2248–2257.